FORSCHUNGSZENTRUM JÜLICH GmbH KFA

Institut für Festkörperforschung

Interlayer Magnetic Coupling in Iron Layered Structures

Qunwen Leng

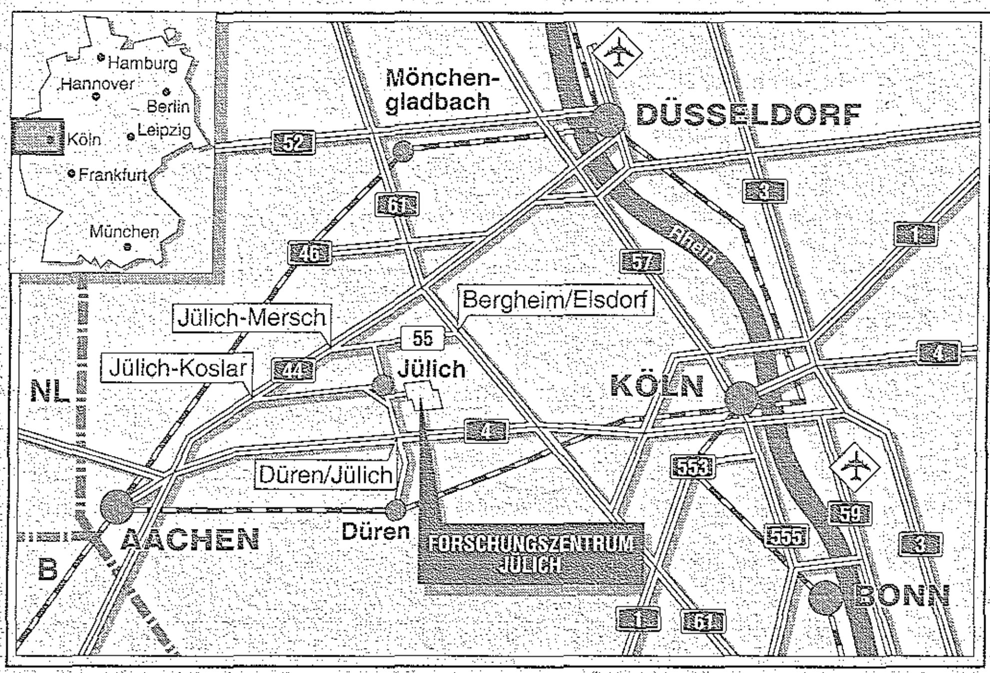

Berichte des Forschungszentrums Jülich ; 2934
ISSN 0944-2952
Institut für Festkörperforschung Jül-2934
D 38 (Diss. Universität Köln)

Zu beziehen durch: Forschungszentrum Jülich GmbH · Zentralbibliothek
D-52425 Jülich · Bundesrepublik Deutschland
Telefon: 02461/61-6102 · Telefax: 02461/61-6103 · Telex: 833556-70 kfa d

Interlayer Magnetic Coupling in Iron Layered Structures

Qunwen Leng

Abstract

In this thesis the magnetic coupling between iron layers across nonmagnetic metal interlayers has been investigated by means of magneto-optic methods. The epitaxial growth and crystalline quality of the layered structures were controlled by RHEED, SPA-LEED and AES techniques. Magnetic properties of ultrathin Fe films from 1.5 to 16 atomic layers have been studied by Brillouin light scattering (BLS) and magneto-optic Kerr effect (MOKE). Interlayer coupling in Cr spacer systems has been investigated systematically. On large GaAs substrates two period oscillations in the coupling as a function of the interlayer thickness have been observed, the thermal stability and temperature dependence of the coupling have been investigated up to 700K. The oscillation periods and the attenuation of the oscillation amplitudes can be understood with the help of the nesting effect in the Fermi-surface of Cr, on the basis of RKKY type interaction. The origin of biquadratic coupling and absence of phase-slips in the fine oscillations have been interpreted as due to reduced quality of the crystalline structure of the Cr interlayer and the Fe/Cr interfaces. The influence of interface roughness on oscillatory coupling has been studied by adding an Ag layer between the Cr interlayer. The additional Ag layer results in weaker bilinear coupling, but stronger biquadratic exchange due to introducing interface roughness. The two period oscillations of the magnetic coupling across noble metal spacers can be reproduced on the basis of the RKKY type interaction theory. It has been confirmed in the case of the noble metals that the oscillatory periods depend on the extremal distances in the Fermi-surfaces of the interlayer elements. Annealing investigations on the coupling have been performed in the layered structures with different interlayers. Both the structure effect of the interlayer and the interface effect have been observed in Cu-Au alloy systems. Antiferromagnetic coupling in these systems can be largely enhanced after annealing at an appropriate temperature due to improvement of the interlayer crystallinity. In addition, in an Au/Cu superlattice spacer structure an antiferromagnetic coupling has been observed after annealing, which coupled ferromagnetically before the annealing.

Contents

With 76 Figures and 9 Tables

1 Introduction

In the last decade the study of magnetic properties in ultrathin metallic layered systems has been very active. The development of UHV (ultra-high-vacuum) technology, MBE (molecular beam epitaxy) techniques and especially the ultilization of various in situ analysis made possible the preparation or/and reproduction of single layer and multilayer structures with sharp interfaces on an atomic scale. This progress brought good prospects of investigating basic problems and magnetism in thin- and ultra-thin films, and constructing new magnetic materials.

The studies presented in this dissertation were focused on the interlayer magnetic coupling. The approach of coupling between magnetic layers interspaced by a nonmagnetic layer has attracted wide interest, since the discovery of the antiferromagnetic coupling in the Fe/Cr layered system in 1986[1.1]. The interest in this phenomenon is not only one of fundamental physics, but also motivated by a search for new magnetic materials with novel properties. Because these systems developed also an unique GMR (giant magnetoresistance) effect[1.2,1.3] which shows a marked increase of the electrical resistivity due to the antiparallel alignment of the magnetizations in adjacent magnetic layers, this effect has potential applications[1.4] in field sensors for data memories. The investigation of magnetic interlayer coupling can be traced back to the 1960s[1.5]. Ferro- and antiferromagnetic coupling were discussed at that time, but only the ferromagnetic coupling was obtained. The quality of the ultrathin layered structures might play a very important role in the coupling, because direct coupling of magnetizations through the so-called pinholes in the interlayer could be reponsible for the ferromagnetic coupling. In 1986 for the first time Grünberg, et al[1.1] showed the antiferromagnetic coupling in a sandwich of Fe/Cr/Fe. The coupling was determined by BLS (Brillouin light scattering) techniques. Subsequently, Parkin, et al[1.6] discovered that the coupling could oscillate as a function of the interlayer thickness in polycrystalline magnetic multilayers prepared by the sputtering technique. In 1991 another coupling type, so-called 90°-type coupling, was discovered between the ferro- and antiferromagnetic coupling range in a wedge-shaped interlayer system of Fe/Cr/Fe sandwich by a Kerr domain observation[1.7]. In this type coupling the two magnetizations of the Fe layers prefer perpendicular alignment without applied magnetic field. The magnetic exchange interface energy density, E_i, between two ferromagnetic layers (1 and 2) can be described by[1.7,1.8]

$$E_i = -J_1 \bullet \frac{\bar{M}_1 \bullet \bar{M}_2}{|\bar{M}_1| \bullet |\bar{M}_2|} - J_2 \bullet \frac{(\bar{M}_1 \bullet \bar{M}_2)^2}{|\bar{M}_1|^2 \bullet |\bar{M}_2|^2} \qquad (1.1)$$

where J_1 and J_2 are the exchange coupling coefficients for, respectively, bilinear- and biquadratic coupling between the magnetization $\bar{M}_1$ and $\bar{M}_2$. The relations between the coupling types and the exchange coefficients will be described in detail in chapter 3. The coupling parameters, J_1 and J_2, can be obtained from different experiments, such as MOKE (magneto-optical Kerr effect)[1.9,1.10], BLS (Brillouin light scattering)[1.1,1.10] and FMR (ferromagnetic resonance)[1.11], etc. In addition, KM (Kerr microscopy) [1.7] and SEMPA (scanning electron microscopy with polarization analysis)[1.12] can be used to qualitatively investigate the coupling phenomenon.

Although magnetic couplings which show oscillations have been found with many elements as interlayers [1.1,1.6-1.13] and approached in intense theoretical work[1.13-1.26], the understanding of the coupling phenomenon is still unsatisfactory. More detailed experiments and comparison with existing theoretical work are necessary. This work intends to make a contribution to a better understanding of the microscopic origin of the coupling phenomena.

This dissertation consists of eight chapters. Chapter 2 describes the experimental methods and a brief outline of their principles. This includes the MBE system for the preparation and the MOKE-, BLS-, Kerr microscopy and GMR- techniques for the investigation of the layered structures. Chapter 3 introduces the theoretical background and characterization of exchange coupling between two ferromagnetic layers interspaced by a nonmagnetic metallic interlayer . In the fourth chapter the investigation of the magnetic properties of ultrathin iron films with thicknesses between 1.5 and 16 atomic layers is presented. Chapter 5 presents systematical studies of magnetic interlayer coupling between Fe layers separated by Cr interlayers. In this chapter the epitaxial growth of the studied sandwich structures, the thermal stability of the coupling, temperature dependence of bilinear and biquadratic coupling, coupling with modified interlayers, ferromagnetic layer thickness dependent coupling and nesting effect in Fe/Cr/Fe systems are discussed. Emphasis is put on the origin of the biquadratic coupling and the influence of interface quality on the coupling, and comparison with the current theoretical understanding. The nobel metal spacer systems are investigated in the frame of the RKKY like interaction theory in chapter 6. Chapter 7 contains the description of the annealing effects on the exchange coupling in Fe/X/Fe systems, where X denotes Cr, Cr/Ag/Cr, AuCu, Ag, Cu and Al etc . This part concentrates on the annealing effect of the coupling in the layered structures with AuCu superlattices and their alloys. The structure of the interlayer and the interface are discussed in the text. The last chapter summarizes the results presented in this dissertation.

References

[1.1] P.Grünberg, R.Schreiber, Y.Pang, M.B.Brodsky, H.Sowers, Phys. Rev. Lett. 57 (1986) 2442.

[1.2] G.Binasch, P.Grünberg, F.Saurenberg, W.Zinn, Phys. Rev. B 39 (1989) 4828.

[1.3] M.N.Baibich, J.M.Broto, A.Fert, F.Nguyen van Dau, F.Petroff, P.Etienne, G.Creuzet, A.Friederich, J.Chazelas, Phys. Rev. Lett. 61 (1988) 2472.

[1.4] P. Grünberg, Germany Patent D.P.D.E.-PS 3820 475.

[1.5] J.C.Bruyere, O.Massenet, R.Montmony and L.Neel, C.R.Acad.Sci. Paris 258 (1964) 1423.

[1.6] S.P.Parkin, N.More, K.P.Roche, Phys. Rev. Lett. 64 (1990) 2304.

[1.7] M.Ruehrig, R.Scgaefer, A.Hubert, R.Mosler, J.A.Wolf, S.Demokritov, P.Grünberg, Phys. Stat. Sol. (a) 125 (1991) 635.
[1.8] Q.Leng, J.A.Wolf, P.Grünberg, W.Zinn, Proc. of Int. Conf. on the Phys. of Trans. Met. Darmstardt, Germany 1992, 434.
[1.9] A.Fuss, Dissertation, University of Cologne (1993).
[1.10] S.W.Demokritov, J.A.Wolf, P.Grünberg, Europhys. Lett. 15 (1991) 881.
[1.11] B.Heinrich, K.B.Urquhart, A.S.Arrott, J.F.Cochran, K.Myrtle, and S.T.Purcell, Phys. Rev. Lett. 59 (1987) 1756.
[1.12] J.Unguris, R.J.Celotta, D.T.Pierce, Phys. Rev. Lett. 67 (1991) 140.
[1.13] A.Fuss, S.Demokritov, P.Grünberg, and W.Zinn, J. Magn. Magn. Mater. 103 (1992) L221.
[1.14] Y.Wang, P.M.Levy and J.L.Fry, Phys. Rev. Lett. 65 (1990) 2732.
[1.15] P.Bruno and C.Chappert, Phys. Rev. Lett. 67 (1991) 1602 and 2592.
[1.16] P.Bruno and C.Chappert, Phys. Rev. B 46 (1992) 261.
[1.17] Y.Yafet, Phys. Rev. B 36 (1987) 3948.
[1.18] C.F.Majkrzak, J.W.Cable, J.kwo, M.Hong, D.B.McWhan, Y.Yafer, J.V.Waszczak and C.Vettier, Phys. Rev. Lett. 56 (1986) 2700.
[1.19] W.Baltensperger and J.S.Helman, Appl. Phys. Lett. 57 (1990) 2954.
[1.20] F.Herman, J.Sticht and M.Van Schilfgaarde, in Mat. Res. Soc. Symp. Proc. edited by S.S.P.Parkin, et al., 1992, vol. 231, p. 195.
[1.21] D.M.Edwards, J.Mathon, R.B.Muniz and M.S.Phan, Phys. Rev. Lett.67 (1991) 493; J.Phys.Condens.Mater. 3(1991) 4941.
[1.22] J.Mathon, J.Magn.MAgn.Mater. 100 (1991) 527.
[1.23] J.Barnas, J.Magn.Magn.Mater. 111 (1992) L215.
[1.24] J.C.Slonczewski, Phys. Rev. Lett. 67 (1991) 3172.
[1.25] Daniel Stoeffler and Francois Gautier, J. Magn.Magn.Mater. 121 (1993) 259.
[1.26] P.Lang, L.Nordstrom, R.Zeller and P.H.Dederichs, Phys. Rev. Lett. 71 (1993) 1927.

2 Experimental Methods

With 5 Figures

2.1 Introduction

The Layered Structures, which are studied in this work, were fabricated by means of Molecular Beam Epitaxy (MBE) and characterized with Reflection High Energy Electron Diffraction (RHEED), Spot Profile Analysis - Low Energy Electron Diffraction (SPA-LEED) and Auger Electron Spectroscopy (AES). Magnetic Interlayer Coupling (MIC) and other magnetic properties in these structures were investigated by magneto - optic techniques, such as Magneto - Optical Kerr Effect (MOKE), Brillouin Light Scattering (BLS) and Kerr Microscopy (KM), etc. Giant Magnetoresistance (GMR) in these structures was measured with a four-point method.

2.2 Molecular Beam Epitaxy Facilities

A sketch of the MBE system is shown in fig.2.1. It consists of three chambers which are separated through slide valves. There is an antechamber, main chamber and analysis chamber.

A motor-driven manipulator at the end of which a sample holder is located is transferable to reach each of the three chambers without breaking the vacuum. Using metal claws, sample substrates will be secured on the sample holder which can be cooled or heated at temperatures between 80 and 923K. Usual substrate formats are 6×16 mm² or 10×10 mm².

In the antechamber a pressure of 5×10^{-7} Pa will be reached using a turbomolecular pump. In this chamber a thermal evaporation source with an Al_2O_3 crucible and an electron gun evaporator are available. The thickness of the samples is measured with a quartz thickness monitor. Due to the relatively high pressure this chamber is used only to prepare protective films or other films for which a high vacuum condition is not necessary.

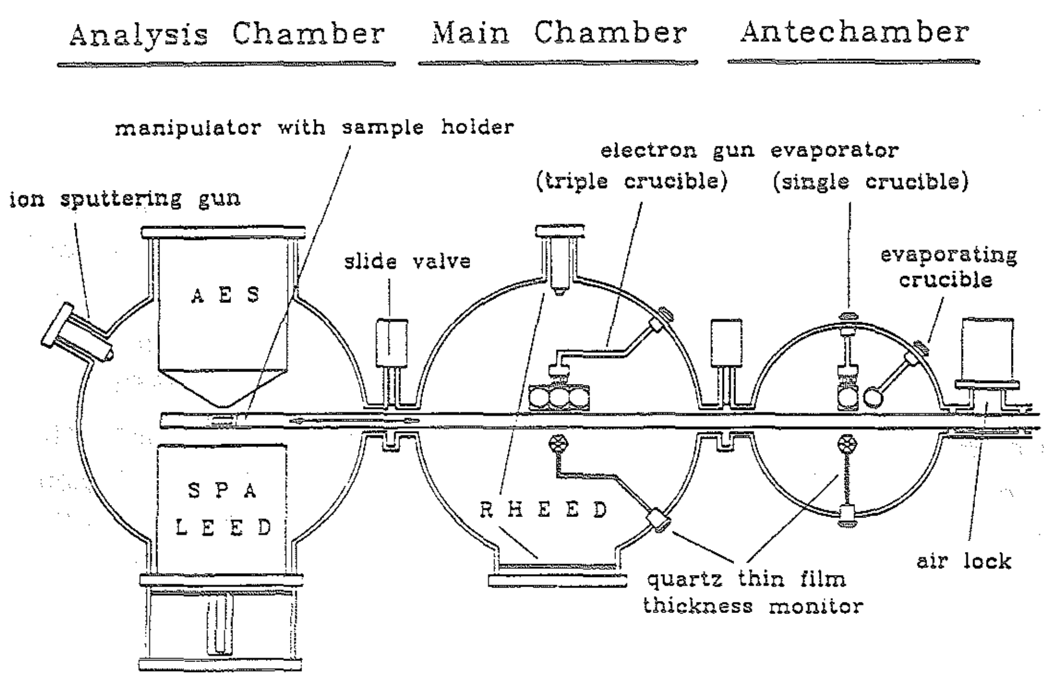

Fig.2.1 Schematic Diagram of the Cross Section of the Molecular Beam Epitaxy System (after Wolf [2.1])

Epitaxial growths of the studied ultrathin layered structures are carried out in the main chamber. A turbomolecular pump and an additional titanium sublimation pump with a cooling trap are used to maintain a ground pressure of approximately 2×10^{-9} Pa in this chamber. With the help of an electron gun a triple crucible allows one to deposit three different materials. A quartz oscillator is used to monitor the thin film thickness and to controll the vaporization rate. This chamber houses a RHEED system, used to monitor the epitaxial growth in situ. An unique sample of a wedge geometry can be achieved in this chamber by moving the transferable sample arm during the sample preparation [2.1, 2.2].

The analysis chamber keeps almost the same background pressure as the main chamber. An AES system for chemical analysis of surfaces and a SPA-LEED analytical system for structure investigations are situated in this chamber. It is also equipped with an ion sputtering gun for cleaning the substrate or sample surfaces.

2.3 Magneto-Optical Kerr Effect (MOKE)

To study the interlayer exchange coupling in the layered structures, MOKE is essential throughout the course of this dissertation. The MOKE is an effective tool for investigating the magnetization process in ultrathin magnetic film systems.

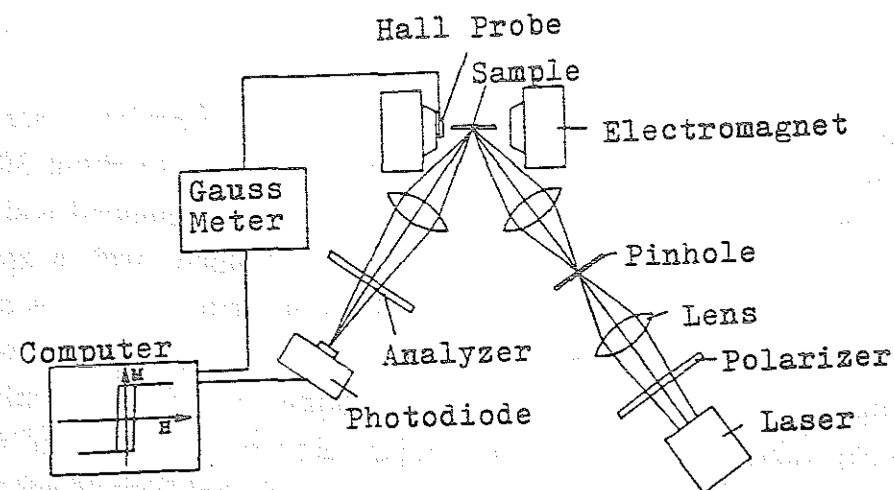

Fig.2.2 Experimental Set-up for Measuring the Longitudinal Magneto-optical Kerr Effect (after Fuss[2.3])

Fig.2.2 shows the experimental set-up for the MOKE measurement. During the experiment the measured sample is put between the magnetic poles of an electromagnet. A laser beam with a wavelength of 7500Å emitted from a semiconductor laser and polarized by means of a polarizer is focused onto the sample surface. The linearly polarized light is reflected from the magnetic sample, where its polarization plane will rotate by an angle which is proportional to the magnetization component lying in the sample plane in first approximation. Then the reflected beam passes an analyzer and is detected with a photodiode. Only the longitudinal MOKE is adopted in this work. In this case only the signal of the magnetization component parallel to the incident plane of the light beam will be measured. With the help of a Gauss menter and a Hall probe near the sample the applied magnetic field is measured at the same time. Therefore, a hysteresis loop of the magnetic sample can be obtained using a computer to collect the two signals.

The laser beam whose wavelength λ is about 7500Å penetrates only several hundred angstroms into a metal surface. For this reason the effect is also known as SMOKE (surface MOKE), which is effective to measure thin magnetic layers. The focused laser spot on the sample is within 0.3 mm. A screw micrometer connected with the sample holder can move the whole sample holder in small steps, for example 0.1 mm, so that it is possible to attain M(H) curves from different thickness of the studied thin film specimens in a wedge geometry.

Investigation of temperature dependence and heat treatment are the important parts of this dissertation. Temperatures from 6 to about 300 K can be accomplished with the help of a special cryostat equipped with an optical window. Annealing of the samples is performed with a special sample holder which can be heated from RT (room temperature) to about 800 K by a tungsten filament. Samples are fixed on a copper groove which is near the heater. The annealing temperature is measured with a thermocouple meter just below the copper groove. In order to avoid oxidization and destruction of the samples, this sample holder is located in a small vacuum chamber with a pressure of around 2×10^{-4} Pa during annealing. The small vacuum chamber has an optical window and is connected with a rotary-pump through a flexible vacuum tube, so that it can be moved between the magnetic poles in small steps by a screw micrometer and the wedged sample can be investigated during the heat treatment.

2.4 Brillouin Light Scattering

Another effective method to investigate magnetic properties in ultrathin magnetic layers is Brillouin light scattering (BLS).

The experimental arrangement of light scattering from low frequency spin waves in thin magnetic films is shown in fig.2.3. The frequency shifts of the scattered light are related to the magnetic properties of the magnetic thin film systems. The BLS , thus, can be used to investigate magnetic anisotropies in single magnetic films, and interlayer coupling in magnetic double layers [2.4].

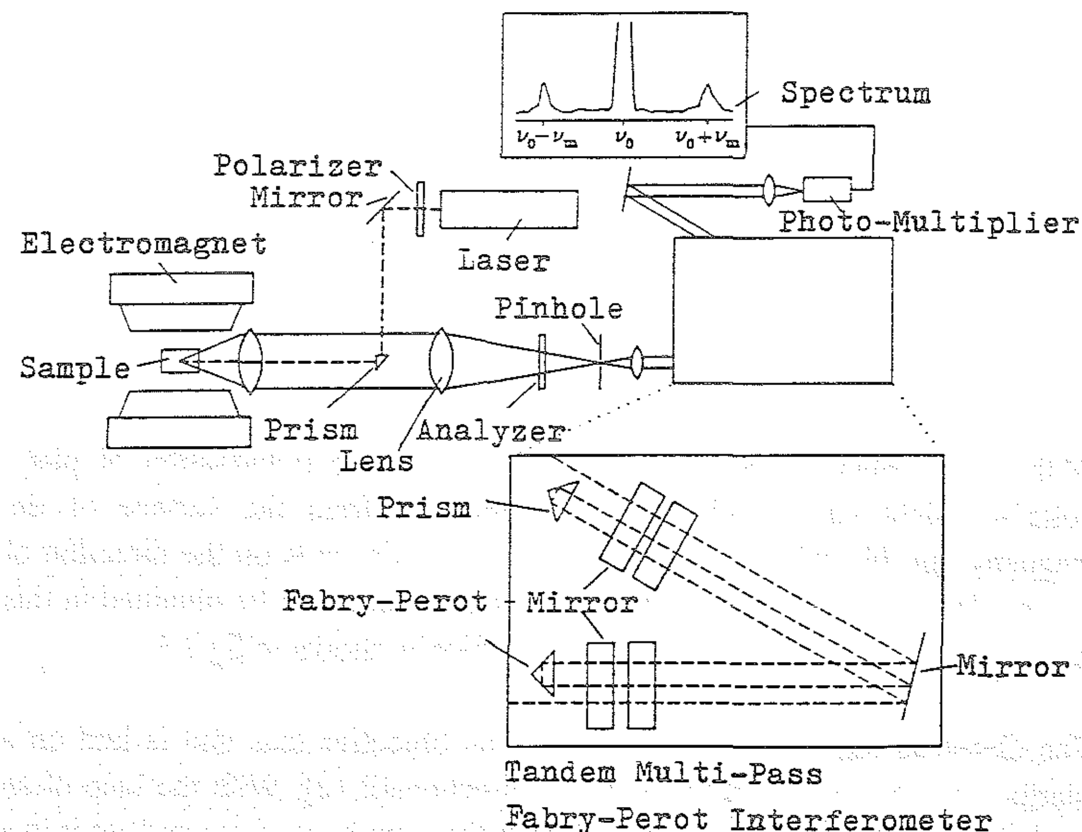

Fig.2.3 Experimental Arrangement for Light Scattering from Spinwaves Using a Back Scattering Geometry (after Wolf [2.3])

A monochromatic, linearly polarized light wave with a wavelength of λ =5145 Å emitted from an argon ion laser is adopted to excite magnons in magnetic thin film specimens. The specimen is put between the poles of an electromagnet with its plane parallel to the direction of the applied magnetic field. The back scattering geometry is employed, i.e. the lens used to focus the incident laser beam on the sample surface collects the scattered light at the same time. The incident angle of the light is 45°, so only a small part of the incident light is inelastically scattered from the sample and collected. Most of the light is elastically reflected. The inelastically scattered light carries the signals from spin waves in the studied structures. Due to the magneto-optical interaction of light and magnon, the polarization plane of the scattered light will rotate by 90° [2.5]. If one sets the analyzer to 90° with respect to the polarizer, the elastically scattered light from roughness as well as the inelastically scattered light from phonons can be greatly reduced. Then by means of a set of lenses a parallel beam of the scattered light is produced. After that a Tandem Multi-Pass Fabry-Perot interferometer[2.6] is used to obtain the spectrum of the scattered light, in order to observe the components with low frequency shifts from spin waves. Finally , the signals are amplified by a photo-multiplier and the spectrum is accumulated in a computer.

2.5 Kerr Microscope

With a Kerr microscope (KM) the rotation of the polarization of plane polarized light can be observed on reflection from the surface of the magnetic thin films[2.8, 2.9]. Since the rotation depends on the direction of the magnetization, a picture of the magnetic domains can be obtained in this way. A schematic diagram for KM observation is shown in fig.2.4.

The observed magnetic sample is under an objective lens and is laid on a platform which can be moved in three directions[2.10]. With the help of an ocular one can monitor the sample, adjust the sample platform and set it in a suitable position. The plane of the incident polarized light on reflection from a magnetized film is elliptically polarized, but that this polarization plane is parallel or perpendicular to the incident plane is also plane polarized. Most of our samples are of plane magnetization. Domain configurations in terms of longitudinal and transverse Kerr effect will be observed in these systems. A video camera is used to monitor the domain patterns. Also, this KM is equipped with a digital system for image treatment. With this system either the saturation state or the demagnetization state of the magnetic specimen is stored as a reference picture and later on substracted from the real picture. In order to get rid of noise 3600 Kerr pictures can be accumulated. Therefore, it is possible with this system to study the weak signals from ultrathin magnetic films.

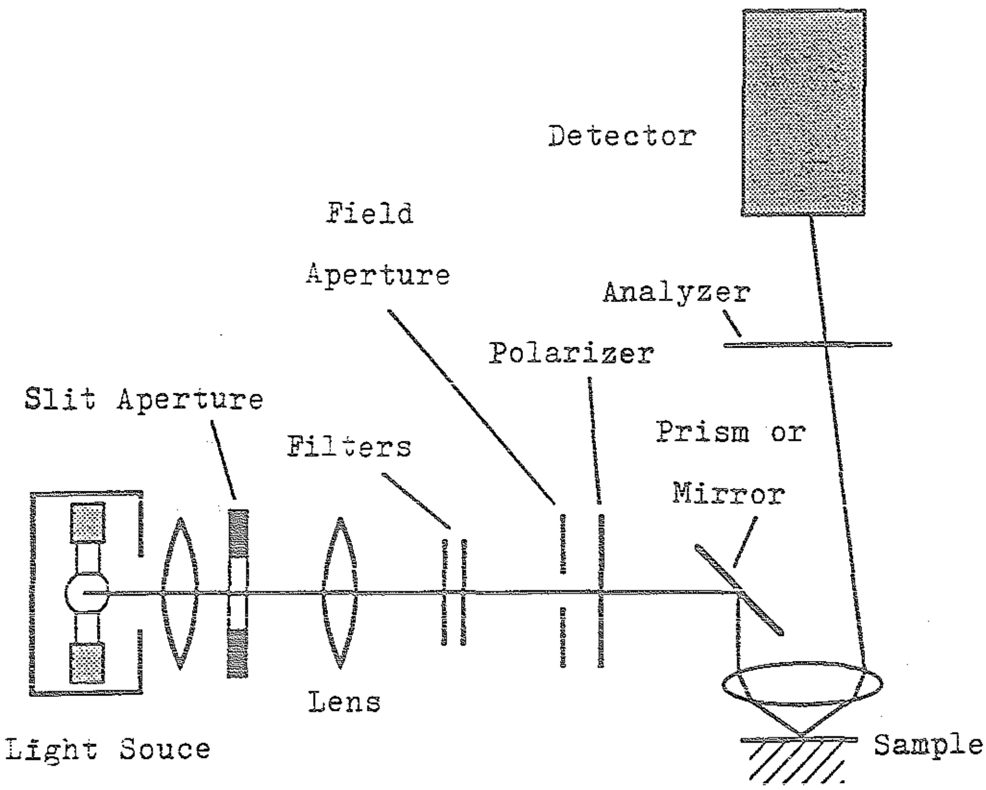

Fig.2.4 Schematic Diagram of the Kerr Microscope for domain observation (after Hubert [2.7])

2.6 Magnetoresistance Measurement

GMR effect in the sandwich structures is observed with a four-point technique as indicated in fig.2.5. The GMR samples are made in a special geometry as seen in the right-up panel of fig.2.5. During the measurement the sample is located in an homogeneous applied field supplied by the electromagnet which is the same as that in MOKE measurements and can vary the magnetic field in two directions. A DC power source provides a constant electric current between the A and B point of the sample and a digital voltmeter is used to take the potential difference between the C and D point. The varying field will be simultaneously measured by a Gauss-meter including a Hall probe which is near the sample. Collecting these two signals by a computer, the resistance versus magnetic field is obtained.

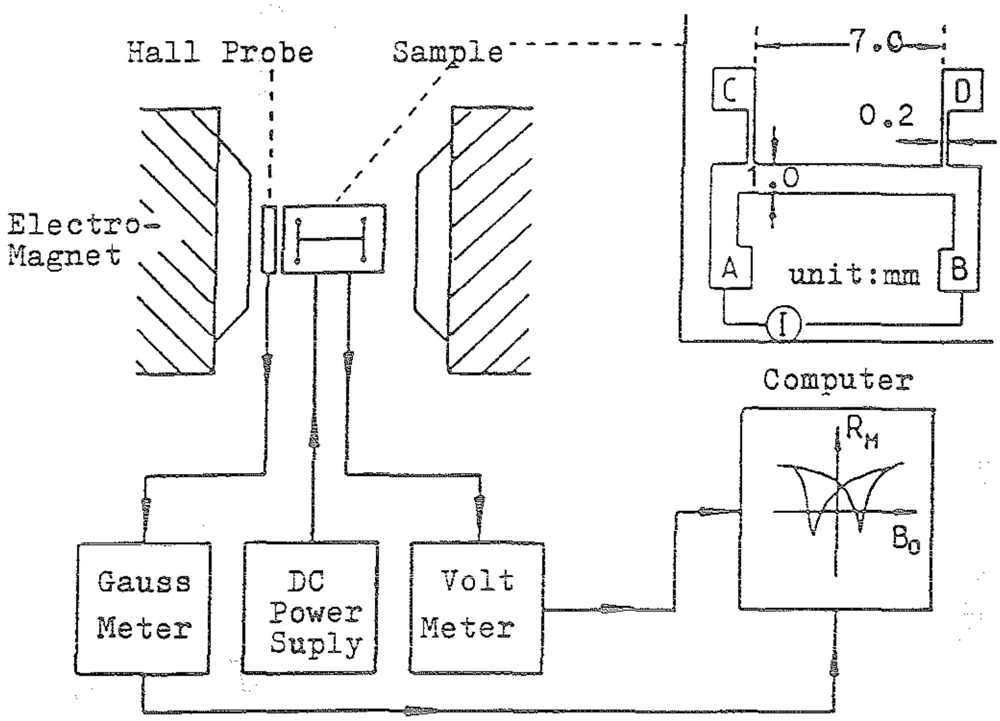

Fig. 2.5 Schematic Diagram for Magnetoresistance Measurement (after Binasch[2.11] and Walz[2.12])

2.7 References

[2.1] J.A.Wolf, Dissertation, Universität zu Köln (1993), and Jül- 2743, Forschungszentrum Jülich GmbH, März 1993.

[2.2] J.A.Wolf, Diplomarbeit, IFF, KFA-Jülich, Uni Münster (1989).

[2.3] H.A.Fuß, Dissertation, Universität zu Köln (1993), and Jül-2740, Forschungszentrum Jülich GmbH, März 1993.

[2.4] P.Grünberg, «Topics in Applied Physics», Vol. 66, edited by M. Cardona and G. Güntherodt, Springer Verlag Berlin-Heidelberg-New York (1989).

[2.5] Ch. Kittel, Phys. Rev. 73 (1948) 155.

[2.6] J.R.Sandercock, «Operation Manual for Tandem Interferometer», (1980).

[2.7] A.Hubert, «Magnetic Domains», to be published.

[2.8] A.Hubert and J.Kranz, Zeitschrift für angewandte Physik, 15 (1963) 221.

[2.9] B.D.Cillity, «Introduction to Magnetic Materials», Addison-Wesly-Publishing, Reading (1972).

[2.10] R.Mosler, Diplomarbeit, Universität zu Köln (1991).

[2.11] G.Binasch, Diplomarbeit, Universität zu Köln (1988).

[2.12] U.Walz, Dissertation, Universität zu Köln (1989), and Jül-2272, Forschungszentrum Jülich GmbH, März 1989.

3 Theory Background and Characterization of Magnetic Interlayer Coupling

With 7 Figures

3.1 Introduction

As mentioned , in this work the magnetic interlayer exchange coupling between iron layers across non-magnetic interlayers is studied. Fig. 3.1 shows the structure of the investigated samples, which were prepared by MBE and characterized by means of RHEED, LEED and AES analytical techniques. Crystalline GaAs(001) is used as substrates. A wedge-shaped interlayer is often used for the research. It has the advantage that different interlayer thicknesses can be inverstigated on one specimen with identical iron films. Three kinds of magneto-optical techniques are employed to study the MIC (magnetic interlayer coupling). In this chapter, characterization of the MIC with these methods, relations between the exprimental methods and the experiments and a phenomenological expression for the MIC are described (see fig.3.2).

3.2 Phenomenological Description of the Magnetic Interlayer Coupling

If the two iron layers are considered to have the same thickness, the total energy density of a magnetically coupled double layer system , as shown in fig. 3.1, may be written as follows[3.1-3.4]:

$$E = -\mu_0 H M_s(\cos\phi_1 + \cos\phi_2) + \frac{K_1}{4}(\sin^2 2\phi_1 + \sin^2 2\phi_2)$$

$$-\frac{J_1}{d_{Fe}}\cos(\phi_2 - \phi_1) - \frac{J_2}{d_{Fe}}\cos^2(\phi_2 - \phi_1) \tag{3.1}$$

Here the first term describes the Zeeman energy density, the second term the crystalline anisotropy and the last two terms are the contributions of the magnetic interlayer coupling. Here ϕ_1 and ϕ_2 are the angles between the magnetizations of the individual iron layers and the external field $\vec{H}$, M_S is the saturated magnetization, K_1 the crystalline anisotropy constant of the iron films and μ_0 the permeability constant for free space. J_1 and J_2 are the phenomenological parameters for bilinear- and biquadratic coupling, respectively. In the literature other parameters A_{12} and B_{12} are also used, where $J_1=2A_{12}$ and $J_2=2B_{12}$. In this work J_1 and J_2 are adopted, since they seem to be more widely accepted.

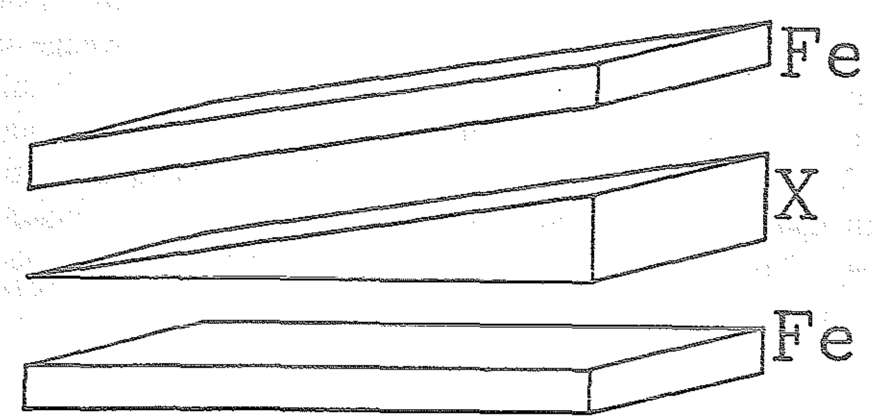

Fig. 3.1 Epitaxial Sandwich Structure, two Magnetic layers (Fe) with Identical Magnetizations (M_S) and a Wedge-shaped Interlayer X (non-magnetic metal layers)

In principle, the orientations of the two magnetizations in the Fe films versus the external field can be calculated under the condition that the minima of the total energy of the system are always reached. In the usual way by evaluation of equation 3.1 and its derivatives with respect to ϕ_1

and ϕ_2 under the above assumption, the phenomenological parameters and the directions of the magnetic moments will be found[3.5].

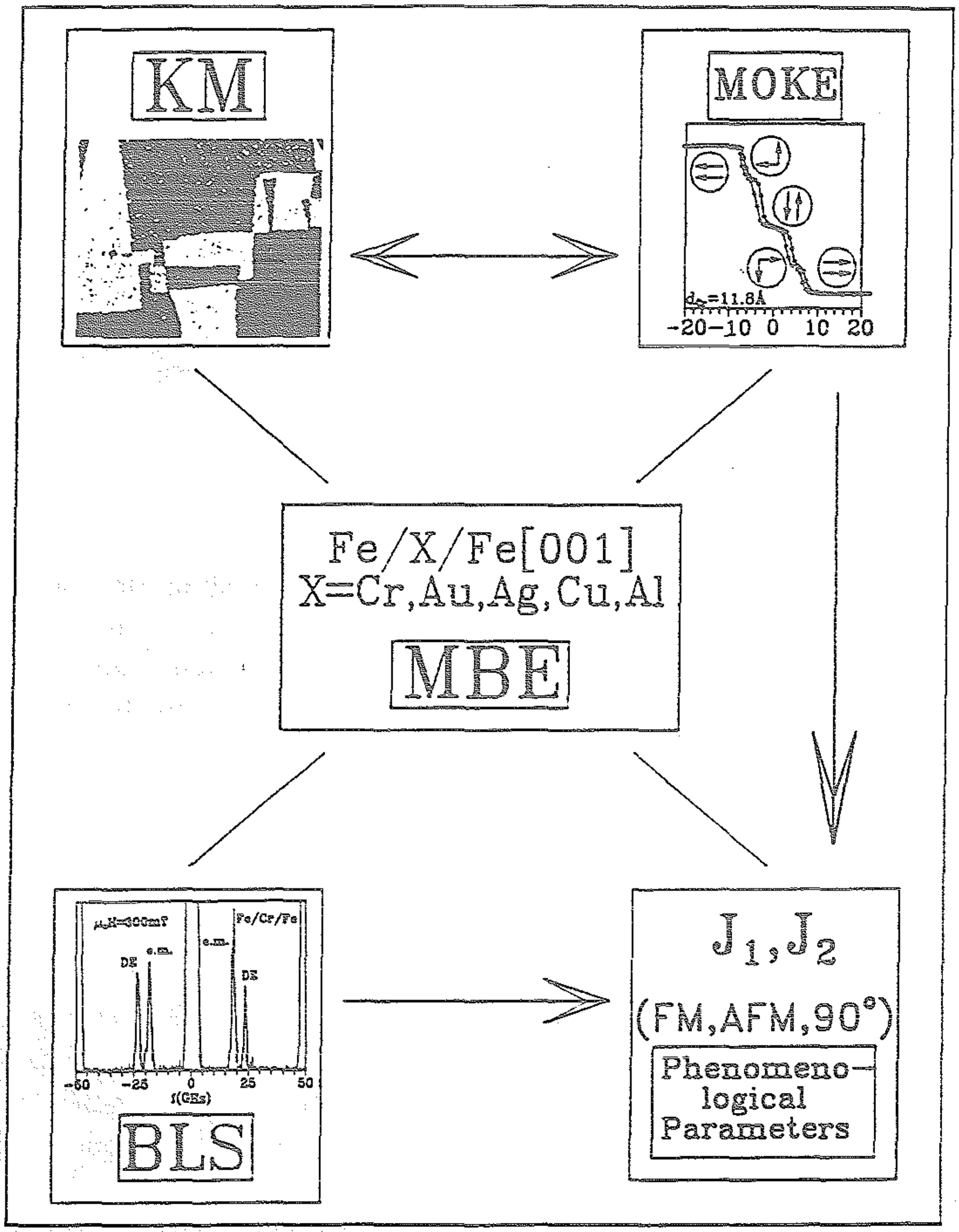

Fig. 3.2 Schmatical Diagram of the Relations Among the Experimental Methods and the Phenomenological Description

Up to now, three totally different kinds of magnetic interlayer coupling are known. These are ferromagnetic (FM), antiferromagnetic (AFM) and 90°-type coupling, in which the two magnetic moments of the Fe layers prefer parallel, antiparallel and perpendicular alignment, respectively, without applied magnetic field. The relations between the parameters (J_1 and J_2) and the coupling types can be obtained by a theoretical analysis of equ. 3.1. These relations can be described in four cases.

1. $J_1>0$ and $J_2\geq 0$:
   FM coupling (parallel alignment of the magnetizations)
2. $J_1<0$ and $J_2>J_1$:
   AFM coupling (antiparallel alignment of the magnetizations)
3. $J_2<0$ and $J_2\leq J_1$:
   90°-type coupling (perpendicular alignment of the magnetizations)
4. $J_1=0$ and $J_2=0$:
   no coupling (the orientations of the individual magnetizations in the two magnetic layers are independent)

Generally, the two parameters, J_1 and J_2, can describe all of the coupling types as indicated above. It depends on their relative strengths, the size of the external field and what the orientation of the film magnetizations will be. The so-called 90°-type coupling does not mean only biquadratic coupling, for it may include bilinear coupling as well. Similarly, the normally called FM and AFM coupling are not identical to the bilinear coupling, since they may have the contribution of the biquadratic one.

3.3 Characterization of MIC from MOKE

MOKE allows one to measure the hysteresis loops (M(H) curves) in magnetic double layers. Some examples of the M(H) curves measured for Fe/Ag/Fe(001) and Fe/Cr/Ag/Cr/Fe(001) systems are given in the upper panel of fig. 3.3 and fig. 3.4. As mentioned in the last section, the M(H) curves can be numerically calculated in the situations of minimizing the total energy (equ. 3.1). The calculated curves are shown just below the corresponding experimental hysteresis loops in the two figures.

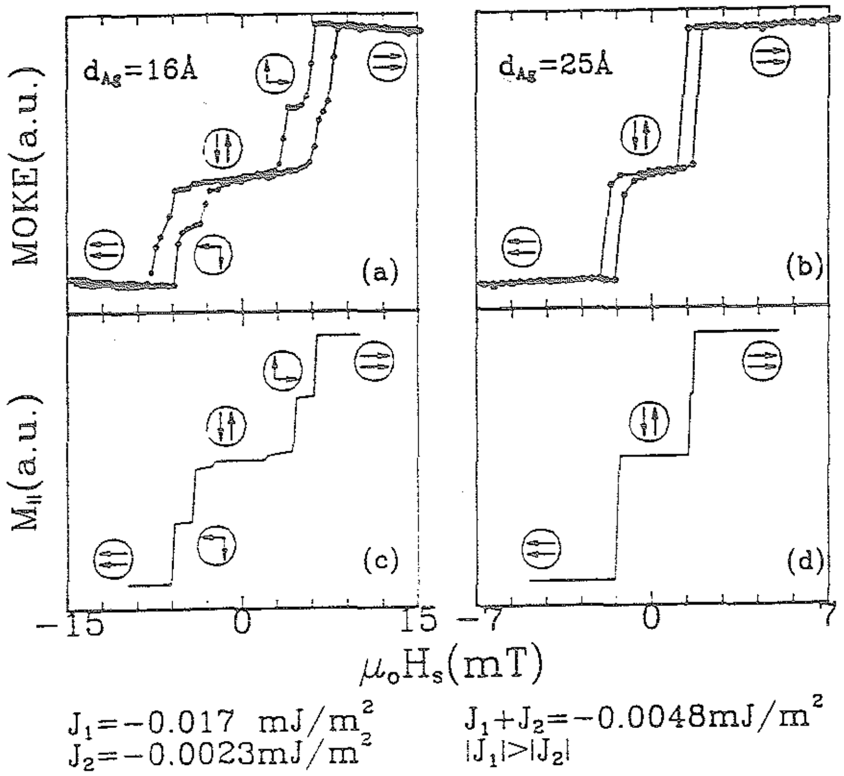

Fig. 3.3 Experimental (a and b)and Calculated (c and d) Hysteresis Loops for Fe(20Å)/Ag(16Å)/Fe(20Å) and Fe(20Å)/Ag(25Å)/Fe(20Å) layered systems. Arrows Inside Circles Indicate the Orientations of the Magnetizations.

Fig. 3.3 shows two types of AFM coupling. The curve in fig. 3.3(a) gives also a plateau at the $M \cong M_S/2$ position as well as a plateau at $M \cong 0$. It means that there is some contribution from the biquadratic coupling component in this case. Fig. 3.4 shows a strong AFM coupling (a) and a 90° alignment type coupling (b). Due to the crystal anisotropy, rotation discontinuities of the magnetizations occur during these magnetization process as long as the saturation field $\mu_0 H_S$ which needs to parallelly align the magnetizations is sufficiently smaller than the crystal anisotropy field B_a ($\cong$60 mT). These is the case in fig. 3.3(a), (b) and fig. 3.4(b). If $\mu_0 H_S \gg B_a$, a continuous rotation takes place like in fig. 3.4(a).

The parameters J_1 and J_2 obtained from the best fitting are given below the corresponding curves in the figures too. The orientations of the magnetizations versus the applied field can be found by fitting the experiment with equ. 3.1 and a set of the parameters can be obtained.

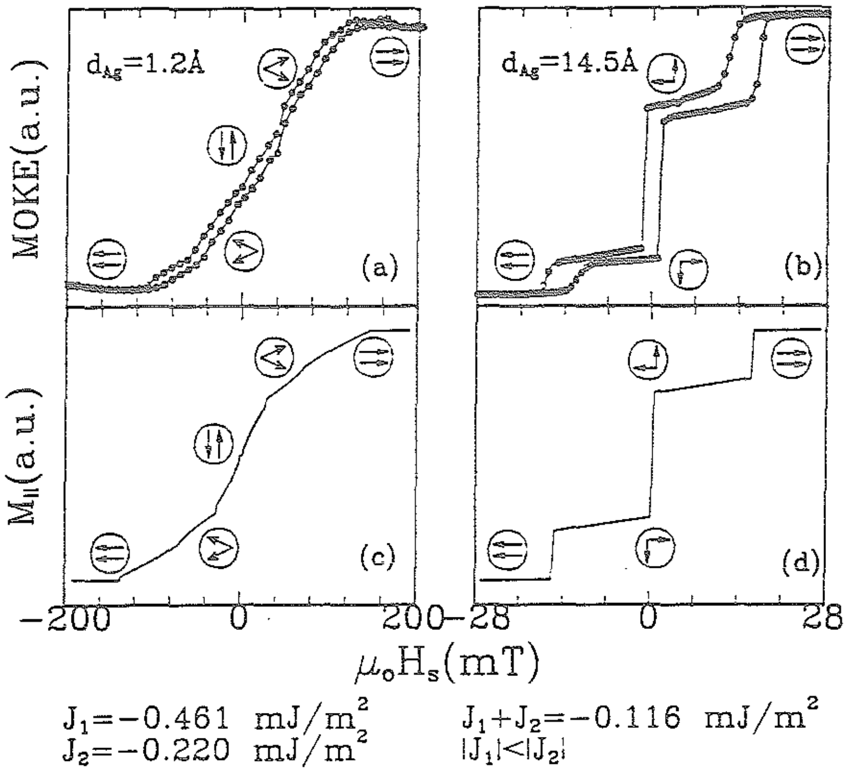

Fig. 3.4 Experimental (a and b)and Calculated (c and d) Hysteresis loops for Fe(20Å)/Cr(5Å)/Ag(1.2Å)/Cr(5Å)/Fe(20Å) and Fe(20Å)/Cr(5Å)/Ag(14.5Å)/Cr(5Å)/Fe(20Å) layered systems. Arrows Inside Circles Indicate the Orientations of the Magnetizations.

However, J_1 and J_2 , usually, can not be separated and only the sum of J_1 and J_2 can generally be obtained. Only for some special case like curve in fig. 3.3(a) and fig. 3.4(a) one may get the parameters separately. According to the report in ref. 3.6, by preparing different thicknesses of the iron layers in the sandwiches, one can separated these two parammeters for the AFM- and 90°-type coupling.

3.4 Characterization of MIC by KM

With the help of the KM (Kerr microscopy) one can directly observe the coupling qualitatively via domain configurations. An example for a Cr spacer system is given in fig. 3.5, where the upper pictures were taken from KM observation and the lower part is the interpretation with respect

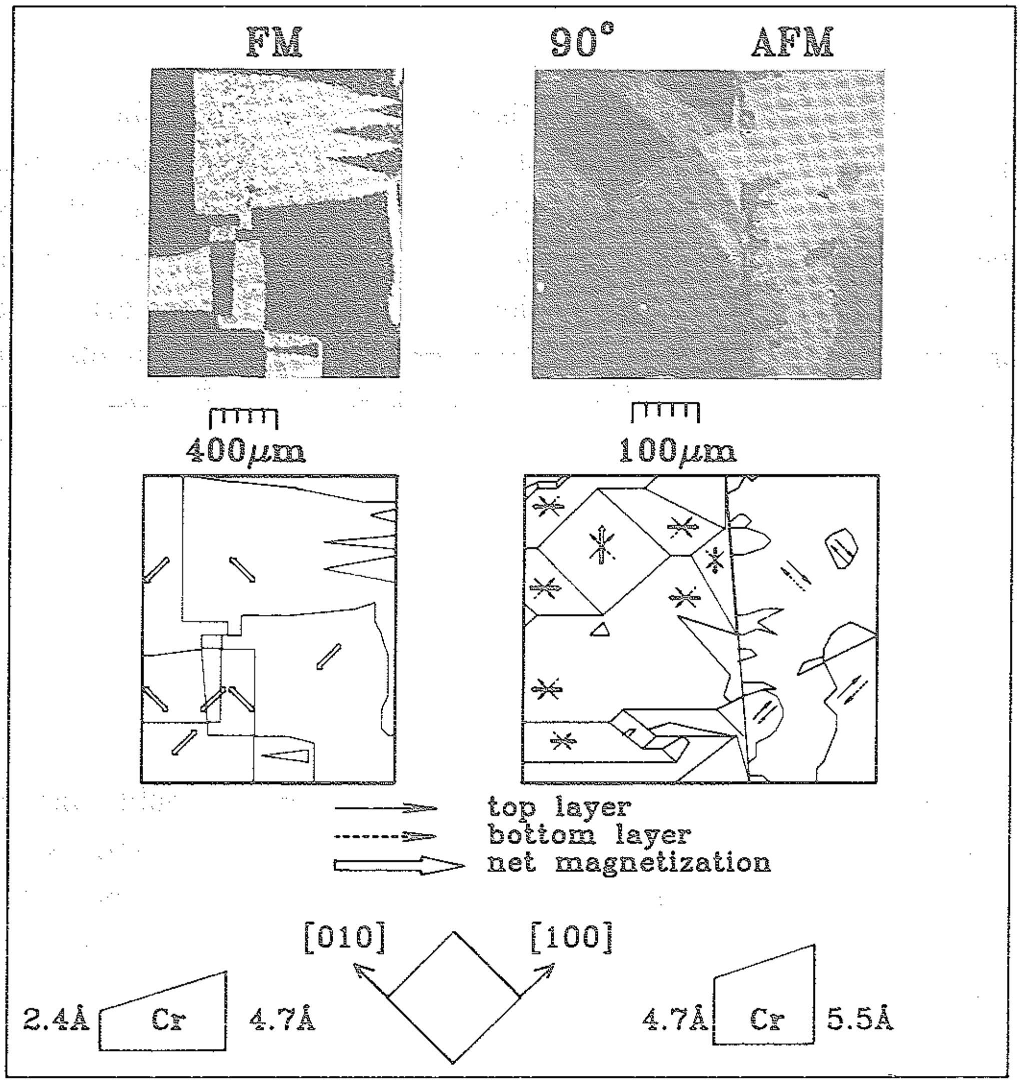

Fig. 3.5 Domain Patterns Taken from Fe(100Å)/Cr/Fe(100Å) Sample with a Wedge Type Interlayer. The Ranges of the Cr Wedge are Indicated

to the orientations of the magnetizations. Since we are dealing with good expitaxial crystal layered structures, there are two easy axes within the

(001)-plane in the Fe layers. Without applied field the moments orient themselves always along the easy axes. Since there are four possible orientations of the magnetization in each iron layer, there is a certain number of possible combinations in such double magnetic layers. Due to the Kerr contrast, different orientations of the two magnetizations will give different gray scales. Therefore, from the gray scales the coupling can be evaluated[3.7].

In domain configurations domain walls are formed in accordance with the principle of free stray field. In both FM and 90°- type ranges, regular domain structures and domain walls are clearly seen, but the wall orientations are different. In the FM zone the magnetizations maintain the easy axes, but the net magnetizations in the 90°-type zone orient along the hard axes due to the perpendicular alignments of the moments. Thus, 90° and 180° domain walls are oriented along the hard axes and easy axes in the FM zone, respectively, while in 90°-type coupling zone they are rotated by 45° for the two kinds of domain walls. In the AFM zone irregular domain configurations can be oberved due to the zero net magnetizations.

3.5 Characterization of MIC from BLS

Fig. 3.6 gives an example of BLS spectrum from a double magnetic layer, which includes two kinds of modes, i.e. DE (Damon-Eshbach) mode[3.8] or surface mode, and e.m. (exchange mode) or bulk mode. The frequency shifts for the DE and e.m. modes as a function of interlayer thickness in a Fe/Cr/Fe(001) wedge type system are shown in fig 3.6(a).

The spin wave frequencies in the double magnetic layers can be determined by evaluation of the Landau-Lifshitz dynamic equation[3.9-3.11]. The Landau-Lifshitz equation of motion without damping term may be written as the following form[3.12]:

$$\frac{\partial \bar{M}_j(\bar{r},t)}{\partial t} = \gamma_j \bar{M}_j(\bar{r},t) \times \bar{B}_{eff,j}(\bar{r},t) \qquad (3.2)$$

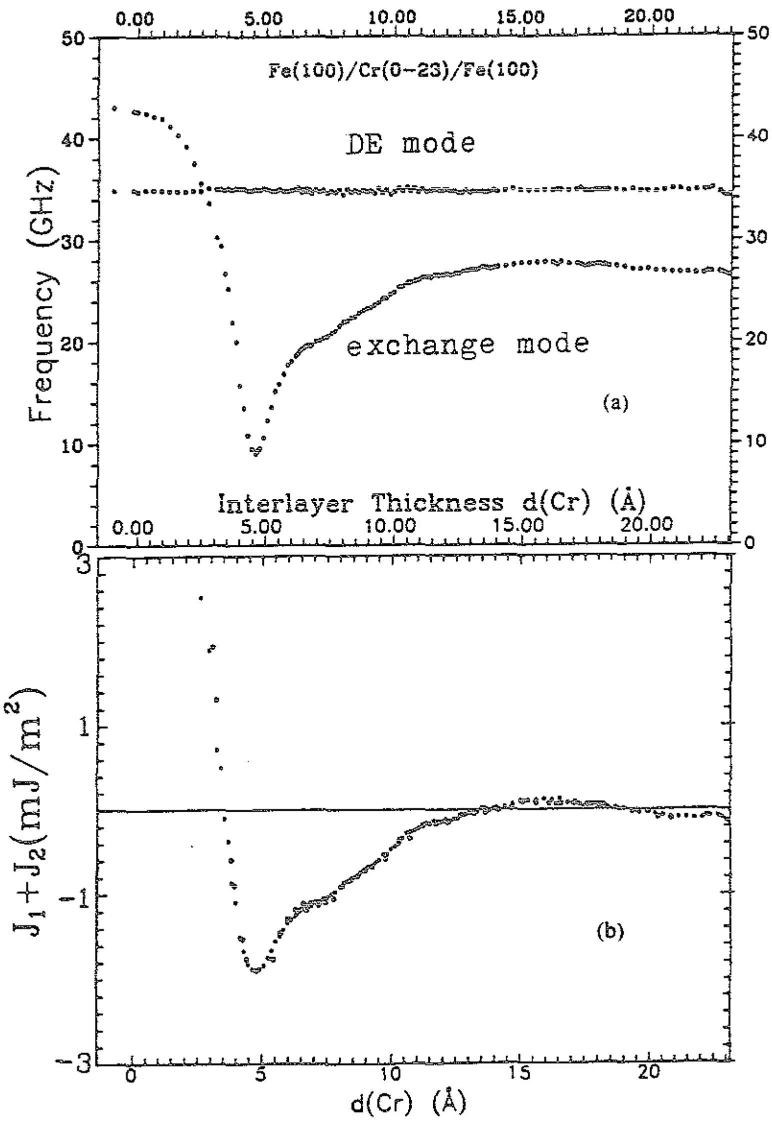

Fig. 3.6 (a) Frequency Shifts of the Spinwaves Versus the Interlayer Thickness in Fe(100Å)/Cr(0-23Å)/Fe(100Å) System. Applied Field is 0.4T and along an easy axis. (b) Thickness Dependence of MIC Evaluated by the Theoritical Analysis; Solid Points (•) for the Sample of Fe(100Å)/Cr(0-23Å)/Fe(100Å) and Cross Markers (×) for Sample of Fe(100Å)/Cr(0-22Å)/Fe(100Å)

where $j=1,2$ indicate the two magnetic layers, $\vec{r}$ and t are the space vector and time, respectively, γ_j the gyromagnetic ratio, $\vec{M}_j$ magnetization of the Fe layers, and the effective induced magnetic field $\vec{B}_{eff,j}(\vec{r},t)$ is given as[3.12,3.13]:

$$\bar{B}_{eff,j}(\bar{r},t) = \mu_0\bar{H}_j(\bar{r},t) + \frac{2A_j}{M_{s,j}^2}\nabla^2\bar{M}_j(\bar{r},t) \qquad (3.3)$$

where A_j is the exchange constant, $\bar{H}_j$ the effective magnetic field in the j-th Fe layer. The second term in equ. 3.3 expresses the effective exchange field of magnetic moments.

The following Rado-Weertman boundary conditions[3.14] are considered:

$$\frac{2A_j}{M_{s,j}^2}\bar{M}_j(\bar{r},t)\times\frac{\partial\bar{M}_j(\bar{r},t)}{\partial\bar{n}} - \frac{2K_{s,j}^{(e)}}{\bar{M}_j(\bar{r},t)^2}(\bar{M}_j(\bar{r},t)\bullet\bar{n})(\bar{M}_j(\bar{r},t)\times\bar{n}) = \bar{0}$$

(3.4)

where $K_{s,j}^{(e)}$ indicates the surface anisotropy in j-th Fe film, and $\bar{n}$ is the normal unit vector of the layered system.

The parameters, J_1 and J_2, are brought in by appling the Hoffmann boundary conditions[3.15,3.16]:

$$\frac{A_1}{\bar{M}_1^2}\bar{M}_1\times\frac{\partial\bar{M}_1}{\partial\bar{n}} - \frac{1}{2}\bullet\frac{J_1+J_2}{|\bar{M}_1|\bullet|\bar{M}_2|}\bar{M}_1\times\bar{M}_2 - \frac{K_{s,1}^{(i)}}{\bar{M}_1^2}(\bar{M}_1\bullet\bar{n})(\bar{M}_1\times\bar{n}) = \bar{0}$$

(3.5)

$$\frac{A_2}{\bar{M}_2^2}\bar{M}_2\times\frac{\partial\bar{M}_2}{\partial\bar{n}} + \frac{1}{2}\bullet\frac{J_1+J_2}{|\bar{M}_1|\bullet|\bar{M}_2|}\bar{M}_1\times\bar{M}_2 - \frac{K_{s,2}^{(i)}}{\bar{M}_2^2}(\bar{M}_2\bullet\bar{n})(\bar{M}_2\times\bar{n}) = \bar{0}$$

(3.6)

where $K_{s,j}^{(i)}$ (j=1,2) indicates the interface anisotropy . In addition, the magnetostatic boundary conditions are applied:

$$\bar{B}_{e\perp} = \bar{B}_{i\perp} \qquad (3.7)$$

$$\bar{H}_{e\,II} = \bar{H}_{i\,II} \qquad (3.8)$$

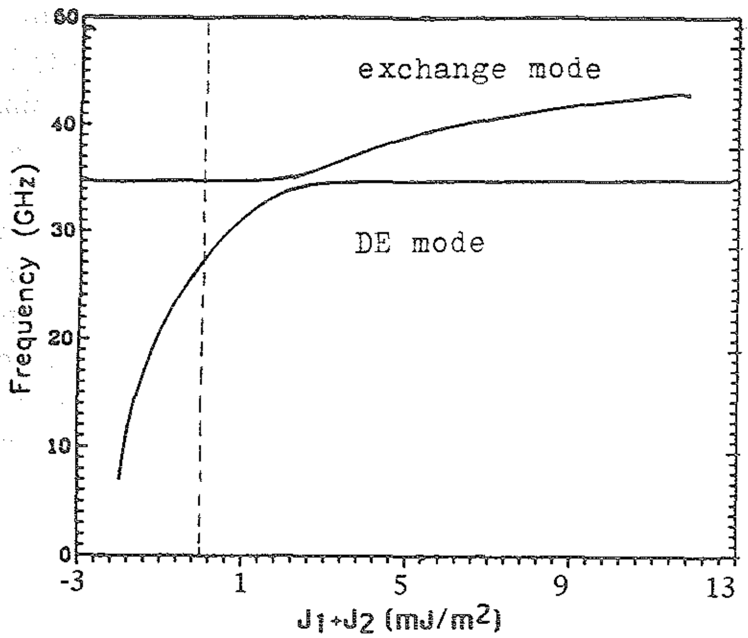

Fig. 3.7 Frequencies of DE- and e.m. Modes Versus Magnetic Interlayer Coupling . The dashed line indicates the uncoupled point. The Following Parameters Were Used for the Calculation:

$A_1=A_2=2.00\times10^{-11}$ J/m; $d_{Fe}=100$Å; $g_1=g_2=2.10$;

$K^{(i)}_{s,1} = K^{(i)}_{s,2} = 0$; $K^{(e)}_{s,1} = K^{(e)}_{s,2} = 0$;

$M_s=1.65\times10^6$ A/m; $K_1=4.80\times10^4$ J/m^3; $\mu_0H_0=0.4$ T

where index e and i indicate the two surfaces of the magnetic films.

Concerning the Landau-Lifshitz equation (3.2) and the boundary conditions (equ. 3.3 - 3.8) together, a set of 12 linear homogenous equations are obtained, which characterize the spinwave frequencies[3.10,3.11].

Fig. 3.7 shows the coupling strength dependence of the frequency shifts obtained by the theoritical analysis. Using the theoritical curves to fit the experimental results of fig. 3.6(a), magnetic interlayer coupling versus the spacer thickness can be found as given in fig. 3.6(b).

3.6 Discussion

To characterize the MIC, all of the three methods described above have the advantage that they can be applied to wedged interlayers due to the of individual characteristic. The MOKE is easily used to measure hystereses, to evaluate the coupling parameters and sometimes to be able to separate the bilinear and biquadratic coupling with equ. 3.1, but this method has a disadvantage that the evaluation of the hystereses does not result in any information about the FM coupling in the normal double layered systems. It is, however, possible to evaluate the FM coupling by MOKE using a specially constructed sample (spin engneering)[3.17]. The inelastic BLS can only yield the total coupling strength by evaluation of the equations discussed in section 3.5, but it has the advantage of evaluating also FM type interlayer coupling. With KM one can directly observe the MIC in a qualitative method, but it can be mutually complementary with MOKE measurements, in order to confirm the coupling types. For example, the KM can be used to distinguish the effect in hystereses which is due to AFM coupling or due to the uniaxial anisotropy effect. In addition, the KM may be used to observe the uncoupled state.

3.7 References

[3.1] F.Hoffmann, A.Stankoff, H.Pascard, J. Appl. Phys. 41 (1970) 1022.

[3.2] M.Rührig, R.Schäfer, A.Hubert, R.Mosler, J.A.Wolf, S.Demokritov, P.Grünberg, Phys. Stat. Sol. (a) 125 (1991) 635.

[3.3] A.Fuß, S.Demokritov, P.Grünberg, W.Zinn, J.Magn. Magn. Mat. 103 (1992) L221.

[3.4] Q.Leng, J.A.Wolf, P.Grünberg, W.Zinn, Proc. of Int. Conf. on the Phys. of Trans. Met., Darmstadt, Germany 1992, p.434, World Scientific 1993.

[3.5] A.Fuß, Dissertation, Universität zu Köln (1993), and Report in Research Center Jülich (KFA), Jül-2740, März 1993.

[3.6] B.Heinrich, Z.Celinski and J.F.Cochran, Workshop on "Magnetism and Structure of Reduced Dimension", Cargese, Corsica, France, June 1992, to be published in NATO ASI series.

[3.7] A.Hubert, "Magnetic Domains", to be published.

[3.8] K.W. Damon and J.R.Eshbach, J. Phys. Chem. Sol. 19 (1961) 308.

[3.9] P.Grünberg, in Topics in Applied Physics Vol.66, Hrsg.: M. Cardona, G. Güntherodt, Springer Verlag (1989).

[3.10] M.Vohl, Dissertation, Universität zu Köln (1991), and Report in the Research Center Jülich (KFA), Jül-2434, Jan. 1991.

[3.11] M.Vohl, J.Barnas and P.Grünberg, Phys. Rev. B, 31 (1989) 12003.

[3.12] W.Döring, Handbook of Physics, Bd. 18 Teil 2, Berlin-Heidelberg-New York, Springer 1966.

[3.13] P.Hansen, Diplomarbeit, Universität Hamburg, 1965.

[3.14] G.T.Rado and J.R.Weertman, J. Phys. Chem. Sol., 11 (1959) 315.

[3.15] F. Hoffmann, Phys. Stat. Sol. 41 (1970) 807.

[3.16] G.Spronken, A.Friedmann and A.Yelon, Phys. Rev. B 15 (1977) 5141.

[3.17] S.S.P.Parkin, Workshop on "Magnetism and Structure of Reduced Dimension", Cargese, Corsica, France, June 1992, to be published in NATO ASI series.

4. Light Scattering from Ultrathin Iron Films

With 7 Figures

4.1 Introduction

In order to investigate the interlayer magnetic coupling, the quality of the studied specimens plays a very important role. Since the coupling between two iron layers is studied, high quality of the structure of the magnetic bilayers and magnetic properties of thin iron films is desired. In addition, in recent years magnetism at surfaces and magnetism in ultrathin films have become fascinating and intense fields of research[4.1-4.4]. However, it is recognized that both experimental and theoretical investigations are difficult and sometimes lead to controversy. The reason is that the properties of the surface and ultrathin films are very sensitive to the conditions of sample preparation and to the adjacent materials, such as substrate, coating layer and contamination, etc. In this chapter the study of magnetic properties of thin Fe films with thicknesses of from 1.5 to 16 monolayers (ML) by means of BLS and MOKE were described, knowledge of which will also help for the research of interlayer coupling in the following chapters.

4.2 Experimental Aspect

4.2.1 Growth and Characterization of Ultrathin Iron Films

Sample preparation was carried out on the basis of a known recipe[4.5,4.6]. The samples were made in UHV by MBE (fig.2.1) and characterized with AES, LEED and RHEED.

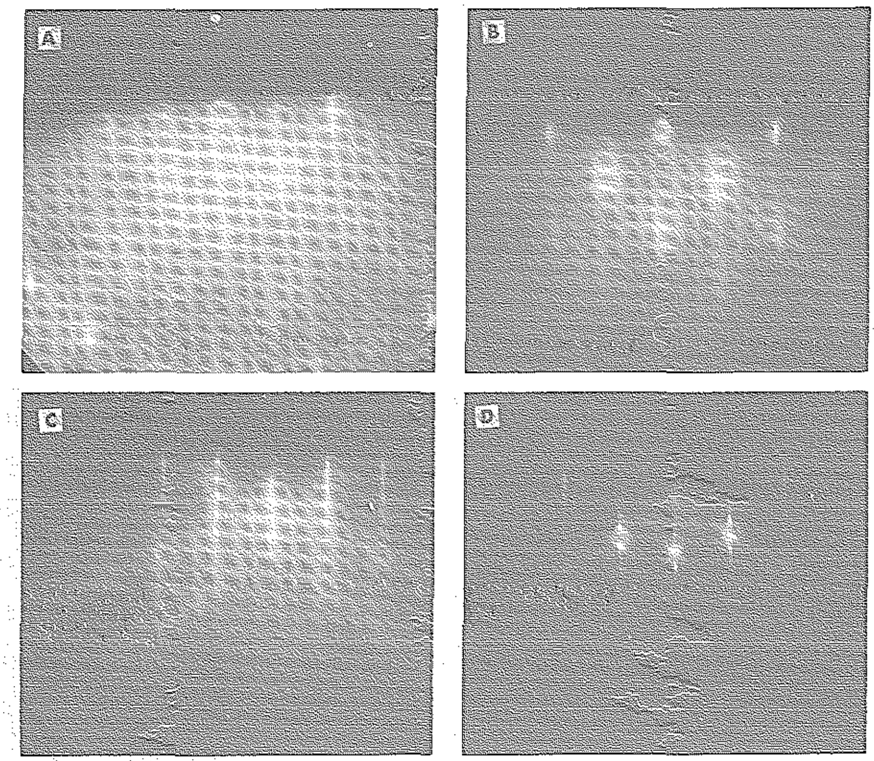

Fig.4.1 RHEED Patterns from Surface of (A) Crystal GaAs(001) Substrate; (B) Iron Seed Layer; (C) and (D) Ag Buffer Layer before Annealing and after Annealing at 573K for 1 Hour, respectively.

A crystal GaAs (001) was used as substrate. It was first cleaned in an ultrasonic bath, then cooked for a few minutes in boiling propanol and dried in propanol vapour. After transfered to the main chamber(growth chamber) of the UHV system, the substrate was degased at 853K for one hour in order to remove oxygen and the other contamination on the crystal surface. This was verified by AES. And the surface structure was characterized by LEED and

RHEED (fig.4.1 A). To reach ideal epitaxial growth and to obtain iron crystal films of high quality, good match in lattices between film and substrate is an essential condition. However, there is about 1.4% mismatch between GaAs (001) and bcc Fe (001) lattices. Thus, if the Fe is directly deposited on the GaAs, a lot of dislocations and strain in the sample plane may be induced. Then a good epitaxial growth is impossible and even the Fe may alloy with the substrate[4.7,4.8]. In order to solve this problem, a buffer layer was introduced.

Before deposition of the buffer layer a 10Å thick seed layer of Fe at a substrate temperature T_s=373K at a rate V_r=0.1Å/sec was evaporated, in order to keep the [001] orientation and to cure some roughness on the GaAs surface. The RHEED pattern for the seed Fe film is shown in fig.4.1B. It is obvious that the surface of Fe is rather rough. The relative larger spots come not only from reflection at the surface, but also from transmission through steps at the rough Fe surface, and are not on the arc[4.9].

Ag was chosen as the buffer layer, because its nearst neighbour distance within the (001)-plane which is 2.89Å is very near that of Fe which is 2.87Å. Although Ag has fcc structure, there is a good match to Fe because the lattice constant of Ag (in [100] or [010]) is 4.09Å. Half of the diagonal line in the [110] direction of the Ag (001) surface is 2.89Å which is close to the lattice constant of bcc Fe. Thus, a nearly perfect in-plane lattice match can be achieved in (001) surface epitaxy by rotating the two [100] directions in 45° relative to each other. A 1500Å thick Ag was fabricated on the seed layer at T_s=373K and V_r=1Å/sec and then annealed at 573K for one hour. The growth was monitored by RHEED whose configurations are given in fig.4.1(C) and (D) before and after annealing, respectively. It is clear that the Ag buffer structure was significantly improved after annealing. Before annealing the spots were streaky, and after annealing were still somewhat streaky but lay clearly on an arc which proved the good epitaxial structure and flatness of the surface[4.10]. The additional features are the Kikuchi lines in the pattern.

On the Ag buffer layer the ultrathin Fe film to be studied was evaporated with V_r=0.1Å/sec. The samples were produced with Fe films of variable thickness d_{Fe}. This was achieved by moving the substrate during the deposition of the Fe behind a shutter[4.8]. In this way a wedge-formed Fe film was obtained (see the sample geometry in the lower-right panel of fig.4.2) and its magnetic properties with different thickness of Fe could be investigated on the same sample made under the same conditions. In order to compare the magnetic properties at different preparation conditions, two samples of wedged Fe were made at different substrate temperatures T_s. One sample with a 0-32Å wedge was done at T_s=RT (room temperature) and the other one with a 0-27Å wedge was done at an increasing T_s from RT to 523K.

The Fe wedges were coated with a 20Å-thick Ag layer to stabilize the Fe structures and to protect them from oxidation. Finally, a 500Å ZnS film covered the prepared structure as an antireflection layer to enhance the interaction between the incident light and Fe thin films in the magneto-optical experiment.

4.2.2 Measurement of Magnetic Properties

The BLS was employed to measure the spin wave frequency in ultrathin Fe layers. The wedge-shaped Fe sample was placed on a sample holder which could be moved between two magnetic poles (see fig.2.3) so that the laser beam could reach the different thicknesses of the Fe. To directly measure the in-plane anisotropy, the sample was attached on another holder which could rotate the sample in an angle of from 0 to 360° relative to the external magnetic field. A back-scattering geometry was adopted in which a surface magnon could be detected. The incident light made a 45° angle with the normal direction of the film and perpendicular to the external field. The spinwave vector of the surface magnon involved for 5145Å laser beam is
$k_y=(4\pi/\lambda)\sin45°\cong1.73\times10^7$/m.

Coercive force and its thickness dependence at RT were measured with MOKE.

4.3 Magnetic Properties of Ultrathin Fe Films

Fig.4.2 shows the coercive forces for various thicknesses of Fe layers which were evaluated from the hystereses of Fe films in a in-plane easy axis measured by MOKE. The coercivity decreases as the Fe thickness decreases. The

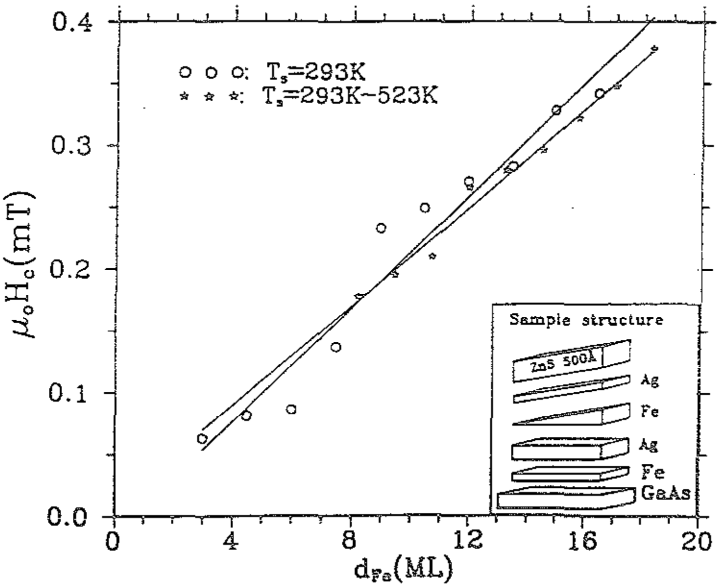

Fig. 4.2 The Thickness Dependence of Coercive Force Measured with MOKE at RT. Substrate Temperatures, T_S, are indicated in the Figure. The lines between Experimental Points just Guide Eyes. The Sample Structures are Schematically Shown in the Lower-right Corner. The lower Fe-film is a seed layer, the upper, wedged Fe film is the sample.

coercive force for the two specimens with different growing temperatures is ≤ 0.4mT. So far to our knowledge, this is the smallest coercivity of single crystal iron films deposited on the GaAs substrate. That means that the magnetic ultrathin layer structures to be prepared and investigated in this work are of quite good epitaxial growth. Of course, a iron whisker has nearly ideal crystal structure with a coercivity of $\mu_0 H_c$=0.05mT[4.11].

Fig.4.3 demonstrates typical magnon spectra measured at RT by BLS in the wedged sample evaporated at RT. The spectra were taken from (a) 2ML and (b) 15ML -thick Fe films under different external magnetic fields. The field was applied in an in-plane [100] direction. With increasing external field the spinwave frequency increases monotonically. It shows that the signal is really originating from magnons. As the thickness of the film is reduced, the frequency at the same applied magnetic field is reduced too. Similar measurements were conducted for other film thicknesses and the same tendency was observed. The spinwave frequencies f as fuctions of the external magnetic field μ_0H and the thickness d_{Fe} of Fe films fabricated at T_s=RT are shown in the fig.4.4.

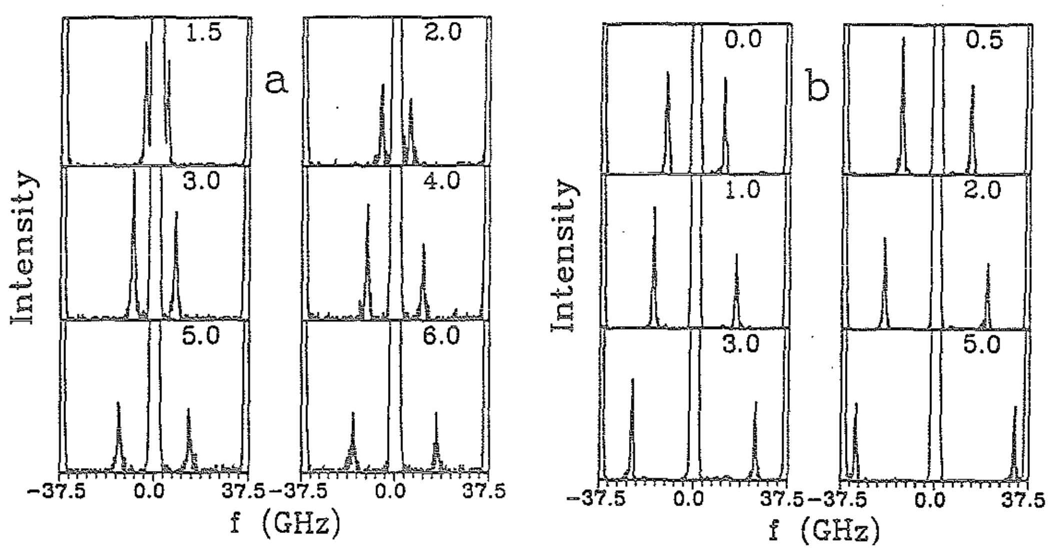

Fig. 4.3 Magnon Spectra in Various Magnetic Field as Indicated in the Upper Right Corner of Each Spectrum (unit: in 10^{-1} Tesla), for (a) 2ML and (b) 15ML Fe Films.

These variations of spinwave frequency f with film thickness d_{Fe} and applied field μ_0H can be described with a modified Damon-Eshbach theory for the surface magnetostatic waves[4.12-4.14]:

$$f = \frac{\gamma}{2\pi}\left\{(\mu_0H + B_a)(\mu_0H + B_a + \mu_0M_{eff}) + \left(\frac{\mu_0M_{eff}}{2}\right)^2\left[1 - \exp(2k_y d_{Fe})\right]\right\}^{\frac{1}{2}} \tag{4.1}$$

where $\gamma=g\mu_B/h$ is the gyromagnetic ratio, g the spectroscopic splitting factor, μ_B the Bohr magneton, h Plank's constant, $B_a=2K_1/M_S$ the magnetic anisotropy field, K_1 the crystal anisotropy constant, M_s the saturation magnetization, and M_{eff} the effective magnetization.

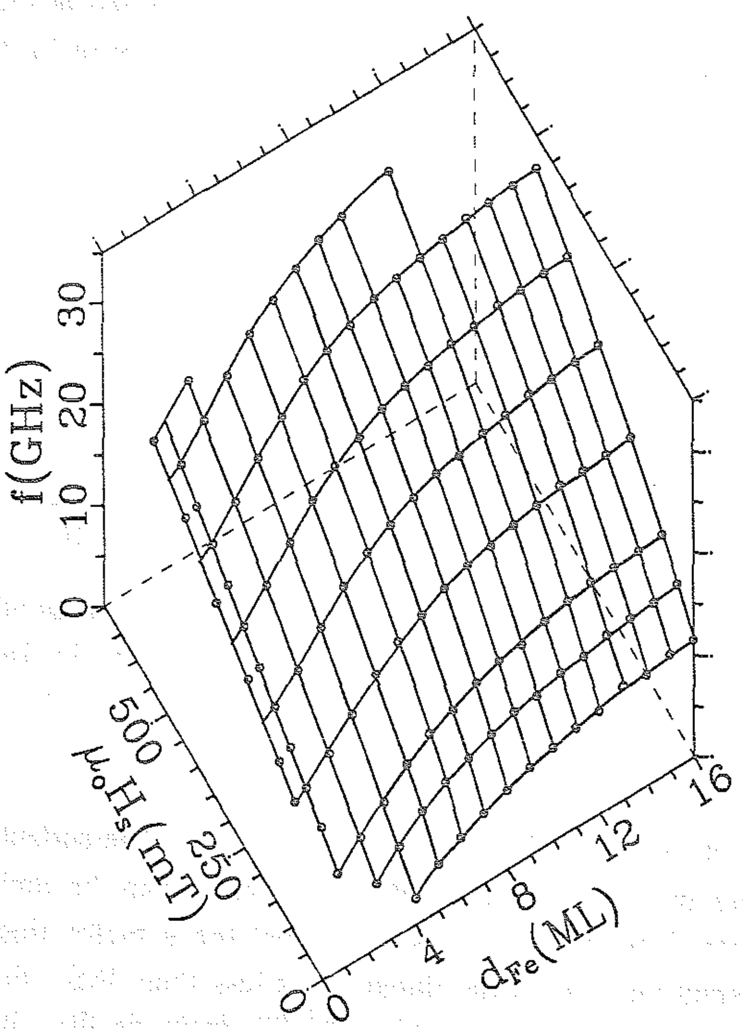

Fig.4.4 Spinwave Frequency versus Applied Magnetic Field and Fe Thickness for the Fe Wedge Samples evaporated at T_S=RT (293K). Circles are Experimental Results from BLS. The Curves in f~μ_0H Coordinates are predicted by the Damon-Eshbach Theory, and the Lines in f~d_{Fe} Coordinates are Guides to the Eye. The Applied Field is along an Easy Axis in the Film Plane. Measured Temperature is 293K.

$$\mu_0 M_{eff} = \mu_0 M_s - \frac{2k_s}{d_{Fe} M_s} \quad (4.2)$$

where k_s is surface anisotropy constant. By fitting the measured data of f versus $\mu_0 H$, the value of B_a, $\mu_0 M_{eff}$ and γ can be obtained at the same time. The fitted curves for the Fe films of 1.5 - 16ML are shown in fig.4.4. It should be pointed out that for the thicknesses larger than 3ML the fitting is unarbitrary,

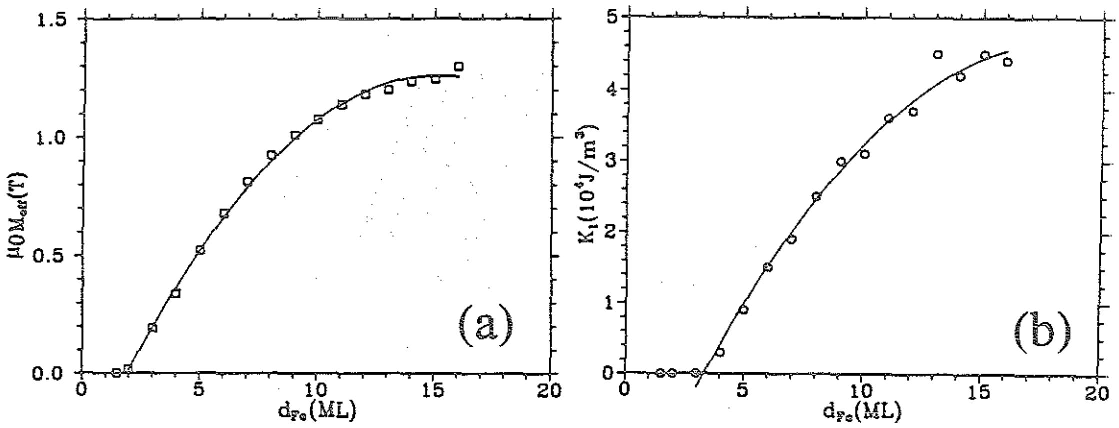

Fig.4.5 The thickness Dependences of (a) the effective Magnetization and (b) the In-plane Magnetic Crystal Anisotropy Evaluated In Terms of the Modified Damon-Eshbach Theory (equ.4.1). For Fitting an Aveage g=1.99 was Used. (evaluated by P.X.Zhang).

and the parameters, B_a, $\mu_0 M_{eff}$ and γ, obtained are independent of the choice of initial values in the fitting. However, some error may be introduced due to the experimental inaccuracy. It was found that the g factor fluctuates slightly around a constant value until the thickness is less than 3ML. For convenience of the data analysis, an average g value (≅1.99) from the first fitting was used. The Fe-thickness dependent effective magnetization $\mu_0 M_{eff}$ and magnetic anisotropy K_1 are indicated in fig.4.5(a) and (b), respectively.

From fig.4.4 it can be seen that the measured frequency shifts for 1.5ML Fe are linearly proportional to the applied fields. According to equ. 4.1, it means that the magnetization and the anisotropy in the film have to be zero. This, in fact, is a paramagnetic phase. With the reduction of the film thickness, the exchange interaction becomes weaker and then the Curie point of the film is below RT. In contrast, the f-μ_0H dependence for the 2ML film shows nonlinear behaviour, i.e. a ferromagnetic phase. So far there is little knowledge on the paramagnetic phase of ultrathin magnetic films and the transition from ferro- to paramagnetic. This measurement may provide an opportunity for such a study.

Only the thickness dependence of the effective magnetization has been obtained from the fitting after introducing a surface parameter (see eq. 4.2). Hence individual parameters of M_s and k_s can not be obtained just from BLS. However, several reports[4.15-4.17] have shown an increase in the spinwave frequency with the reduction of the external field, which originates from a perpendicular surface magnetic anisotropy when a critical thickness of the film is reached. Clearly, in the results shown in fig.4.4, there is no detecteble perpendicular surface anisotropy at RT.

The established d_{Fe}-dependent anisotropy K_1 seems to follow a similar behaviour as the effective magnetization with a small offset in thickness. This is different from the properties of ultrathin Co (001) film on Cu (001)[4.3], where the two-dimensional magnetization is accompanied by a magnetic in-plane anisotropy. It can be seen, however, that the K_1 for Fe-films thicker than 12ML is near the value of bulk Fe.

In principle, angle dependent measurements of the spinwave frequency can directly yield the magnetic anisotropy. Before discussing the experimental results, it is necessary to describe the theoretical relation between the frequency and the angle φ (see fig.4.6). The coordinate system is given in fig.4.6. Concerning the FMR (ferromagnetic resonance) condition, the relation between angular frequency ω (=2πf) and effective induced magnetic field B_{eff} can be given as[4.18]

$$\bar{\omega} = -\gamma \bar{B}_{eff} \tag{4.3}$$

where γ is the gyromagnetic ratio, and the effective induced field is[4.18,4.19]

$$B_{eff} = \frac{1}{M_s \sin\theta}\left[\frac{\partial^2 F}{\partial\varphi^2}\bullet\frac{\partial^2 F}{\partial\theta^2} - \left(\frac{\partial^2 F}{\partial\varphi\partial\theta}\right)^2\right]^{\frac{1}{2}} \quad (4.4)$$

Here θ and φ are defined in fig.4.6, and F indicates the free energy density of the system. For the studied structure system as indicated in fig.4.6, F may be written as[4.20]:

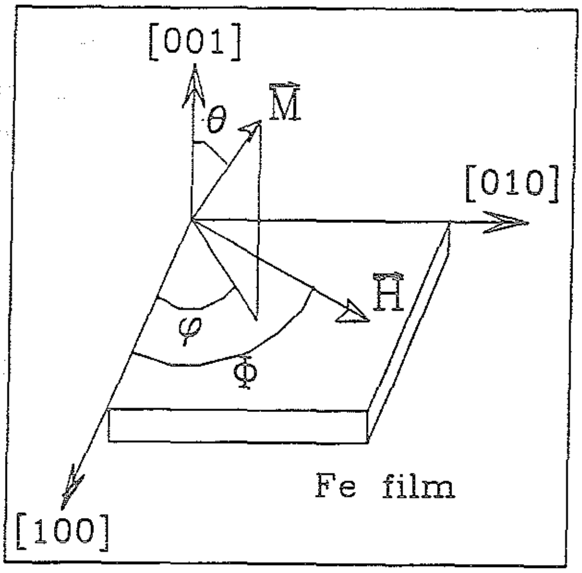

Fig.4.6 Orientations of the Magnetization and the External Magnetic Field in the Coordinate System of the [001] Oriented Crystalline Fe Film.

$$F = -\mu_0 M_s H \sin\theta\cos(\Phi - \varphi)$$

$$+ \frac{K_1}{4}(\sin^2 2\theta + \sin^4\theta\sin^2 2\varphi)$$

$$+ \frac{1}{2}\mu_0 M_s^2 \cos^2\theta - \frac{k_s}{d_{Fe}}\cos^2\theta \quad (4.5)$$

where the first term on the right hand is the Zeeman energy density, the second term is the magnetic anisotropy energy density, the fourth one comes from the shape anisotropy (demagnetization energy) of the system, and the last term is for the surface anisotropy. The minima of the free energy density, F, can be found by evaluation of equ.4.5 with $\frac{\partial F}{\partial \theta} = \frac{\partial F}{\partial \varphi} = 0$.

Then
$$\theta = \frac{\pi}{2} \tag{4.6}$$
and
$$\mu_0 M_s H \sin(\Phi - \varphi) = \frac{1}{2} K_1 \sin 4\varphi \tag{4.7}$$
are obtained. Equ.4.7 indicates that only if the external magnetic field is applied along one of the easy axes[100] (φ=0°) or along one of the hard axes[110] (φ =45°), the magnetization parallels to the external field. Considering the conditions of equ.4.6 and 4.7, the solution of equ.4.4 and 4.5 is the following:

$$f = \frac{\gamma}{2\pi}\left\{(B_a \cos 4\varphi + \mu_0 H)\left[\frac{B_a}{4}(3 + \cos 4\varphi) + \mu_0 H + \mu_0 M_{eff}\right]\right\}^{\frac{1}{2}} \tag{4.8}$$

Equ.4.8 expresses the magnon frequency as a function of the angle between the applied magnetic field and [100]-direction in the Fe (001)-plane. Because the studied ultrathin Fe films are thinner than 32Å which are << λ=5145Å, the laser wavelength in BLS experiment, equ.4.1 can be rewritten as:

$$f = \frac{\gamma}{2\pi}\left[(B_a + \mu_0 H)(B_a + \mu_0 H + \mu_0 M_{eff})\right]^{\frac{1}{2}} \tag{4.9}$$

This is the case of equ.4.8 when φ=0°. Thus, equ.4.1 and 4.8 are consistent with each other under the condition of d_{Fe} << λ=5145Å.

Let's come back to the experiment. Fig.4.7 shows the Φ-dependence of the magnon frequency for the Fe thin films with different thicknesses d_{Fe} in different applied fields $\mu_0 H$ as indicated in the figure. In fig.4.7(a) the 4-

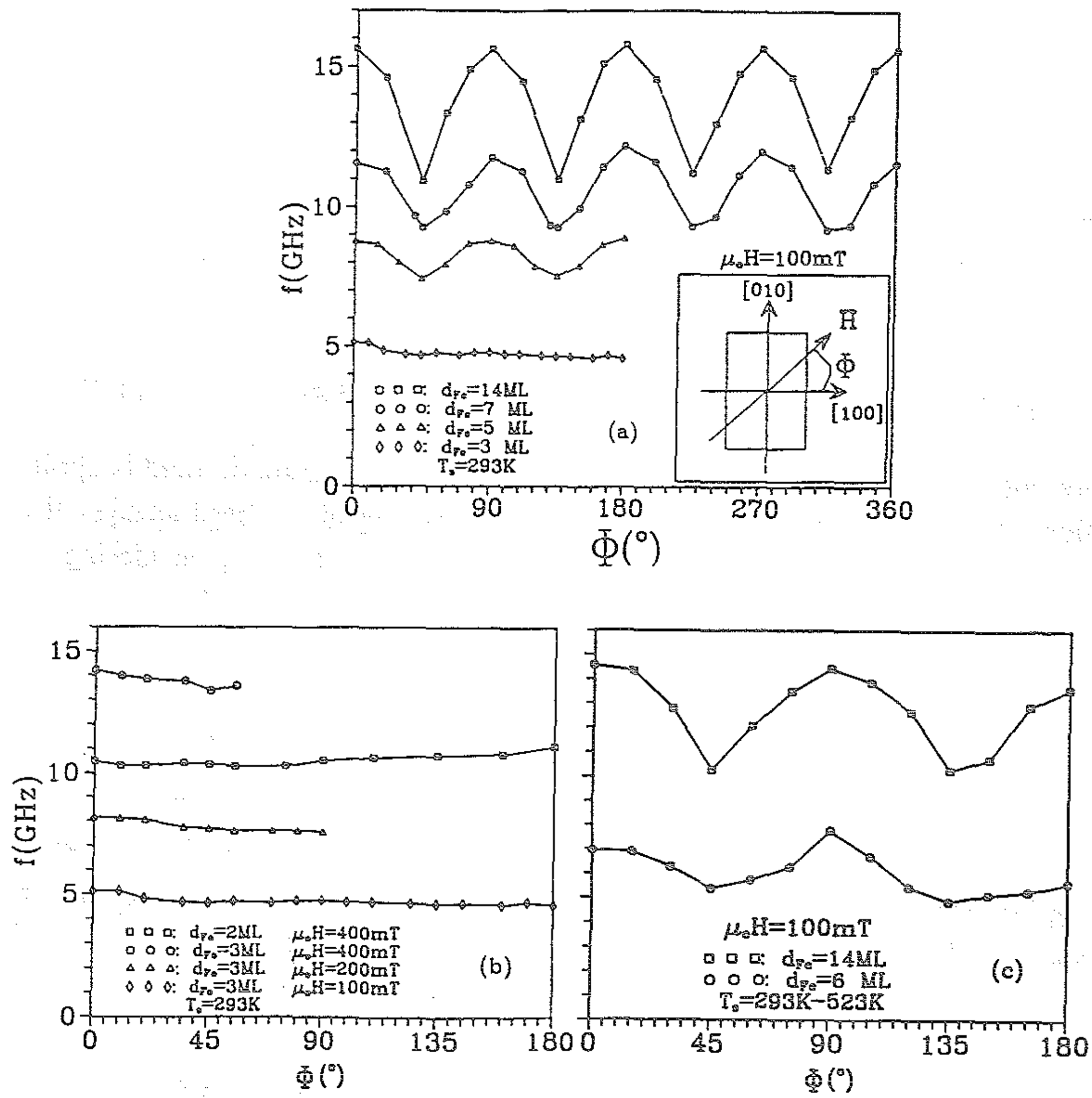

Fig.4.7 Spinwave Frequency as a Function of the Angle between the Applied Magnetic Field and the [100]-direction of the Fe Film Measured by BLS. The Measured Geometry is shown in the Lower-right Panel of fig.4.7a. (a) and (b) for the Sample of 0-32Å Wedge Prepared at RT and (c) for te Sample of 0-27Å Wedge prepared at Ts=0-523K (see the text).

fold in-plane magnetic crystal anisotropy is clearly seen for the 5, 7 and 14 ML Fe films evaporated at T_S=RT. The frequencies for the Fe thiner than 4ML, however, are almost independent of the directions of the magnetic field (fig.4.7b). This means that there is no anisotropy in these fillms. It can also be seen with the help of equ.4.8. If the magnon frequency f keeps constant as the field direction Φ varies, the magnetic anisotropy field B_a and K_1 must be zero.

Another sample evaporated at an elevated substrate temperature (T_s from RT to 523K during the fabrication of the Fe wedge) shows quite different results in BLS. For somewhat thicker Fe films, for example d_{Fe}=5-6Å, it was already difficult to record the frequency shifts. Fig.4.7c shows the field direction dependence of the spinwave frequency for d_{Fe}=6 and 14 ML. This can be compared with the results in fig.4.7a. It seems that the sample fabricated at the elevated temperature is not so good as that one prepared at RT. The reason may be due to interdiffusion at the Fe/Ag-interfaces. They could be alloyed and show weak ferromagnetism. However, the coercivity measured by MOKE for the two samples demonstrates almost the same behaviour (see fig.4.2).

Another interesting feature which should be mentioned is the ratio of Stokes and anti-Stokes intensities of the magnon peaks. In the case of Fe on an Ag buffer this ratio is only 1:1.3, while on substrates of sapphire[4.21] and W[4.16] it is about 1:3.4. Generally, at RT due to the low spinwave frequency, the intensities of both Stokes and anti-Stokes lines should be same. In YIG the difference of the magnon peak intensities was considered to be the contribution from the second order magneto-optical coupling constant[4.22]. It is not clear, however, if this difference in the ratio of Stokes and anti-Stokes lines for ultrathin Fe between different substrate and coating layer is due to the second order magneto-optical coupling or same other reasons. A possibility may originate from the reflected light field from the substrate, which is silver in our case.

4.4 Conclusion

The magnetic properties, such as in plane anisotropy, effective magnetization and coercivity etc, as well as their thickness dependences and external field direction dependences have been investigated by means of BLS and MOKE for ultrathin iron films prepared at two different substrate temperatures. These investigations provid basic data for the understanding of the magnetization, magnetic anisotropy, and the coercive force in ultrathin magnetic films.

The observed 4-fold anisotropy in ultrathin Fe, the observed narrow linewidth in BLS from 2 and 3 ML Fe films, and the small coercive forces (≤0.4mT) demonstrate that the studied iron films are of high quality. The possible interdiffusion between interfaces of the iron film and the buffer or coating layer has been found in the film prepared at an elevated temperature.

The continuous variation of the film thickness in a wedge geometry shows certain advantages for the investigation.

4.5 References

[4.1] P.Grünberg, In Light Scattering in Solids, Vol.66, Topics in Applied Physics, edt. by M.Cardona, G.Güntherodt, Springer, Berlin, Heidelberg, 1989, P.304.
[4.2] S.D.Bader and C.Liu, J.Vac. Sci. Technol. A9(3), (1991) 1924; L.M.Falicov, J.Mater. Res. 5 (1990) 1299.
[4.3] P.Krams, F.Lanks, R.L.Stamps, B.Hillebrands, and G.Güntherodt, Phys. Rev. Lett. 69 (1992) 3674.
[4.4] Pascal Xhonneux, and Eric Curtens, Phys. Rev. B46 (1992) 556.
[4.5] P.Etienne, J.Massies, F.Nguyen van Dau, A.Barthelemy and A.Fert, Appl. Phys. Lett. 55 (1989) 223.
[4.6] J.A.Wolf, Dissertation, University of Cologne (1993); and Jül-2743, KFA Research Center, Jülich, Germany.
[4.7] J.J.Krebs, J.Jonker and G.A.Prinz, J. Appl. Phys. 61 (1987) 2596.
[4.8] D.K.Lottis, J.Florczak, E.Pan Dahlberg, S.Batra, A.M.Wowchak, and P.I.Cohen, J. Appl. Phys. 63 (1988) 3662.
[4.9] M.Henzler, W.Göpel, Oberflächenphysik des Festkörpers, Teuber Strudienbücher (1991), Chapter 3.5-3.8.
[4.10] M.G.Lagally, D.E.Savage, M.C.Tringides, in Reflection Electron Imaging of Surfaces, NATO ASI Series, Series B, Physics Band 188, Plenum Press 1988, P.139.

[4.11 U.Hartmann, Phys. Stat. Sol. (a) 108 (1988) 387.
[4.12] R.W.Damon and J.R.Esgbach, J.Phys.Chem.Solids, 19 (1961) 308.
[4.13] B.Hillebrands, P.Baumgart, and G.Güntherodt, Appl. Phys. A49 (1989) 589.
[4.14] P.X.Zhang and W.Zinn, Phys. Rev. B35 (1987) 5219.
[4.15] J.G.Gay and R.Richter, Phys. Rev. Lett. 56 (1986) 2728.
[4.16] B.Hillebrands, P.Baumgart, and G.Güntherodt, Phys. Rev. B36 (1987) 2450.
[4.17] J.F.Cochran, B.Heinrich, A.S.Arrott, K.B.Urquhart, J.R.Dutcher and S.T.Purcell, J. Phys.C8 (49) (1988) 167.
[4.18] J.Smit and H.G.Beljers, Philips Research Repts 10 (1955) 113.
[4.19] J.W.Kauffman and J.S.Koehler, Phys. Rev. B97 (1955) 555.
[4.20] J.O.Artman, Phys. Rev. B105 (1957) 62.
[4.21] P.X.Zhang, Y.Z.Pang and W.Zinn, Solid State Commun. 60 (1986) 449.
[4.22] W.Wettling, M.G.Cottam, and J.R.Sandercock, J. Phys.C8 (1975) 211.

5 Interlayer Magnetic Coupling in Fe/Cr/Fe Layered Structures

With 37 Figures and 7 Tables

5.1 Introduction

Fe/Cr/Fe was the first system discovered to have antiferromagnetic(AFM) exchange coupling between the two Fe layers[5.1] and to show a giant magnetoresistance(GMR) effect[5.2,5.3]. In the last years many details about this exchange coupling have been reported. The most important are the long period[5.4] and short period[5.5-5.7] oscillations and the biquadratic coupling contribution which tends to align the two magnetizations in the magnetic films on both sides of the interlayer perpendicular to each other[5.8,5.9]. However, the interpretation of interlayer coupling in this oldest system, the Fe/Cr/Fe sandwich, is by far not complete. Satisfactory understanding of the microscopic mechanism of this coupling phenomenon calls for more detailed experiments. In this chapter, systematical investigations of magnetic exchange coupling between Fe (001) layers interspaced with Cr interlayers is presented, which includes growth research of the sandwich structures, thermal stability of the coupling, temperature dependence of interlayer coupling, origin of biquadratic coupling, role of the nesting effect on the interlayer coupling and influence of interface and structure quality on the exchange coupling.

5.2 Investigations of Growth

5.2.1 Preparation Recipe

For studying interlyer coupling, the fabrication of high quality specimens is greatly desired. The specimen geometry adopted in this work is shown in fig.5.1. It consists of a GaAs substrate, a Fe seed layer, Ag buffer layer, the Fe/X/Fe sandwich structure to be investigated and a ZnS protective and antireflective layer. The studied sandwich structure is normally prepared in a wedge geometry in this work. The recipe for producing this sample has been well studied and improved previously [5.10,5.11].

Fig.5.1 Sample Geometry evaporated in UHV by means of MBE. X=non-magnetic interlayer materials. The numbers indicate the thicknesses of the layers.

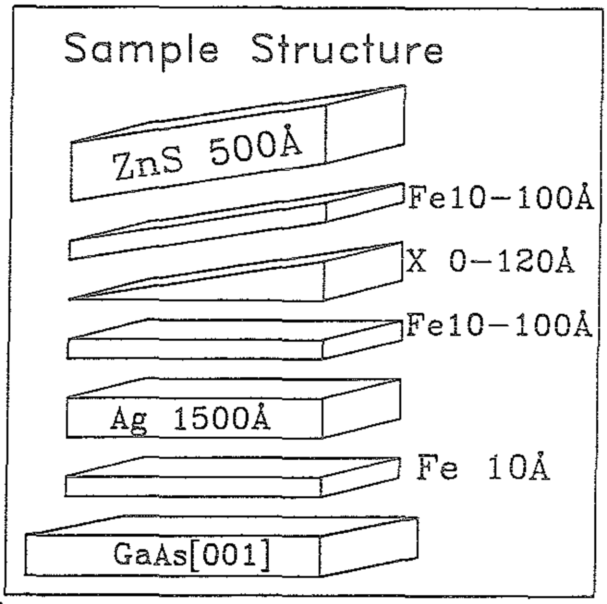

Preparation and treatment of the GaAs substrate, growing Fe seed layer and Ag buffer layer and their heat treatments have been described in the previous chapter (see section 4.2). The preparation conditions are also briefly summarized in tab. 5.1, where d is the thickness of the film, T_s the substrate temperature during evaporation, T_a the annealing temperature, V_r deposition rate of the film. X denotes the non-magnetic interlayer and t indicates the time for annealing.

The GaAs substrate is treated in such a way that its surface reaches "Auger cleanness" (sensitivity is 1/100ML). Surfaces of the samples are characterized by means of SPA-LEED. The growth of the films is monitored by means of RHEED (see section 4.2 and 5.7).

Tab. 5.1 The preparation recipe for the sandwich structure (see text).

Element	d (Å)	V_r (Å/sec)	T_s (K)	T_a (K)	t (mins)
GaAs(001)	4.5×10^6			823	60
Fe	10	0.1~0.2	373		
Ag	1500	1~1.5	373	573	60
Fe	10~100	0.1~0.2	293/523		
X	0-120	0.1~0.2	293/523		
Fe	10~100	0.1~0.2	293/523		
ZnS	500	1~2	293		

5.2.2 Influence of Substrate Temperature and Deposition Rate on Oscillatory Exchange Coupling

Much growth research of Fe/Cr/Fe sandwich structures on GaAs has been done by Wolf[5.10] in this laboratory. Here emphasis is only given on two conditions for the sample preparation. These are the substrate temperature T_s and the deposition rate of the film V_r.

Fig. 5.2 shows oscillatory interlayer coupling as a function of interlayer thickness in Fe/Cr/Fe structures prepared at nearly the same growth rate, but different substrate temperatures. For the samples prepared with $T_s \leq 423$ K only long period oscillations were found, while the samples deposited at higher temperatures developed short period oscillations as well as superimposed long periods. In spite of both fig.5.2(b) and (d) showing the fine oscillations, their oscillatory amplitudes are much smaller than that of the oscillations in fig.5.2(c). Thus, with V_r=0.1~0.2Å/sec and T_s=523K will be the optimal growth temperature for the Fe/Cr/Fe layered structures. Different growth rates have also a drastical effect on the oscillatory coupling. One can compare the results of fig.5.3(a) and (b) with each other. The sample, for which the coupling curve is shown in fig.5.3(b), was prepared at the optimal substrate temperature, but only long period oscillations have been found due to a too fast growth. Even samples grown at higher temperatures but with lower deposition rates, display well defined oscillations (fig.5.3c) in constrast to those grown at lower T_s but larger V_r (fig.5.3d).

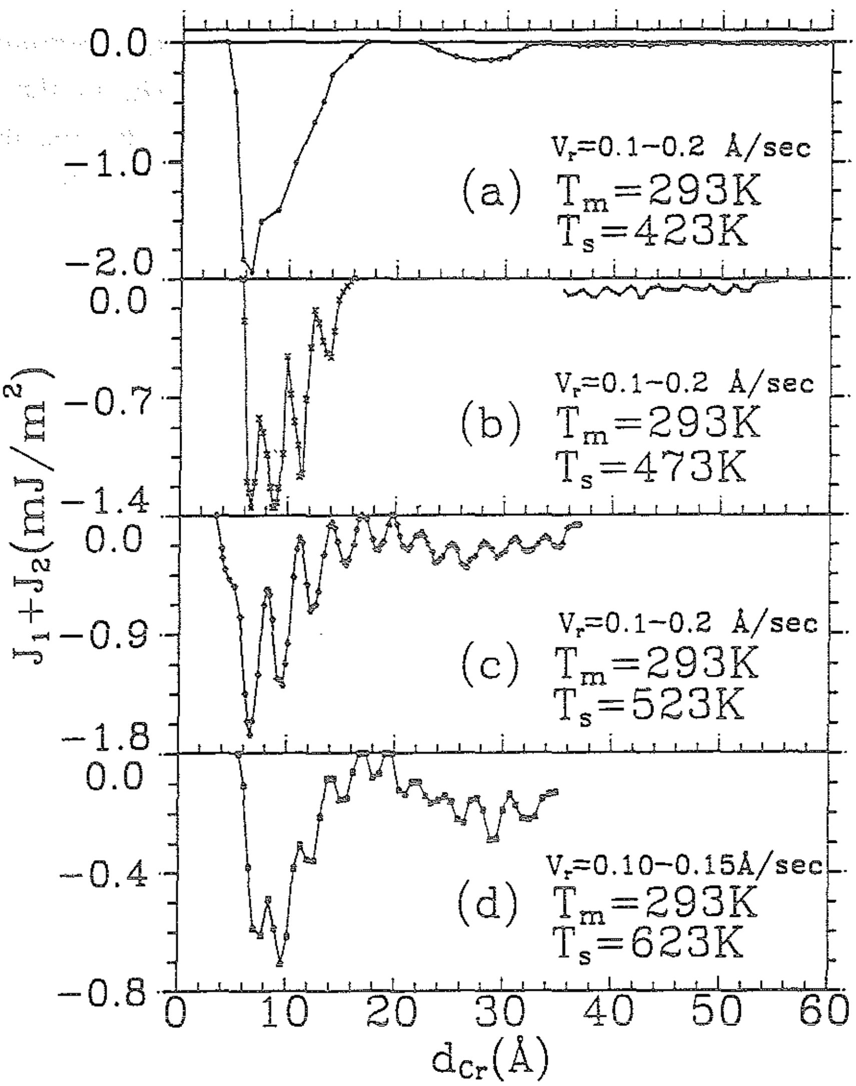

Fig.5.2 Interlayer exchange magnetic coupling as a function of the interlayer thickness in Fe/Cr/Fe (001) sandwiches grown epitaxially in UHV with the nearly same evaporation rate V_r but different substrate temperature T_s, measured by means of MOKE at temperature T_m.

In conclusion: It is clear that interlayer coupling is very sensitive to the preparation conditions. If the substrate temperature is too low, the sandwich structure will not have the quality to show the fine structure in the oscillations (fig.5.2a). If the T_s is too high, interdiffussion may take place at the Fe/Cr interfaces and attenuates the coupling strength, which is the case in fig.5.2(d). If evaporation is at a too high rate, the adatoms can not form a well ordered structure. Therefore, too fast growth can smooth the fine oscillations as shown in fig.5.3(b) and (d). Thus, to study the oscillatory coupling, the optimum may be reached with **T_s=523K** and **V_r=0.1~0.2Å/sec**. Fig.5.4 shows the domain configuration of the sample prepared with the optimal conditions, taken by means of Kerr microscope (KM). The stripe domains are clearly seen. The coupling oscillates with a short period of around 2ML Cr and superimposed by a long period of about 12ML Cr.

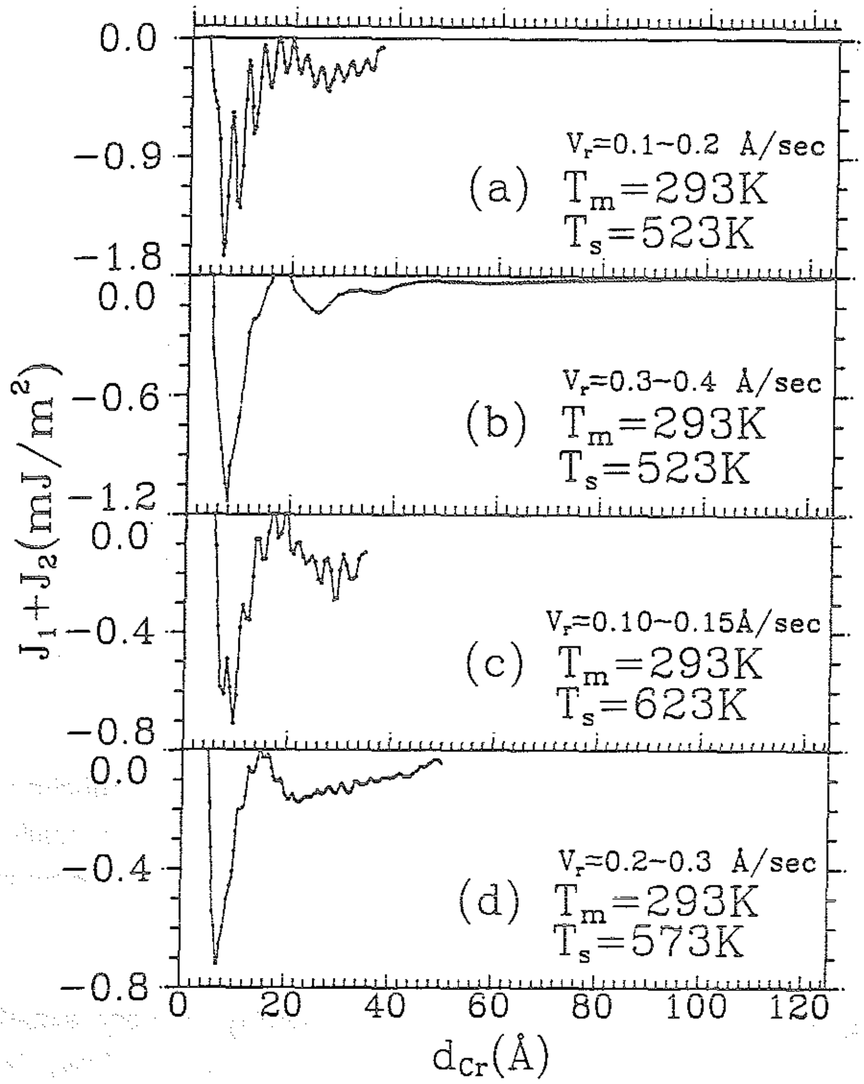

Fig.5.3 Interlayer exchange magnetic coupling as a function of the interlayer thickness in Fe/Cr/Fe (001) sandwiches grown epitaxially in UHV with evaporation rate V_r and substrate temperature T_s, measured by means of MOKE at temperature T_m.

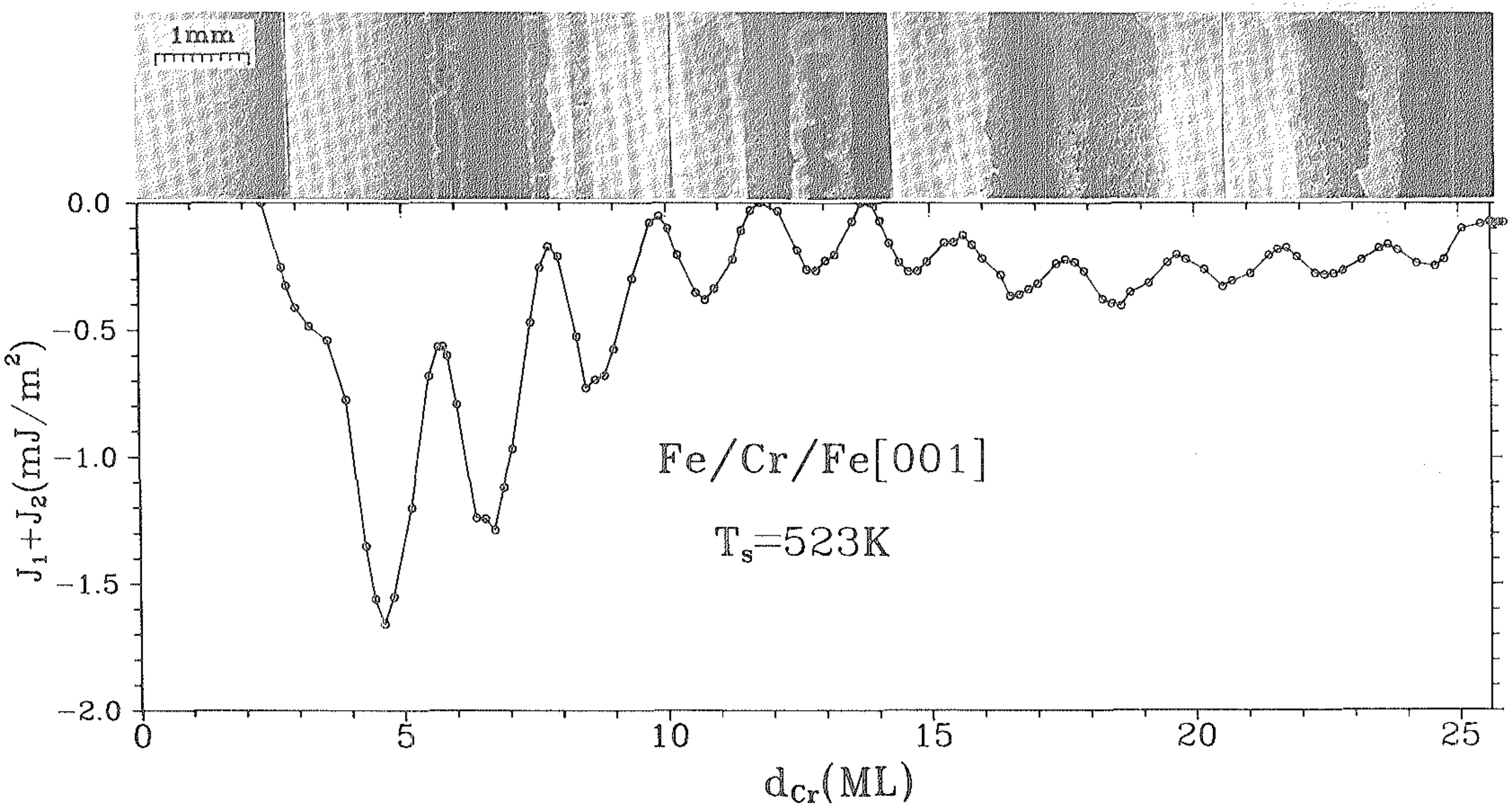

Fig. 5.4 Domain pattern and interlayer coupling vs. interlayer thickness in a Fe/Cr/Fe layered structure (fig.5.2c). The domain picture was taken by means of a Kerr microscope with an external magnetic field of 20mT along a [100] direction in the film plane.

5.3 Thermal Stability of the Interlayer Coupling

Magnetic exchange coupling between Fe layers across Cr interlayer has been observed by means of MOKE during annealing over the temperature range of 293 to 809K. The heat treatment was carried out in a special vacuum chamber which was described in section 2.3. Two samples were used for this study. They were prepared at different substrate temperatures, T_s= RT and 523K, and show long and short period oscillations in the coupling, respectively.

Fig.5.5 Interlayer thickness dependence of saturation magnetic fields in a Fe(80Å)/Cr(0-27Å)/Fe(80Å) structure prepared with T_S=RT and V_r=0.1Å/sec, measured by means of MOKE before, during and after annealing at the indicated temperature. (a) the first AFM coupling peak; (b) the second AFM coupling peak.

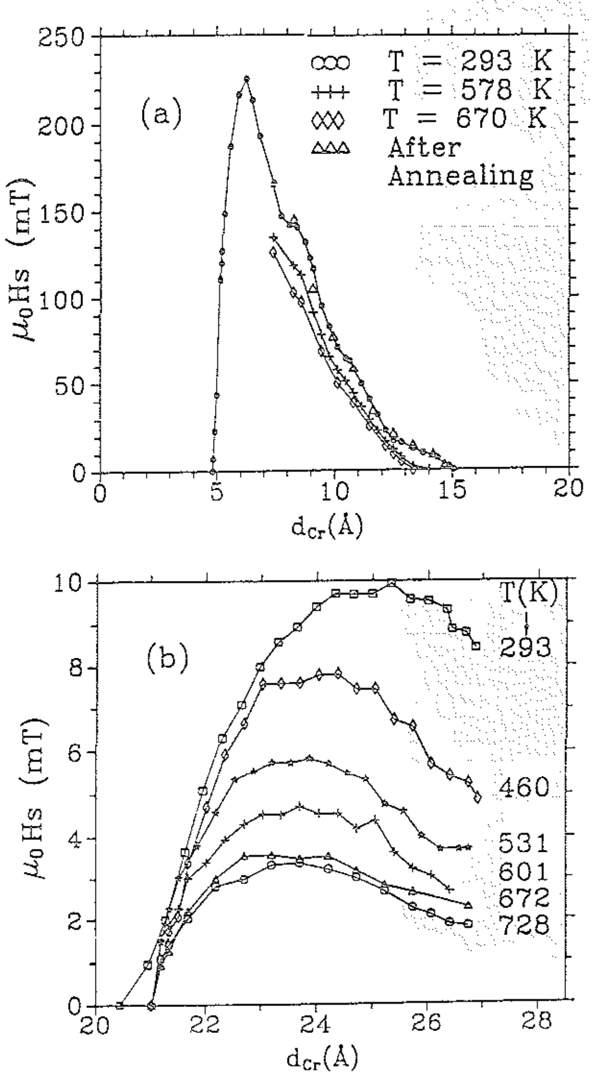

The results in fig.5.5 were obtained with the sample prepared at T_s= RT. Here the magnetic thickness dependent field $\mu_0 H_s$ from M(H) curves where the magnetizations in the adjacent Fe layers saturate parallel to the external field is presented. This sample shows only long range oscillation with a period of 12.6 ML. Fig.5.5(a) demonstrates the first antiferromagnetic coupling peak. The coupling fields $\mu_0 H_s$ were measured before annealing, during annealing and after annealing. The annealing temperature and time are indicated in the figure. It can be seen that the exchange coupling shows different temperature dependences for different interlayer thicknesses. For d_{Cr}=7.5Å the field decreases by 18.5% and 23.5% when temperature increases to 578 and 670K, respectively. In the range of d_{Cr}=14.5~15.0Å, the coupling vanishes at an elevated temperature, which is due to the contribution of biquadratic coupling. A similar phnomenon has been observed for Au and Al interlayers below room temperature[5.12]. An important feature in fig5.5(a) is that the coupling is thermally reversible after annealing up to 670K. Fig.5.5(b) presents the second antiferromagnetic coupling area in this sample, which was observed during annealing at various temperatures as indicated in the figure. For each temperature the annealing time is approximately 30 minutes. At RT 90° -type coupling is dominant in this range. In the range with d_{Cr}=22.5~25.3Å, the coupling is 180° -type (antialignment), and there is a significant contribution from the biquadratic interaction. As the temperature increases, the biquadratic coupling decreases strongly. Only bilinear coupling is observed for temperatures higher than 460K. Typical M(H) curves for d_{Cr}=26.2Å obtained by MOKE are given in fig.5.6(a) - (d). For this structure at RT (fig5.6b) and at about 339K (fig.5.6c) the coupling is 90°-type, but at 6.2K (fig.5.6a) and 809K (fig.5.6d) it is antiferromagnetic. The coupling strength is given on top of each hysteresis loop. More details of this temperature dependence will be discussed in the next section.

The behavior of fine oscillations in the exchange coupling after annealing at various temperature is shown in fig.5.7. This sample was prepared under the optimal conditions and shows two period oscillations, whose long- and short periods are around 12.6 and 2 ML in Cr thickness, respectively. The coupling after heat treatment for several hours agrees well with that before heat treatment

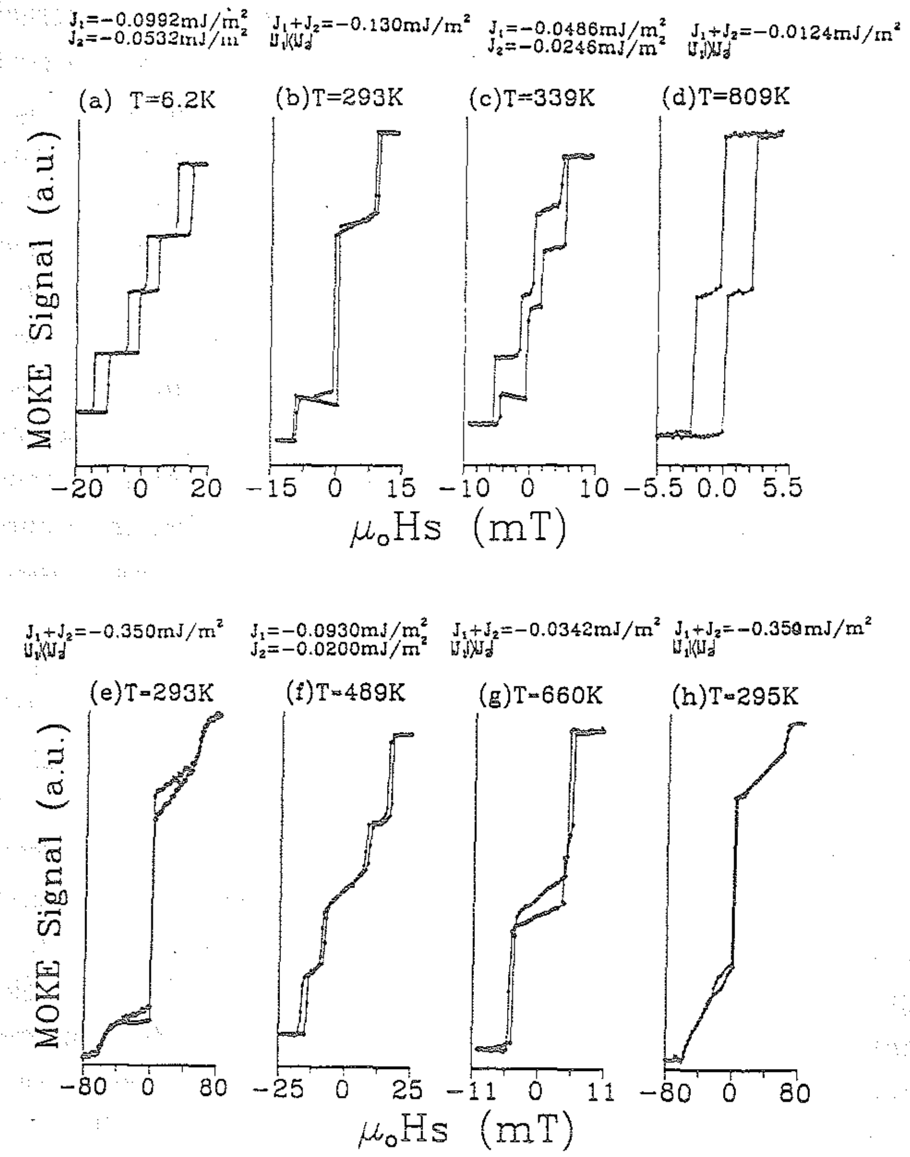

Fig.5.6 Magnetic hysteresis loops measured at various temperatures by means of MOKE on the wedge samples. (a)-(d) were obtained from Fe(80Å)/Cr(0-27Å)/Fe(80Å) prepared at RT at the point with d_{Cr}=26.2Å, where fig.5.6(b)-(d) were obtained after annealing for 10, 20 and 30 minutes, respectively. Fig.5.6(e)-(h) is for Fe(50Å)/Cr(0-36Å)/Fe(50Å) prepared at 523K at the point with d_{Cr}=26.6Å. Magnetic field was applied along the in-plane easy axis of the films.

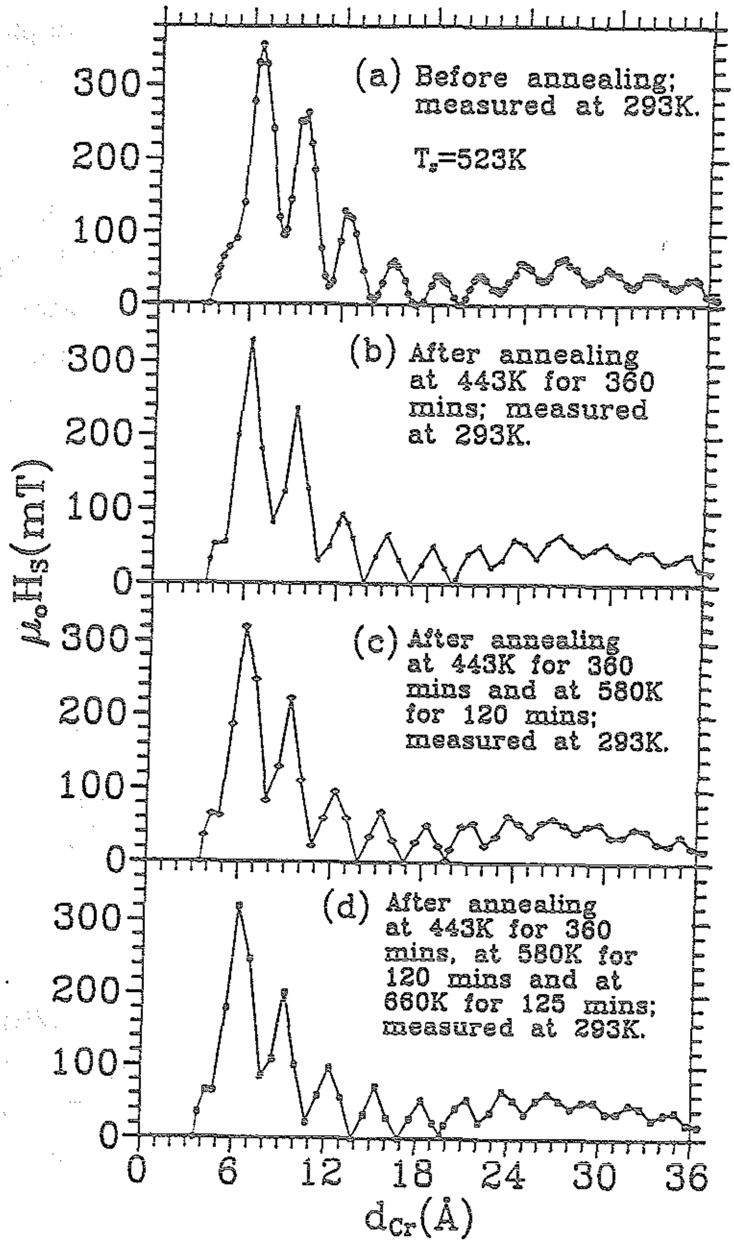

Fig.5.7 Interlayer thickness dependence of saturated magnetic fields in Fe(50Å)/Cr(0-36Å)/Fe(50Å) structure evaporated with T_S=523K and V_r=0.1~0.2Å/sec, measured at RT after annealing with the indicated temperature and time. This sample is the same as that in fig.5.2(a).

except in the range of extremely thin interlayers and strong coupling. Typical hysteresis curves at the d_{Cr}=26.6Å point during the annealing procedure are shown in fig.5.6(e) - (f). Fig.5.6(e) and (f) indicate that the coupling could be reproduced for this sample after annealing up to 660K . The coupling type will change too at high temperatures. As the temperature reaches 660K (fig.5.6g) the biquadratic coupling is close to zero ($J_2 \cong 0$).

Several authors have investigated the temperature dependence of antiferromagnetic coupling in the Fe/Cr/Fe systems [5.13-5.15] and given similar results. Namely the exchange coupling strength decreases linearly with temperature. The temperature dependence of the coupling extrapolates to zero at about 700K. However, in this work the antiferromagnetic coupling has been observed up to 800K (fig.5.6d). The problem is that the coupling will not be

Tab.5.2 Coercive forces measured by means of MOKE at temperaute T_m. T_a is annealing temperature, t is annealing time and d_{Cr} is the interlayer thickness in Fe/Cr/Fe sample prepared with T_s=293K and V_r=0.1Å.

d_{Cr} (Å)	7.5		26.2		
t (mins)	20	25	30	60	65
T_a (K)	758	758	809	809	809
T_m (K)	758	293	809	809	293
$\mu_0 H_c$ (mT)	2.6	10.0	1.4	2.1	5.0

stable at temperatures above 758K. Beyond this temperature diffusion between Fe and Cr could be observable by measuring the behavor of coercive forces. Tab.5.2 displays the coercive forces in the first sample at different temperatures for various times after the coupling disappeared. The coercive force at d_{Cr}=7.5Å increased faster than that at d_{Cr}=26.2Å. The reason is that the interface quality is more sensitive to thinner interlayer thicknesses due to interdiffusion at high temperatures.

In conclusion: The interlayer magnetic exchange coupling for both long and short period oscillations in Fe/Cr/Fe systems has been observed in situ by MOKE during annealing up to around 800K. It has been found that the oscillatory coupling for both cases is thermally stable up to 700K and can be observed until the sample structure is destroyed at temperatures beyond approximately 750K. A deviation in the range of extremely thin interlayers is contributed to the diffusion at the Fe/Cr interfaces . The biquadratic coupling is reduced faster than the bilinear one with increasing temperature.

5.4 Temperature Dependence of the Interlayer Coupling

5.4.1 Long Period Oscillation

Fig.5.8 shows the thickness dependence of the coupling at 6.2, 293 and 321K in Fe/Cr/Fe structures prepared with T_s=293K and V_r=0.1~0.2Å/sec. The coupling oscillates as a function of the interlayer thickness with a period of 12.6ML. In order to clearly see the coupling types with a certain interlayer thickness at a certain temperature, one can refer to fig.5.9 which displays a "phase" diagram of the interlayer coupling for this system. In fig.5.9, schematic hystereses are used to indicate the coupling types which are explained in tab.5.3.

As discussed in chapter 3, there are three different types of coupling which are known. For antiferromagnetic coupling we distinguish between three different cases according to different ratios of coupling strength ($\mu_0 H_s$) and anisotropy field $B_a=2K_1/M_s$ where K_1 is the anisotropy constant and M_s the saturation magnetization of the Fe layers. According to the theoretical analysis in chapter 3, only J_1+J_2 can be obtained for type (1) and (2). Separated parameters, J_1 and J_2, can be obtained for type (3), (4) and some special cases of type (5). All data are shown in fig.5.8. In the first AFM coupling peak, the bilinear coupling (J_1) is dominant, but between the areas of AFM and FM coupling there are 90° -type coupling zones where the contribution of biquadratic coupling (J_2) is larger. This was first observed by a Kerr microscopy[5.8]. As shown in fig.5.9, region (a) and (f) are FM type coupling, (c) and (d) are AFM coupling and (b) and (e) which are between (a) and (c) and between (d) and (f), respectively, are 90° -tpye coupling. For the second AFM peak, around d_{Cr}≅24Å the situation is more complicated. In fig.5.9, zone (i) and (j) are AFM coupling, (g) and (h) are 90° -tpye coupling. Diffusion in region (k) has been observed as mentioned in section 5.3, where the coupling is not stable.

Tab.5.3 Schematic diagram of hysteresis curves for different coupling types.

Schematic Hystereses	**Type of interlayer Coupling (J_1: bilinear coupling; J_2: biquadratic Coupling)**
(1) 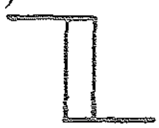	Ferromagnetic coupling ($J_1>0$; $J_2\geq0$)
(2) 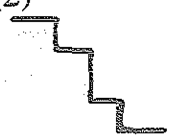	90° -type coupling ($J_2<0$; $J_2\leq J_1$)
(3) 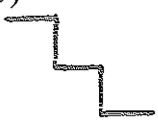	Antiferromagnetic coupling ($\mu_0 H_s \leq B_a = 2K_1/M_s$) ($J_1<0$; $J_2\cong0$)
(4) 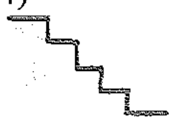	Antiferromagnetic coupling ($\mu_0 H_s \sim B_a = 2K_1/M_s$) ($J_1<0$; $J_1\leq J_2$)
(5) 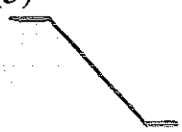	Antiferromagnetic coupling ($\mu_0 H_s \gg B_a = 2K_1/M_s$) ($J_1<0$; $J_1\leq J_2$)

The temperature dependences of interlayer coupling with fixed interlayer thicknesses are demonstrated in detail in fig 5.10. Fig.5.10(a) shows the results of d_{Cr}=5.0, 5.2 and 10.7Å. Coupling at the positions of d_{Cr}=5.0 and 5.2Å has larger biquadratic coupling, while the coupling at the position of d_{Cr}=10.7Å is dominated by bilinear one. It is obvious that the former decreases faster than

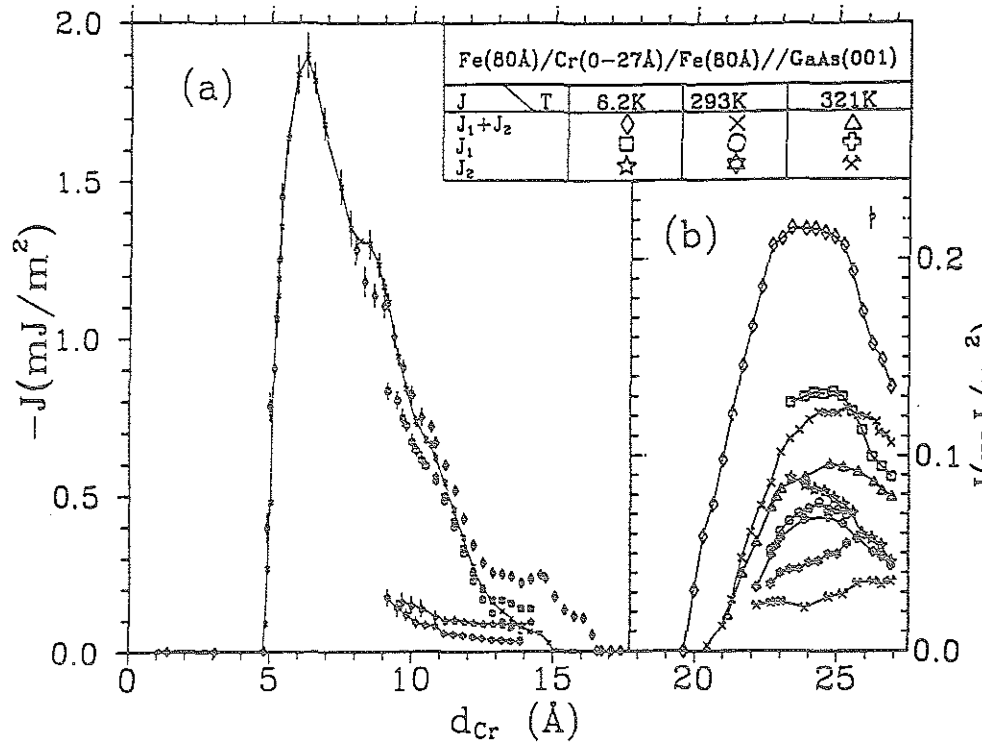

Fig.5.8 Interlayer coupling versus interlayer thickness, d_{Cr}, in Fe/Cr/Fe layered structure, measured at 6.2, 293 and 321 K. For some thicknesses of Cr interlayer the separated parameters, J_1 and J_2 are given.

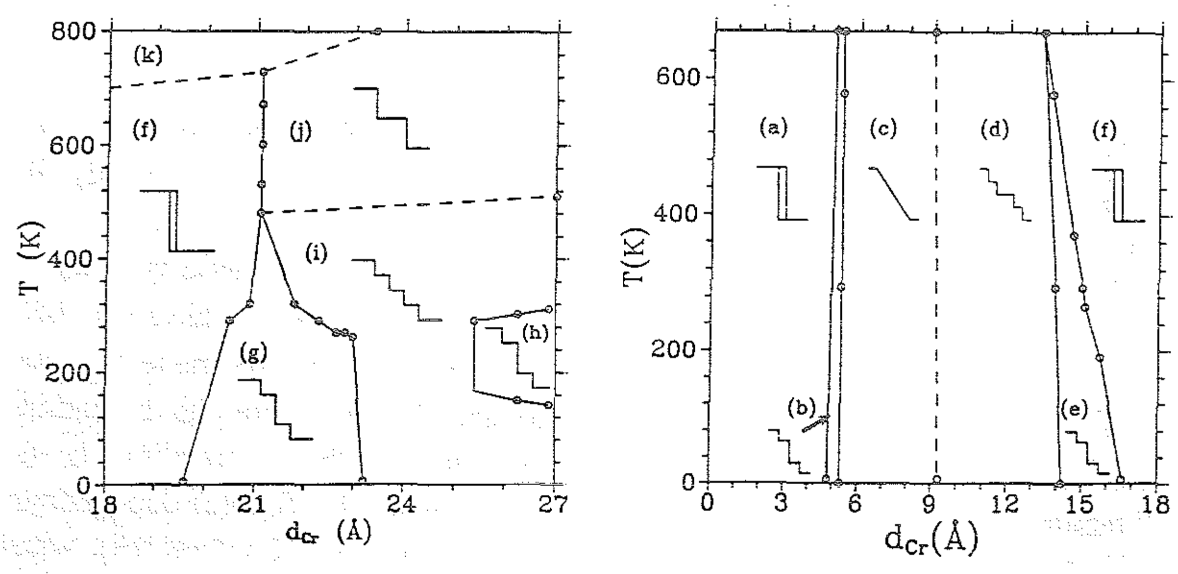

Fig.5.9 Phase diagram of the interlayer magnetic coupling in a Fe(80Å)/Cr(0-27Å)/Fe(80Å) layered structure. Schematic symbols are used to indicate different types of the exchange coupling. Their interpretation is given in tab.5.3.

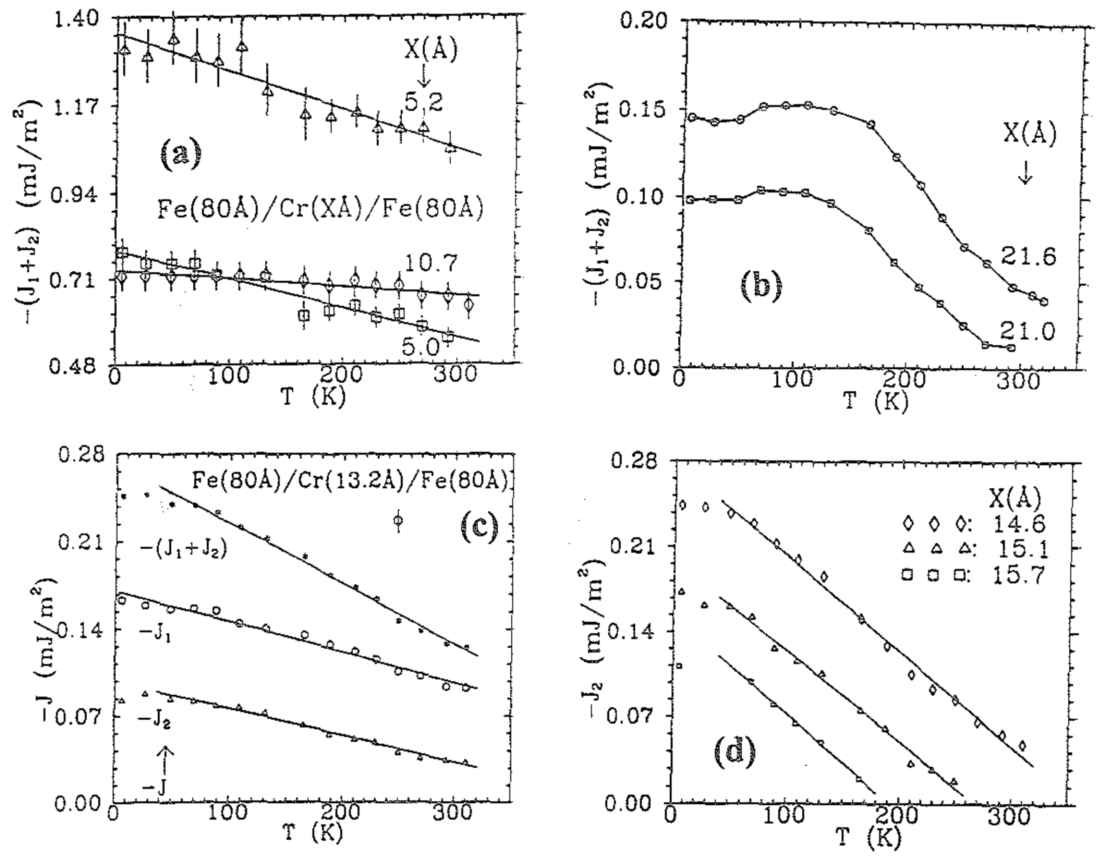

Fig.5.10 Temperature dependence of interlayer magnetic coupling in Fe(80Å)/Cr(0-27Å)/Fe(80Å) layered structure. Here X indicates the thickness of the Cr interlayer.

the latter as the temperature rises. Fig.5.10(d) displays the results in the transition region. J_2 has a finite value at low temperatures, but then the coupling is drastically reduced as the temperature increases. The coupling is almost biquadratic ($J_1 \cong 0$) in this region and is of ferromagnetic type as the temperature is near RT (room temperature). These phenomena have also been observed in the Fe/Au/Fe system[5.12,5.16]. Fig.5.10(b) shows the temperature dependence of the coupling at d_{Cr}=21.0 and 21.6Å where the biquadratic coupling is dominant. The behavior of the interlayer coupling is not monotonical with temperature. It shows a maximum. Fig.5.10(c) demonstrates exchange coupling versus temperature in Fe(80Å)/Cr(13.2Å)/Fe(80Å), which is of AFM type superimposed by a 90° -type contribution. The individual parameters, J_1 and J_2, can be evaluated from the MOKE measurement in this case. The bilinear coupling displays a linear temperature dependence and the biquadratic coupling shows a similar behaviour.

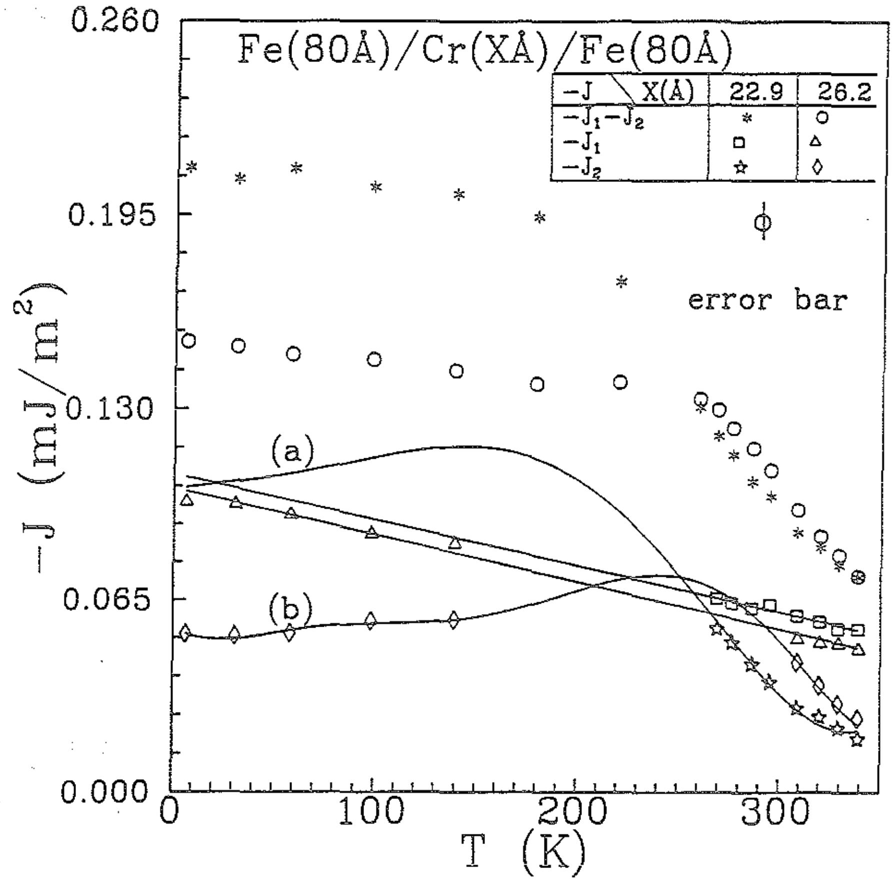

Fig.5.11 Interlayer coupling as a function of temperature in Fe(80Å)/Cr(22.9Å)/Fe(80Å) and Fe(80Å)/Cr(26.2Å)/Fe(80Å) sandwiches.

The region of d_{Cr}=25.5 - 27Å (see fig.5.9) shows a special temperature dependence of the coupling. The coupling type changes from AFM to 90° -type and comes back to AFM again as the temperature increases. Hysteresis curves at the position with d_{Cr}=26.2Å have been displayed in fig.5.6(a) - (d). The temperature dependence of the coupling with d_{Cr}=26.2Å as well as d_{Cr}=22.9Å is shown in fig.5.11. For d_{Cr}=26.2Å the strength of bilinear and biquadratic coupling can be separated from 6 to 150K and from 300 to 340K, and within the temperature range of 150 to 300K only the sum of these two contributions can be obtained. It can be clearly seen that the bilinear coupling shows a good linear temperature dependence, despite the lack of data from 150 to 300K. Then, the biquadratic coupling as a function of temperature can be deduced as shown by curve (b) in fig.5.11, which is not linear and shows a maximum value at about 250K. For d_{Cr}=22.9Å, only in the region between 260 and 340K a separation of J_1 and J_2 can be achieved. Given that the bilinear coupling in this interlayer thickness has a linear relation with temperature as observed in many other cases and reported in literatures[5.13-5.15], the temperature dependence of the biquadratic coupling (curve (a) in fig.5.11) can be obtained. It shows also a maximum.

5.4.2 Short Period Oscillation

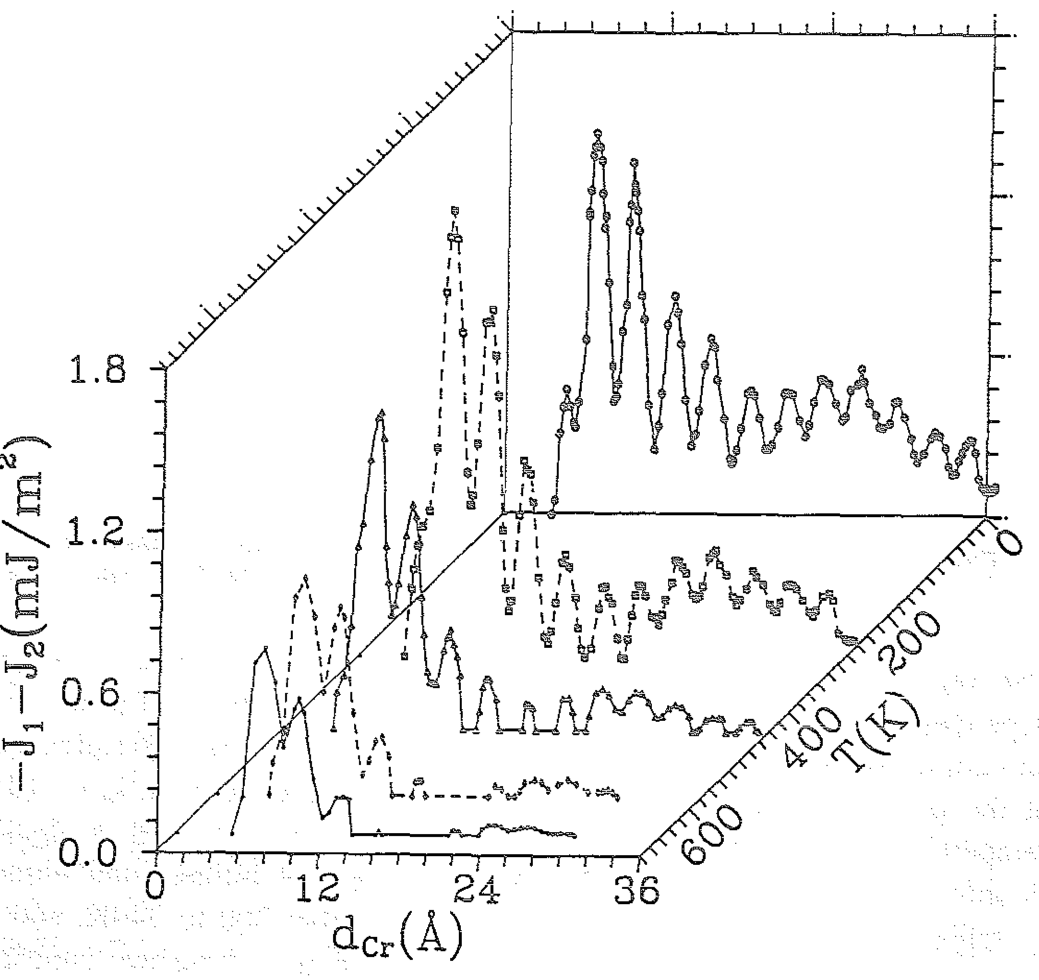

Fig.5.12 Interlayer coupling versus interlayer thickness in Fe(50Å)/Cr(0-36Å)/Fe(50Å) system, measured at temperature T by means of MOKE.

As mentioned above the oscillatory coupling is thermally reversible up to 700K. Fig.5.12 shows the coupling curves of the Fe(50Å)/Cr(0-36Å)/Fe(50Å) structure made at T_s=523K with V_r=0.1~0.2Å at various temperatures. The coupling oscillates with a short period of about 2ML and a long period of around 12.6ML. The "phase" diagram of the coupling for this system is shown in fig.5.13. From fig.5.12 and fig.5.13, it can be seen that the whole oscillatory coupling is located in a negative exchange background below room temperature(RT). Another feature below RT is that the 90°-type coupling is dominant in the oscillations. Only the first three peaks in the oscillations always show AFM coupling at tempratures from 6 to 700K. Between each two AFM peaks there is a 90°-type coupling area. As temperature increases to RT two FM coupling peaks appear at the positions of d_{Cr}≅17Å and d_{Cr}≅20Å. As temperature reaches about 360K there is another FM peak at d_{Cr}≅13.8Å. If temperature increases to higher than 570K, then the negative coupling in the range of d_{Cr}≅30 - 36Å and a negative coupling peak at d_{Cr}≅18Å disappear. The coupling in the region of d_{Cr}≅22.5 - 30Å changes from 90°-type to AFM type as temperature rises .

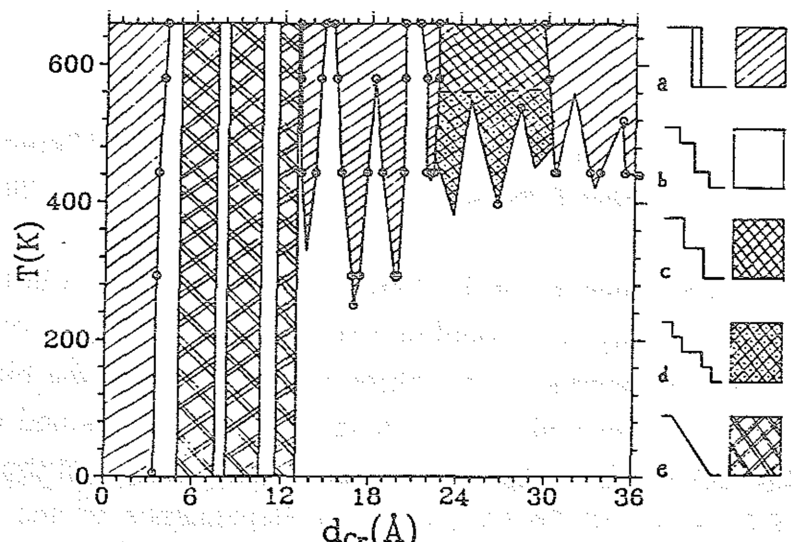

Fig.5.13 Phase diagram of interlayer coupling in the Fe(50Å)/Cr(0-36Å)/Fe(50Å) system. Schematic hystereses (a) - (e) are ultilized to show the coupling types. Their interpretation is given in tab.5.3.

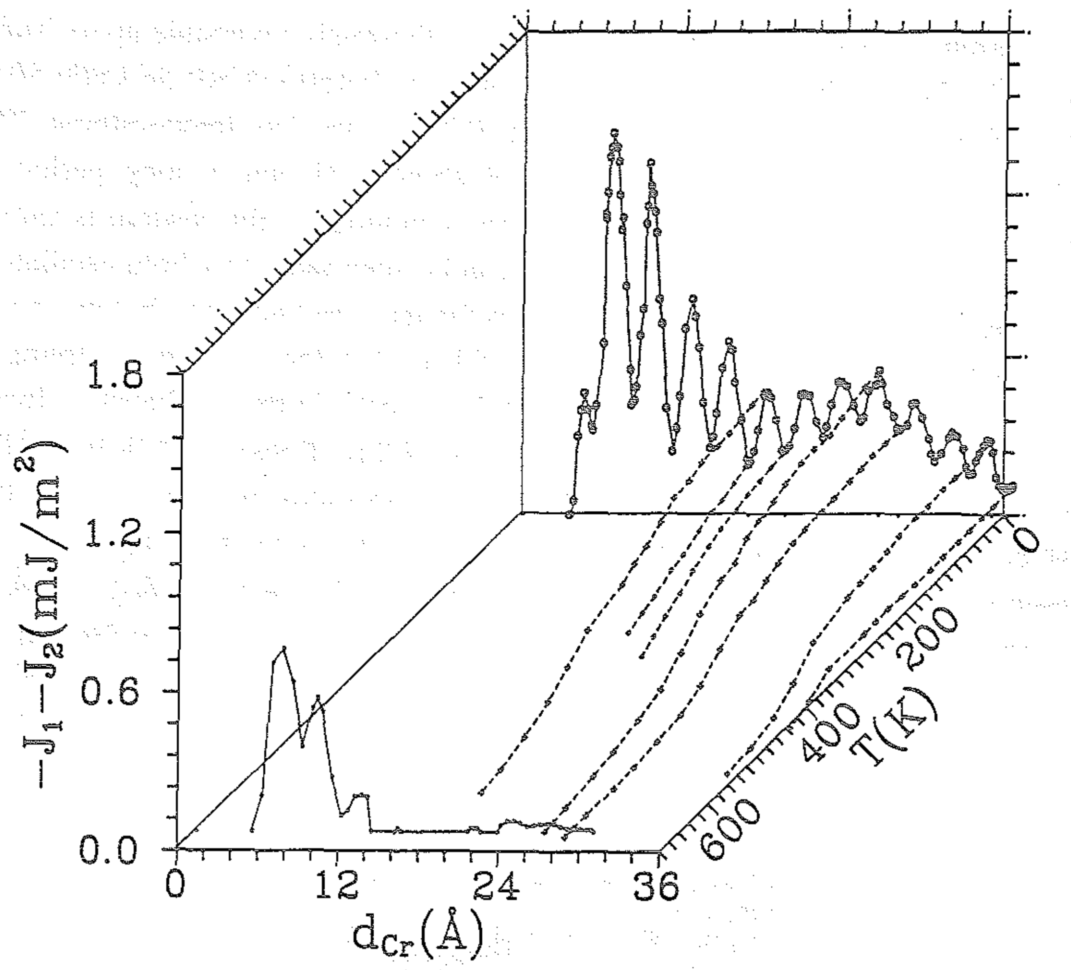

Fig.5.14 Temperature dependence of Interlayer coupling in different positions of the interlayer thickness in the sample of Fe(50Å)/Cr(0-36Å)/Fe(50Å).

The temperature dependences of the coupling curves are given in fig.5.14, in a three dimensional display. The coupling strength at the positions of $d_{Cr}\cong 17$ and 20Å, in which the biquadratic contribution is dominant and the bilinear one is near zero, decreases drastically as the temperature increases and decreases to zero around RT. A similar behavior has been also observed at the positions of d_{Cr}=15.4, 18.2, 35.1 and 36.3Å , etc. The dependence of the coupling on temperature at d_{Cr}=20.9, 26.6 and 28.1Å is different. There is a contribition of bilinear coupling as well as of biquadratic. The coupling damps also seriously as the temperature rises from 6K to 400K and then decreases slowly above 400K. In order to precisely analyze the temperature behavior of the coupling, the coupling at various temperatures at d_{Cr}=26.6 and 28.1Å is shown again with a separation of the J_1 and J_2 contributions in fig.5.15. The typical hysteresis curves at various temperatures for d_{Cr}=26.6Å have been presented in fig.5.6(e) - (f). At d_{Cr}=26.6Å bilinear- and biquadratic coupling can be separated at temperatures above 400K. Suppose that the bilinear coupling has a linear temperature dependence as discussed above, then the biquadratic coupling can be deduced from the total coupling strength as displayed in the fine dashed curve in fig.5.15. In this way, the biquadratic coupling versus temperature for d_{Cr}=28.1Å is obtained and shown in the coarse dashed curve in the figure. Athough the total coupling versus temperature for these two Cr- thicknesses is different, the biquadratic coupling vs. temperature behaves in the same way and decays rapidly. Extrapolating the linear temperature dependence of the bilinear coupling to zero, one can obtain the critical temperatures: about 750K for d_{Cr}=26.6 Å and 900K for d_{Cr}=28.1Å..

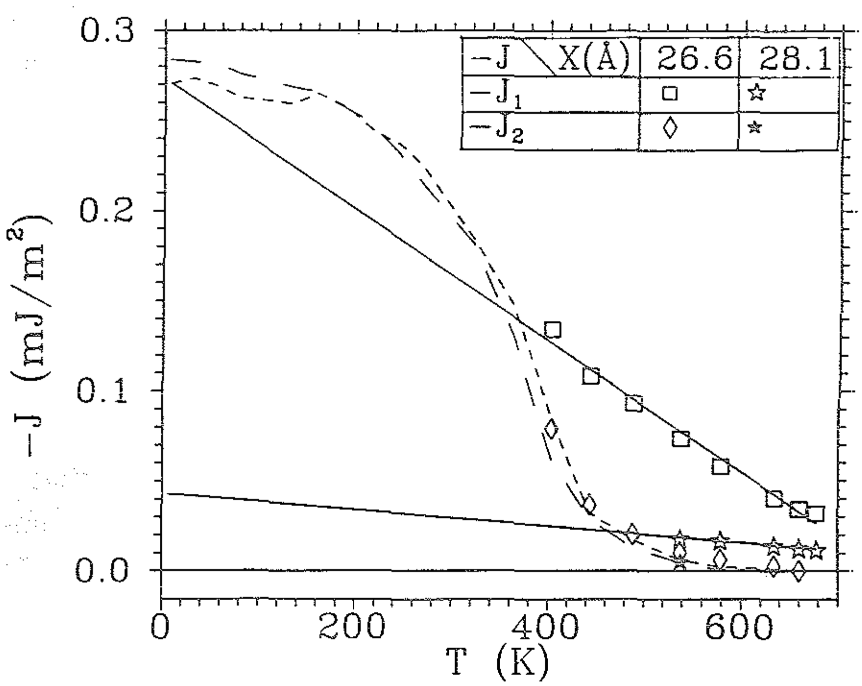

Fig.5.15 Temperature dependence of bilinear- and biquadratic coupling in the sample of Fe(50Å)/Cr(0-36Å)/Fe(50Å) with the interlayer thickness X.

In conclusion: Temperature dependences of both long and short period oscillatory coupling have been investigated from 6 to 700K. It has been found that the periods in the oscillations do not change in this temperature range. The bilinear coupling behaves in the way of linear temperature dependence. The biquadratic coupling behaves in very different ways. It is not always monotonically decreasing as temperature increases and can show maxima. A common feature of the biquadratic coupling, on the other hand, is a strong temperature dependence.

5.5 Nesting Effect

5.5.1 Introduction

In above the sections, the oscillatory magnetic exchange interaction between iron layers interspaced by a Cr layer has been investigated by means of MOKE on epitaxial wedge specimens. Concerning the coupling as a function of the interlayer thickness d_{Cr}, both short- and long period oscillations in combining bilinear and biquadratic exchange are found. In order to understand the oscillations, the nesting effect in the RKKY type interaction theory is employed. Finally, Fabry-Perot type model for the oscillatory coupling is discussed.

5.5.2 Experimental Results

The oscillation amplitudes in the interlayer magnetic coupling versus the interlayer thicknesses (d_{Cr}) in several Fe/Cr/Fe samples are summerized in fig.5.16. Considering the total coupling, the envelope curve of the exchange coupling may be written in the form

$$J_1 + J_2 = J_0\,(d_0/d_{Cr})^n \qquad (5.1)$$

where J_0 is the coupling strength as the interlayer thickness d_{Cr} equals to d_0 (=1.43Å), the thickness of one atomic layer of Cr.

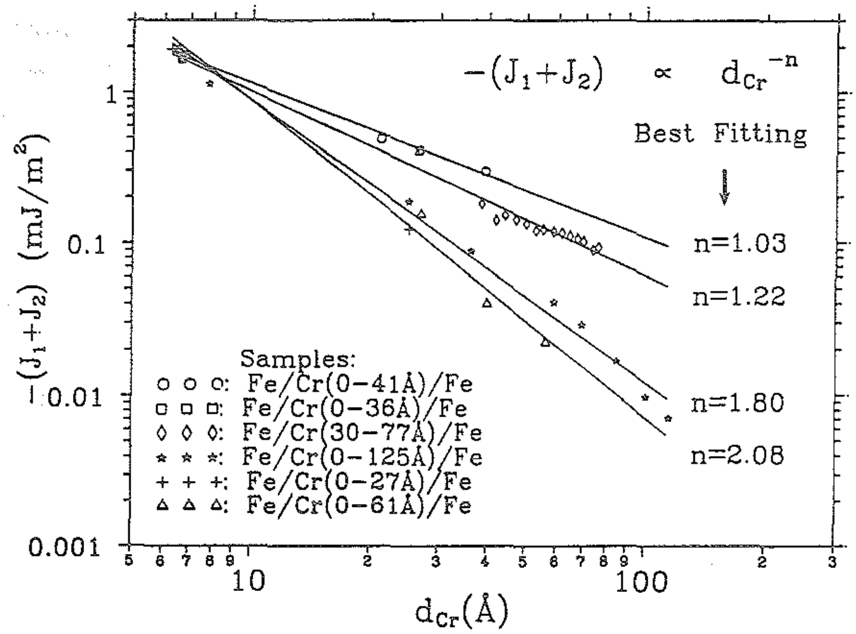

Fig.5.16 The interlayer thickness dependence of the amplitudes of the oscillations in the magnetic exchange coupling in Fe/Cr/Fe systems, measured at room temperature. Both horizontal and vertical coordinates are in logarithmic scales.

Equ.5.1 is used to fit the experimental data and the curves obtained from the best fitting are shown in fig.5.16 too. Fig.5.16 indicates that the attenuations of the oscillation amplitudes in the exchange coupling agree with the d_{Cr}^{-n}-dependent power laws, where n=1.03, 1.22, 1.80 and 2.08 for different samples. Some important parameters for these samples are quoted in tab.5.4. There are in total three different periods of the oscillatory coupling in Cr spacer systems to be observed in this work. Namely, the wavelengths λ=2.0, 10.0 and 12.6ML of the interlayer Cr have been obtained. From fig.5.16 and tab.5.4, it can be found that the attenuation of the coupling amplitudes with the interlayer thickness in fine oscillations is much faster than that in long period oscillations. These results can be compared with previous work on a 12.6ML-period oscillation of the coupling in the Fe/Cr/Fe layered structure in this laboratory[5.5]. In that work[5.5] for the first time the precise oscillatory exchange coupling in an epitaxial sandwich structure was reported and a damping power index n=4.5 was deduced from the experimental results, which is much larger than that observed in this work (see tab.5.4). Refering to the growth investigations in section 5.2, the damping power index in the oscillatory coupling might be also related to the quality of the layered structures, such as interface roughness, crystallinity of the interlayer, etc. Generally, the samples which result in smaller damping power indices should be of better quality. It would mean that the structure quality has been greatly improved since 1991 in this laboratory.

Tab.5.4 Sample list with important parameters. Here n is the power index obtained from fitting with equ.5.1, λ is the oscillation period, T_s is the substrate temperature and V_r is the evaporation rate during the sample preparation.

Samples: Fe/Cr/Fe	**n**	**λ (ML)**	**Preparation Condition**		**Ref. in This Thesis**
			T_s (K)	**V_r (Å/sec)**	
Fe/Cr(0-41Å)/Fe	1.03	2.0 12.6	523	0.1~0.2	
Fe/Cr(0-36Å)/Fe	1.03	2.0 12.6	523	0.1~0.2	Fig.5.2(c)
Fe/Cr(30-77Å)/Fe	1.22	2.0 12.6	523	~0.2	Fig.5.19
Fe/Cr(0-125Å)/Fe	1.80	10.0	523	0.3~0.4	Fig.5.3(b)
Fe/Cr(0-27Å)/Fe	2.08	12.6	293	0.1~0.2	Fig.5.8
Fe/Cr(0-61Å)/Fe	2.08	12.6	423	0.1~0.2	Fig.5.2(a)

5.5.3 Nesting Effect

Up to now there have been many theories to describe the magnetic exchange coupling between two ferromagnetic layers spaced by a nonmagnetic metal layer[5.17-5.31]. Among them, the RKKY type interaction theories have succeeded in explaining some characteristics of the oscillatory coupling[5.18-

5.21,5.25,5.26,5.31], especially, for noble metal spacer systems[5.18] (see also chapter 6).

The original RKKY interaction was introduced to deal with dilute magnetic alloy systems of localized magnetism[5.32-5.34]. The basic physics is that spins of magnetic atoms interact with conduction electrons of nonmagnetic atoms and polarize the conduction electrons, and then the spin polarization is propagated to other magnetic atoms and interacts with them. The RKKY interaction shows oscillatory behavior with the distance **d** between magnetic atoms and normally, the attenuation of this interaction is proportional to $\mathbf{d}^{-3}$. The oscillation period is related to the Fermi vector of the system. Roth et al[5.35] have indicated that the nesting in the Fermi surface of the system has a remarkable effect on the damping power in the oscillations (see tab.5.5).

Bruno and Chappert[5.18,5.19] have successfully applied the RKKY interaction to the layered magnetic systems. According to their theory, the oscillatory periods are connected with certain distances at the Fermi-surfaces of the interlayer materials. The attenuation of the oscillations can be also largely influenced by nesting in the Fermi surface of the interlayer materials.

The so-called nesting is a special feature which can appear in a Fermi surface. If two parts of a Fermi surface connected by a stationary vector Q closely fit each other under operating a translation, this case will be considered as complete nesting. If the two parts of the Fermi surface contact each other only along a line under the operation, this case is considered as partial nesting. And if the two parts of the Fermi surface have only a common point after operating the translation, this case is absence of nesting. The corresponding stationary vector Q is refered to as nesting wave vector. According to the theory[5.19], nesting in the Fermi surface can change the damping power index in equ.5.1. The interlayer coupling decreases as d_i^{-1}, $d_i^{-1.5}$ and d_i^{-2} for complete nesting, partial nesting and absence of nesting, respectively, where d_i is the interlayer thickness. Thus, due to the nesting effect the exchange coupling will damp much more slowly . The oscillation period λ can be obtained [5.19] for a given Q vector from

$$\lambda = 2\pi/Q \tag{5.2}$$

or

$$\lambda = 2\pi/\left|Q - 2\pi/d_0\right| \tag{5.3}$$

where d_0 is the thickness of one monolayer of interlayer.

Tab.5.5 Damping power indices (n) of the RKKY interaction in bulk materials[5.35] and in the interlayer coupling[5.19,5.21] for different cases of nesting.

RKKY Interaction (3-dimension)	
Nesting Types	n [5.35]
Complete Nesting	2
Partial Nesting	2.5
Absent Nesting	3

Interlayer Coupling (multilayer)	
Nesting Types	n [5.19,5.21]
Complete Nesting	1
Partial Nesting	1.5
Absent Nesting	2

The observed oscillations in the magnetic coupling of Fe/Cr/Fe layered structures discussed in the last section can be understood on the basis of the nesting effects in the Fermi-surface of the Cr interlayer. From fig.5.16 and tab.5.4, it can be found that the power indices, n=1.03 and 2.08 correspond to the cases of complete nesting and absence of nesting, respectively, and n=1.22 and 1.80 are between the two cases. The corresponding stationary wave vectors (Q_n) for the observed oscillatory periods through equ.5.2 or equ.5.3 are denoted in fig.5.17[5.17,5.19,5.31].

In fig.5.17, the complete nesting wave vector Q_1=0.95ΓH is well known[5.17]. It is reponsible for the 2 ML period oscillations in the coupling. Stiles[5.31] has pointed out that wave vector Q_2 and Q_3 result in oscillatory coupling with periods of 17.4Å and 13.2Å, respectively, which are well consistent with the experimental results of λ=12.6ML and 10.0ML shown in tab.5.4. In addition, vector $Q_4 \cong 0.8\Gamma H$ is also related to the oscillation with λ=10.0ML[5.37] by using equ.5.3. The experimental and the theoretical results are all cited in tab.5.6.

Tab.5.6 Theoretical and experimental results of the oscillation periods in the coupling in Fe/Cr/Fe systems.

Wave vector in Cr Fermi-Surface (fig.5.17)	*Theoretical Period*		*Experimental Period*
	λ(ML)	*Ref.*	λ(ML) (see tab.5.4)
Q_1	2.1	[5.17]	2.0
Q_2	12.2	[5.31]	12.6
Q_3	9.2	[5.31]	10.0
Q_4	10.0	[5.37]	10.0

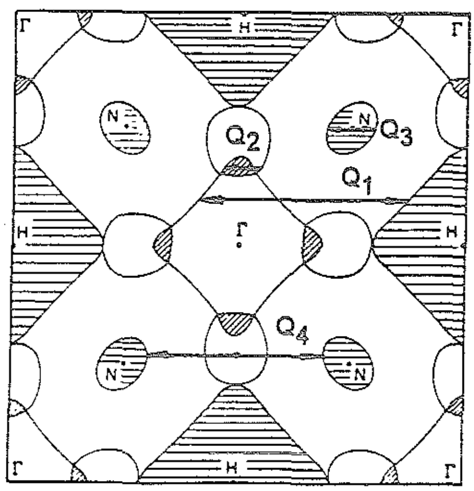

Fig.5.17 Cross section of the Cr(100) Fermi-surface (after Laurent et al[5.36]). The wave vectors which give rise to the oscillatory coupling are denoted by Q_n (n=1,2,3 and 4).

5.5.4 Fabry-Perot Effect Model

As mentioned above, the coupling damps as d_i^{-1} and d_i^{-2} for the complete and absent nesting , respectively, where d_i is the interlayer thickness. A simple model proposed by Edwards and Mathon et al[5.25] can give an interpretion of this effect.

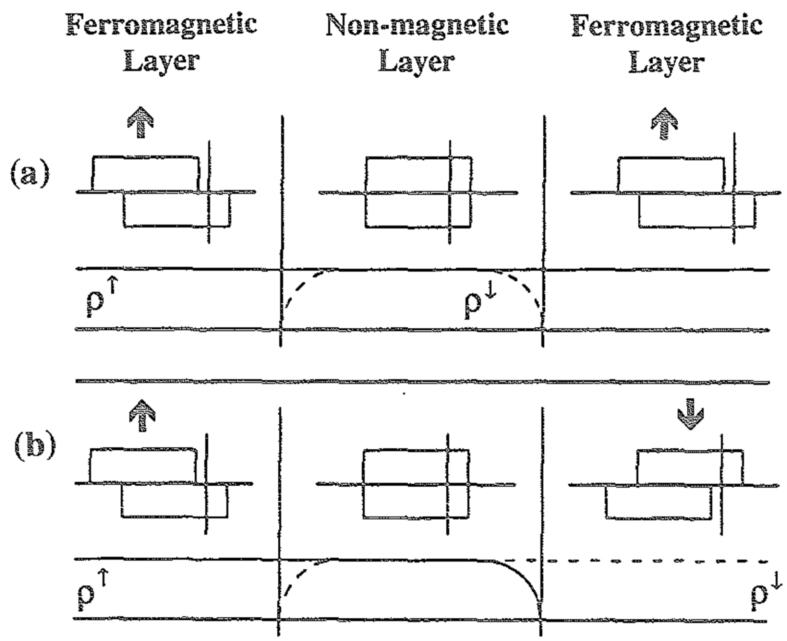

Fig.18 Schematic diagram for the densities of the states in the d band and for the densities of holes in a layered structure for FM (a) and AFM (b) coupling between two ferromagnetic layers (after Erdwards et al [5.25]).

Fig.5.18 shows a schematic diagram of spin sub-bands for a sandwich, including two ferromagnetic layers and one nonmagnetic metal layer. It indicates two cases corresponding to the ferromagnetic (FM) and antiferromagnetic (AFM) coupling states. The ferromagnetic metal has the partially occupied spin minority d band and a full majority d band. The nonmagnetic metal has equal numbers of holes in each sub-band. In the figure, $\rho^{\downarrow}$ indicates the spin-down hole density and $\rho^{\uparrow}$ the spin-up hole density. As to the FM case shown in fig.5.18(a), at both interfaces a reflection occurs in the spin-down hole densities and, thus, the in- and outgoing waves interfere with each other. For the AFM case shown in fig.5.18(b), the effects on each interface between the ferromagnetic layer and nonmagnetic interlayer occur in opposite spin densities and, therefore, no interference occurs. In this model the exchange coupling is entirely determined by the interference effect in the down spin band of the interlayer.

These effects work like a spin-dependent electron resonator, which is analogous to an optical resonator as in a Fabry-Perot interferometer. The Fabry-Perot interferometer consists of two parallel mirrors whose separation can be adjusted. In resonance an integral number of half wave-lengths of the light fits into the separation(cavity). Then there is an increase of the light intensity between the mirrors.

In the spin-dependent resonator, the two interfaces between the ferromagnetic- and nonmagnetic layer are like the two mirrors in the Fabry-Perot interferometer. The light is now replaced by the electron wave but for the ferromagneic alignment only one spin direction is reflected($\rho^{\downarrow}$). In resonance analogous to the optical case, there is an increase of $\rho^{\downarrow}$ and therefore an increse of energy (kinetic Couclomb repulsion). Then energetically it is more favorable to go to the antialiqned state(fig.5.18.b) because then the interface on the right hand side becomes transparent for $\rho^{\downarrow}$ and the resonance is lost.

In this picture the effect of nesting can be understood in such a way that many electrons from the Fermi surface having all the same Q_n contribute to the resonance. For non nesting the electrons have different Q, and there is destructive interference and a strong attenuation of the effect when the spacer thickness increases. This explains qualitatively why the attenuation is weaker for nesting.

In Conclusion: For the Fe/Cr/Fe system in total three different periods in the oscillations are found to be related to certain distances in the Fermi-surface of Cr, as predicted by theories. The attenuations of the oscillation amplitudes in the exchange coupling follow d_{Cr}^{-n} -dependent power laws with n=1.03, 1.22, 1.80 and 2.08 for different samples. They are correlated with different nesting effects, where n=1 corresponds to the complete nesting and n=2 to the absence of nesting.

5.6 Structural Properties of Fe/Cr Interfaces

5.6.1 No Phase-Slip Oscillations

Fig.5.19 shows the interlayer coupling versus the Cr-interlayer thickness (d_{Cr}) in a Fe/Cr/Fe structure made at T_S=523K. The short period oscillations in the coupling have been observed up to d_{Cr}=77Å of the interlayer thickness.

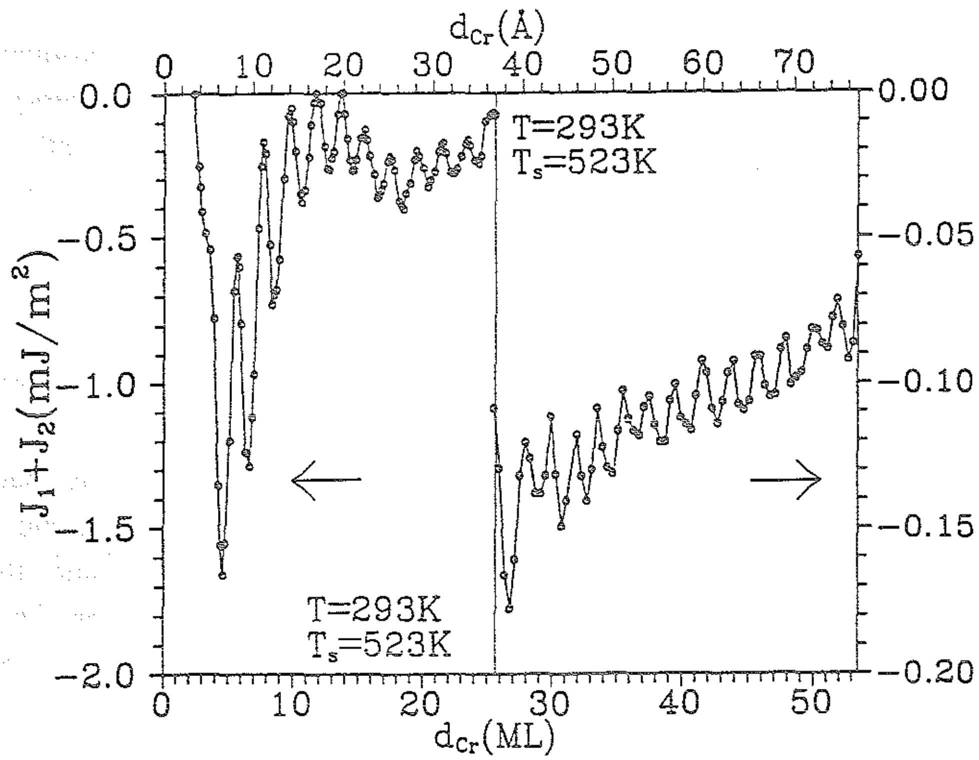

Fig.5.19 Interlayer coupling as a function of the interlayer thickness in Fe/Cr/Fe system. Here T is the measuring temperature and T_S the substrate temperature during the sample preparation.

These results should be compared with the observation by Unguris et al[5.38]. They ultilized SEMPA (scanning electron microscopy with polarization analysis) to investigate the magnetic domains in a Fe/Cr/Fe sample. Fig.5.20 shows their sample geometry (fig.5.20a) and the SEMPA image of the magnetization in the y-direction (fig.5.20b). The sample was evaporated on a [001]- Fe whisker substrate, which is part of the sample itself. In this way, the Fe/Cr/Fe sandwich structure is supposed to have the best growth so that the fine oscillations could be observed up to 80ML of Cr interlayer. The very

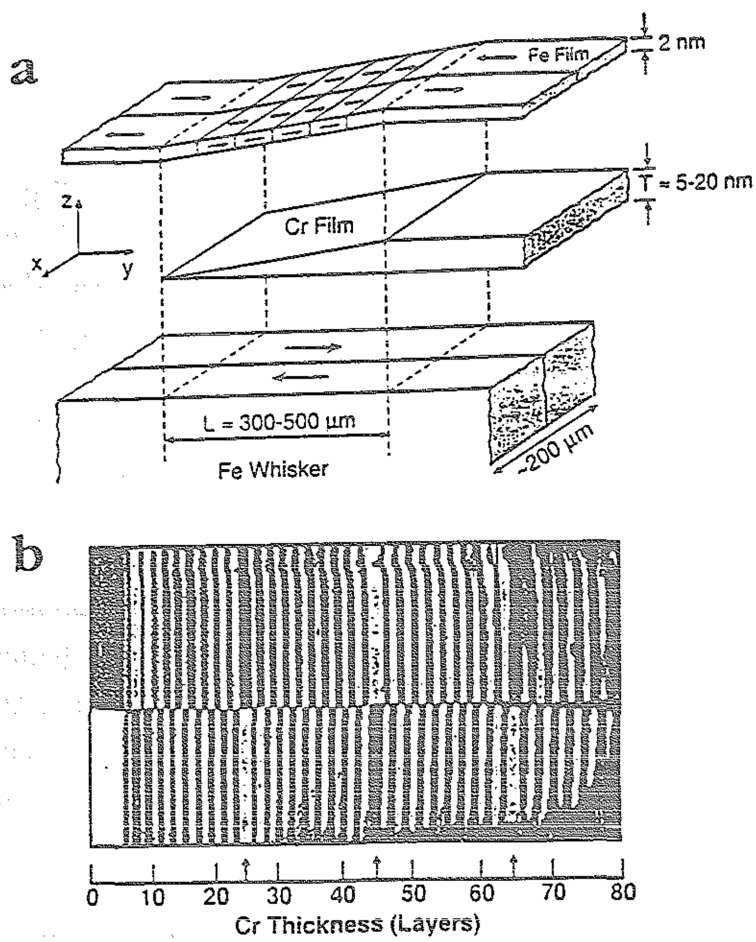

Fig.5.20 Domain configuration in a 20Å-thick iron, which is coupled with a iron whisker across a wedge-formed interlayer of Cr. T_S=623K (after Unguris et al[5.38]).

important feature in fig.5.20 are the phase-silps at the positions of d_{Cr}=24, 44 and 64 ML as denoted by arrows. This effect is thought to be due to the incommensurate spin desity wave (IMSDW) whose vector is just the well-known nesting vector Q_1=0.95ΓH in fig.5.17. This wave vector indicates that there is 5% mismatch between the spin density wave (SDW) in antiferromagnetism Cr and the bcc Cr lattice vector, so the phase-slip takes place every 20ML.

According to this, the oscillations in fig.5.19 should have two phase-slips. However, no phase-slip is observed in fig.5.19. Therefore, one may ask why there is no phase-slip in the oscillations shown in fig.5.19.

5.6.2 Interfaces of Fe/Cr

First of all, let's consider the interface quality of the samples. Fig.5.21 displays the RHEED patterns taken from each surfaces of the Fe/Cr/Fe sandwich prepared at T_S=293K and 523K. The Fe/Cr/Fe structure was deposited on a buffer layer whose RHEED patterns have been shown in fig.4.1. Streaks are clearly seen in fig.5.21(A)-(C). They are due to the reflection or transmission from 3-dimensional islands on the surfaces. Comparison with the RHEED configurations in fig.5.21(D)-(F) indicates that the surfaces of the layered structures made with higher T_S are rougher than of those with lower T_S.

Normally, the structures which show fine oscillations in the coupling have high quality. Thus, the samples evaporated at higher T_S may have better crystallinity than at the lower one. However, one achieves this advantage at the expense of the interfaces of Fe/Cr. The samples made with lower T_S may have better interface quality than with higher T_S, but the structures of the layers are not ordered enough to show short-period oscillations.

For the observing morphology of the surfaces in this system, a sample with stepped Fe, Cr and Fe layers was prepared at a T_S=523K, whose geometry is shown in fig.5.23. This structure shows 90°-type coupling. Scanning electron microscopy (SEM) is used to investigate the surfaces. The image from the surface of the

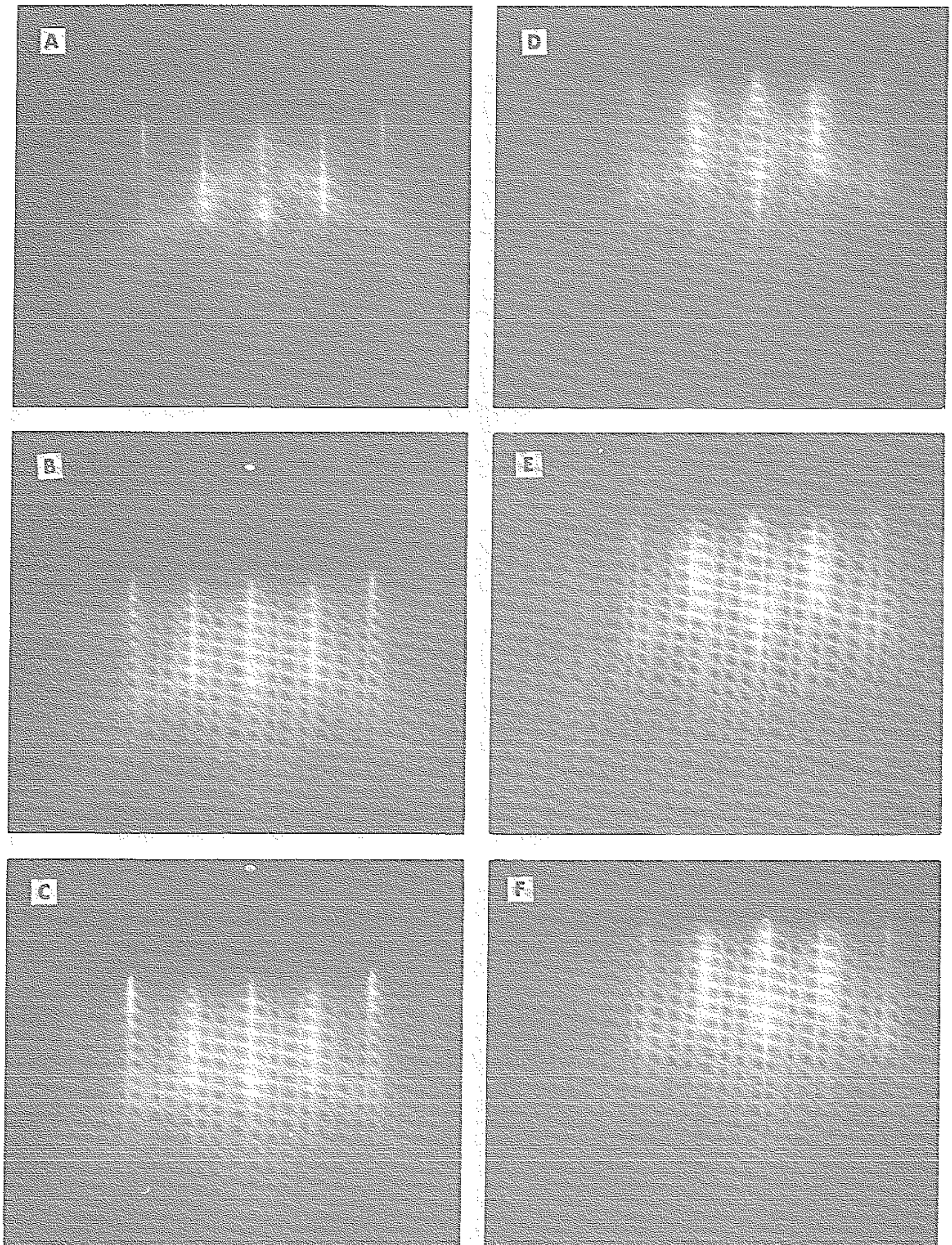

Fig.5.21 RHEED patterns from each of the surfaces of the Fe/Cr/Fe structures evaporated with different substrate temperature T_S. (A), (B) and (C) for T_S=523K, (D), (E) and (F) for T_S=293K, in which (A) and (D): first Fe layers, (B) and (E): Cr interlayers, and (C) and (F): second Fe layers. Energy of incident electron beam E=10kV and incident angle $\alpha_E \cong 2°$.

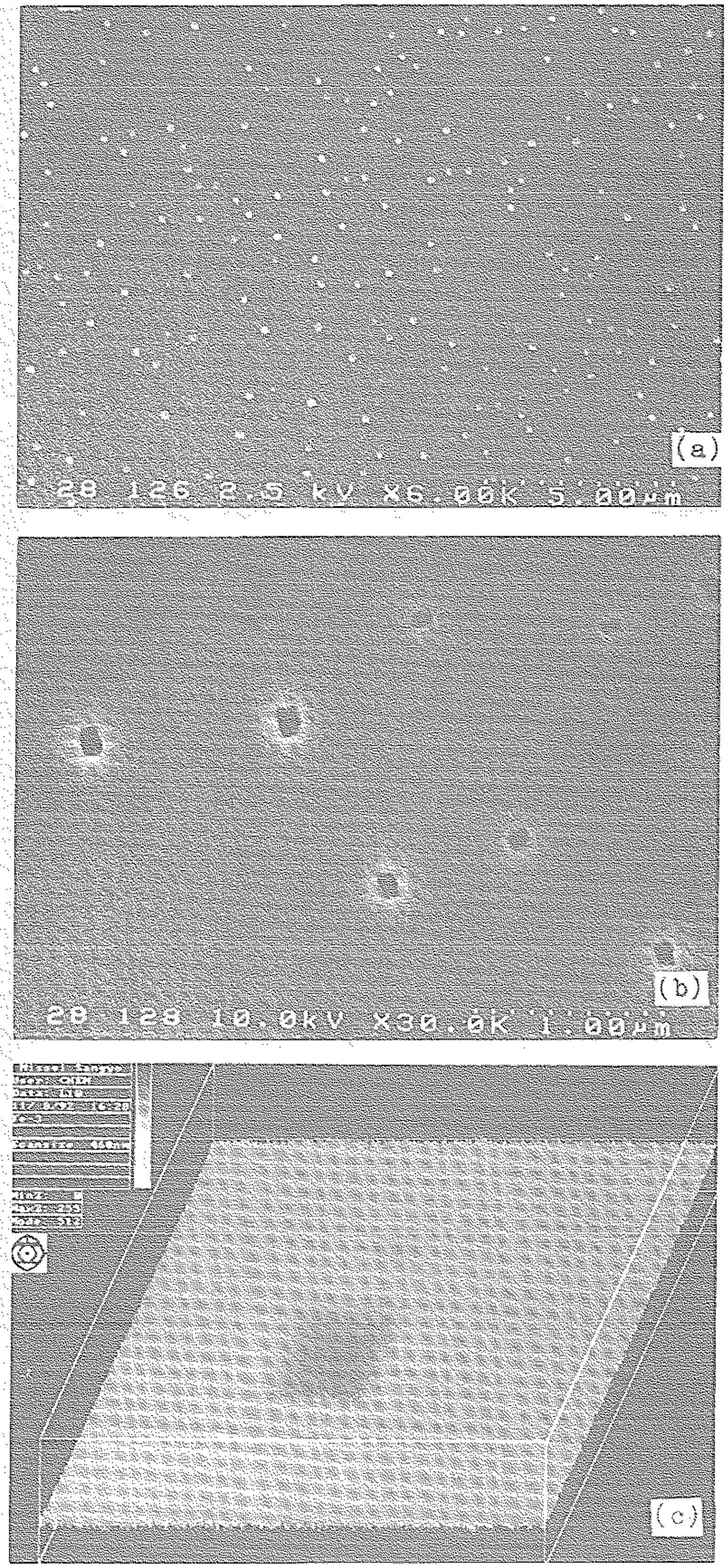

Fig.5.22 Morphology of the second Fe layer in the Fe/Cr/Fe structure made with T_S=523K, imaged by SEM with different amplifications. (c): scanning size is 4680Å×4680Å.

top Fe layer is displayed in fig.5.22. In large scanning size (fig.5.22a), many deffects have been observed on the surface. From fig.5.22(b), it can be seen that these defects are dents on the surface. One of the dents was enlarged and shown in fig.5.22(c), which has a size of about 1000×1000Å^2. Such morphology has been found on each surface of the steps in the sample. These defects are most likely due to the rather rough surface of the GaAs substrate, for roughness in the range of about 30Å has been observed on the substrate by means of scanning force microscopy [5.39]. Although the buffer layer has cured out most of the roughness, some remains up to the last layer.

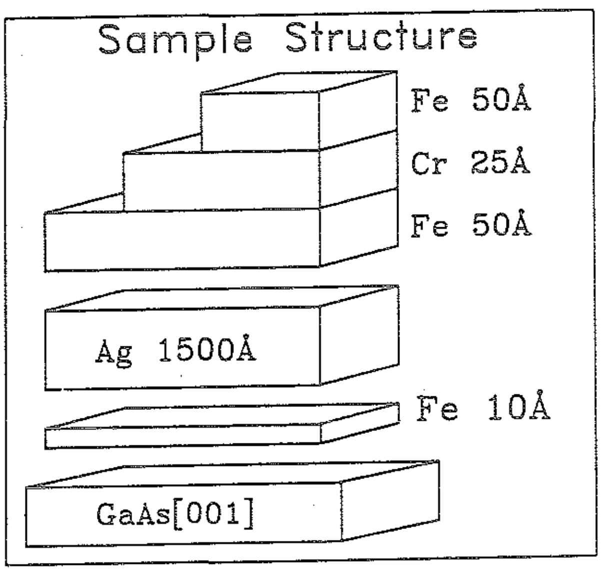

Fig.5.23 The sample structure for SEM observation.

To obtain more quantitative information of the interface, a usful tool, conversion electron Mössbauer spectroscopy (CEMS) is employed to investigate the layered systems. This part of work was done in cooperation with Dr. Ch.Sauer's group.

Special samples with a 2ML-thick isotope ^{57}Fe layer is deposited on the interfaces as a probe for CEMS studies. The geometries are indicated in fig.5.24. The sample structure (a) and (b) in fig.5.24 are for studing the structural properties of the lower and upper interfaces, respectively. In the experiment samples with different interlayer thicknesses d_{Cr} and prepared with different substrate temperatures T_s are used.

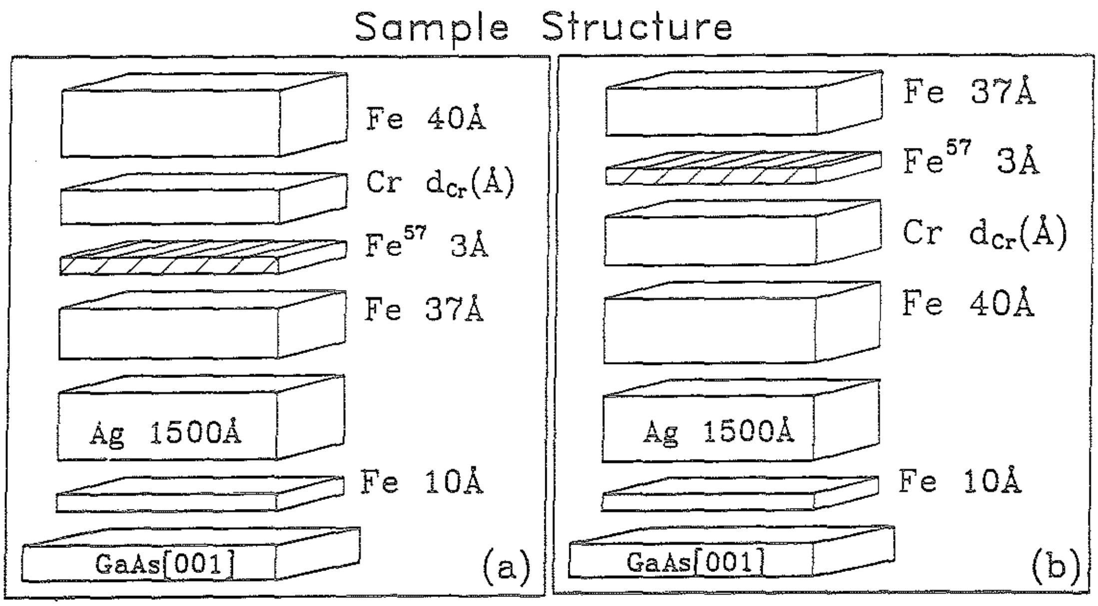

Fig.5.24 Sample structures for the CEMS investigations.

Fig.5.25 displays a typical CEMS spectrum of the upper Fe/Cr interface region in a Fe/Cr(10Å)/Fe structure which has the geometry of fig.5.24(b). There are different contribitions. From these, the associated magnetic hyperfine (hf.) fields can be deduced [5.40].

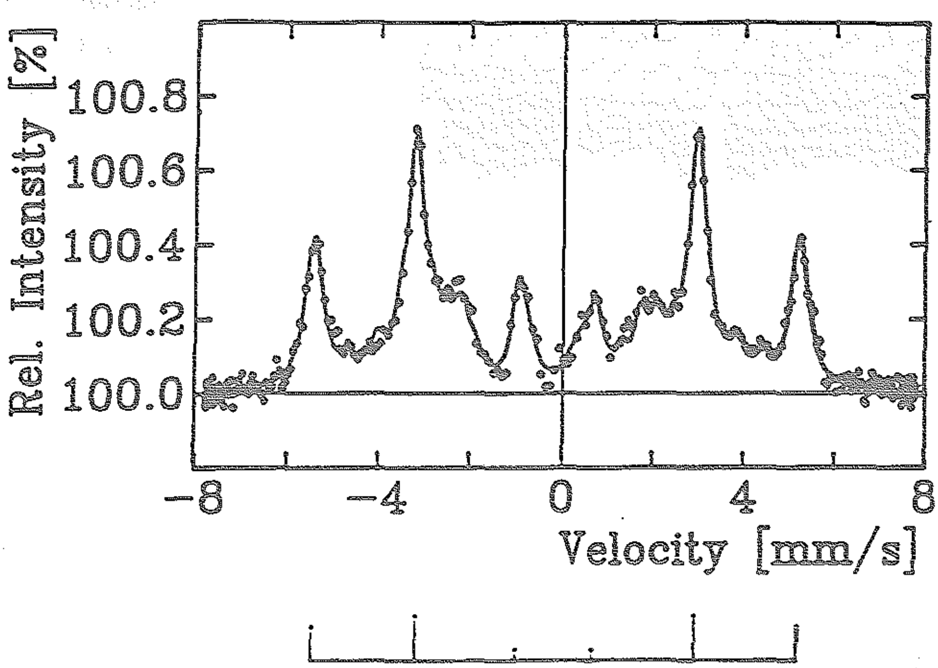

Fig.5.25 Typical CEMS spectrum of Fe/Cr interface in Fe(37Å)/^{57}Fe(3Å)/Cr(10Å)/Fe(40Å) structure (see fig.5.24b) prepared with T_S=293K. The bar diagram indicates the 6-line α-Fe "bulk" subspectrum.

In order to identify the subspectra from the experimental data, a simple model displayed in fig.5.26 can be used to describe the Fe/Cr interface[5.40]. The interface consists of different step regions and flat regions of various extensions. The ^{57}Fe probe atoms located in the flat areas will feel the hf. field corresponding to an ideal Fe/Cr interface, while the hf. fields for the probe atoms at step positions will have a deviation. Therefore, different configurations of the atoms at the Fe/Cr interfaces will show different hf. fields. From the Fe/Cr layered structure, totally, ten different Fe positions can be distinguished on an atomic scale, of which one position is in the bulk, one on the flat interface and eight at the step positions. By analyzing the subspectra from the ME data[5.41], distribution of hf.fields from all interface configurations in this model could be found as demonstrated in fig.5.27.

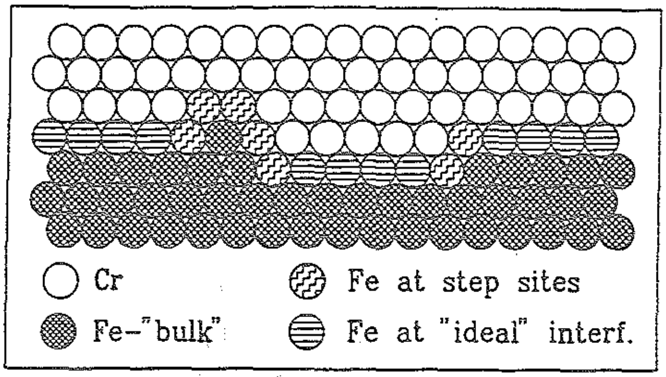

Fig.5.26 Schematic diagram of a Fe/Cr interface model (after Sauer et al[5.40]).

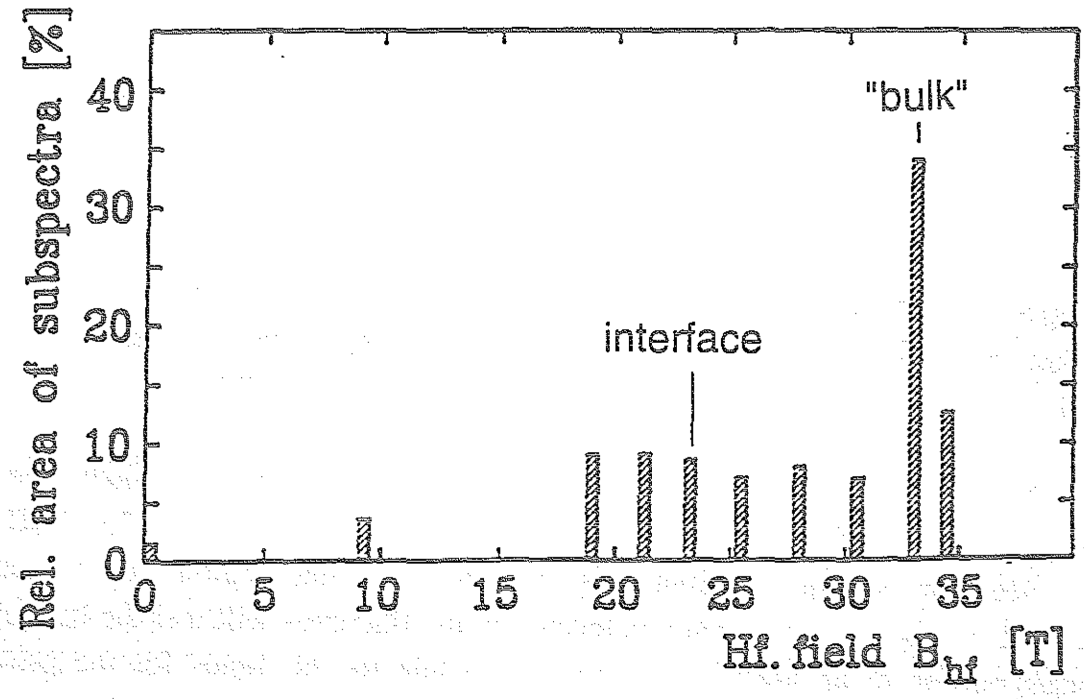

Fig.5.27 Distribution of hf. fields for different Fe positions analyzed from the CEMS spectrum in fig.5.25.

Interface roughness can be determined on the basis of this analysis. The interface condition can be described with a parameter, the near-order coefficient α ($0 \leq \alpha \leq 1$)[5.41]. For extremal cases, $\alpha=1$ denotes ideally flat interface or smooth terrace and $\alpha=0$ denotes the roughest interface with alternative Fe and Cr atoms statistically. The results of analysis from different samples are summerized in tab.5.7. The table gives also information of relative paramagnetic peak, which is another important feature and can be analyzed from the CEMS spectra. Occurence of the paramagnetic peak suggests that some Fe atoms diffuse though the interface into the Cr interlayer.

Tab.5.7 Interface information from CEMS spectrum for different samples.

Samples (refer to fig.5.24)	*T_S (K)*	*Near-order coefficient α*	*Paramagnetic peak intensity (relatively)*
Fe/^{57}Fe/Cr(10Å)/Fe Fe/Cr(10Å)/^{57}Fe/Fe	293	0.25 ~ 0.30	small
Fe/Cr(10,24Å)/^{57}Fe/Fe	523	0.20 ~ 0.25	large

Comparison in tab.5.7 suggests that the interfaces in the samples deposited with T_S=523K should be rougher than with T_S=293K, which is consistent with the above surface study by RHEED. In addition, interdiffusion at interfaces of Fe/Cr occurs more seriously in the samples made with higher T_S.

5.6.3 Discussion and Conclusion

According to the above analysis, our samples which show fine oscillations of the coupling (see fig.5.19) have rather rough interfaces of Fe/Cr. In the Cr interlayer there are Fe impurities due to diffusion through the interfaces, which would form a dilute Fe-Cr alloy. The Fe impurities will change the magnetic properties of Cr.

In 1976, Mori et al[5.42] investigated the effect of Fe impurities in Cr. Their results with other reports about this system are shown in fig.5.28. The most important observation is that the increase of Fe in Cr raises the wave length of the sinusoidal spin modulation in bulk Cr and gives rise to the first order transition from a transverse ICSDW structure of antiferromagnetism to a CSDW one, which is stable for Cr containing Fe of more than 3 at%.

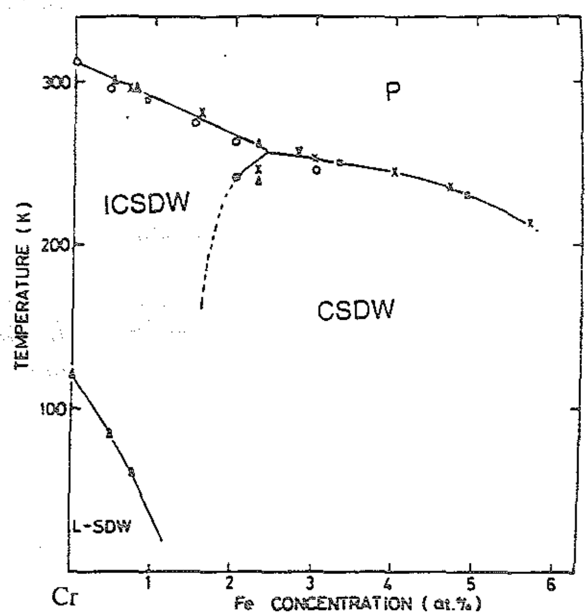

Fig.5.28 Magnetic phase diagram of the dilute Fe-Cr alloy system (after Mori et al[5.42]). P: paramagnetic state, ICSDW: transverse incommensurate spin density wave state, CSDW: commensurate spin desity wave state, L-SDW: longitudinal spin density wave state.

According to the investigation by means of CEMS, 3 at% Fe into Cr interlayer is possible for the layered structures made with $T_S \geq 523K$. It is now clear that the interdiffusion at Fe/Cr interfaces should be reponsible for the no phase-slip oscillations in fig.5.19, because the diffusion of Fe into Cr would cause the transition of Cr from the ICSDW- to the CSDW antiferromagnetic phase.

Comparison with the results by Unguris et al[5.38] indicates that their samples using Fe whisker substrates have much better quality than ours with GaAs substrates. It can be now understood why the short period oscillations in fig.5.20 are dominated by 180°-type coupling, while the oscillations in fig.5.19 have a considerable contribution of 90°-type exchange interaction. The reason is the interface roughness in the layered structures. A more detailed discussion of the 90°-type coupling will be given in the next section.

Annealing investigations on the coupling in Cr spacer systems have been presented in the previous section, which shows that the coupling could be thermally reversible in a quite large range of interlayer thicknesses up to around 700K. These results suggest that improvement of the interlayer structure is compensated by increase of roughness at interfaces after annealing. Therefore, the coupling is thermally stable. In addition, both short- and long-period oscillations of the coupling have been observed at high temperature up to 700K and the periods did not change at temperatures, which are well above the Neel temperature, T_N=311k, of bulk Cr. The reason may be that the bottom Fe layer induces a SDW through the interface in the Cr interlayer, even if SDW antiferromagnetism in bulk Cr is destroyed above T_N.

Finally, from this study, we can also conclude that the oscillatory magnetic coupling between iron layers across nonmagnetic interlayers depends on both crystalline ordered structures of the interlayers and interfaces between the iron films and the interlayers, but a smooth interface is not a necessary condition for an oscillatory coupling with short periods, while a well ordered crystalline interlayer should be reponsible for a fine oscillatory magnetic coupling.

5.7 Biquadratic Coupling

5.7.1 90°-type Magnetic Coupling

As mentioned in chapter 3, the so-called 90°-type coupling in the layered systems means that alignment of the magnetizations in the Fe layers is perpendicular. Generally, it includes contributions from both bilinear (J_1)- and biquadratic (J_2) exchange and the latter is stronger than the former. Evidence for this type coupling was found from the analysis of the Kerr domain configurations in the transition region between ferromagnetic (FM) and antiferromagnetic (AFM) coupling[5.8].

Actually, one can easily obtain the 90°-type coupling using the Fe/Cr layered structures evaporated at an elevated substrate temperature in a rather large range of interlayer thickness. An example of a M(H) curve which shows 90°-type coupling is displayed in fig.5.29. This is from a Fe/Cr/Fe sample with the thickest interlayer which shows still coupling we observed so far. This thickness is as high as 86ML Cr.

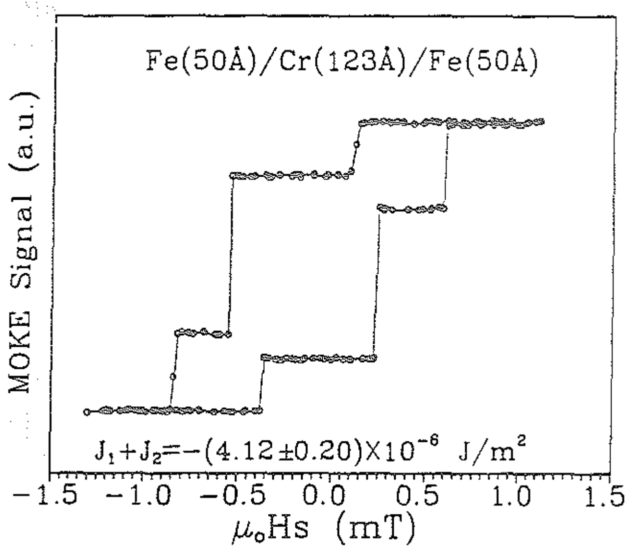

Fig.5.29 Hysteresis loop measured by means of MOKE from Fe(50Å)/Cr(123Å)/Fe(50Å) sandwich made with T_S=523K. The total coupling strength is indicated.

In addition, the 90°-type coupling shows a strong temperature dependence. Fig.5.30(a) displays an example of coupling versus temperature in a Fe/Cr/Fe structure prepared with T_S=293K. This sample shows 90°-type coupling only below 200K. Otherwise, if the temperature is higher than 200K, only FM coupling is observed. The coupling strength in this sample decreases very fast with increase of temperature. Fig.5.30(b) shows the results of absolute measurement by means of SQUID (superconducting quantum interface device) in this sample. For the SQUID measurement, each point was obtained with the same external field of 1mT after saturating the sample along an easy axis in the film plane. From the temperature dependence of the magnetic moment, it can be seen that the total moment in the 90°-type coupling region is just half of that in the FM coupling region. It is obvious that in the case of FM coupling the magnetic moments in both Fe layers have parallel alignment and will contribute together to the measurement, while for the case of 90°-type coupling only the moment in one iron layer is measured and the moment in the other layer has perpendicular alignment and therefore, not detected. This is an obvious comfirmation of the 90°-type coupling.

Fig.5.30 Temperature dependence of interlayer coupling (a) and magnetic moment (b) in a Fe(50Å)/Cr(15.4Å)/Fe(50Å) structure. Here M is the magnetization at RT obtained from the experimental data.

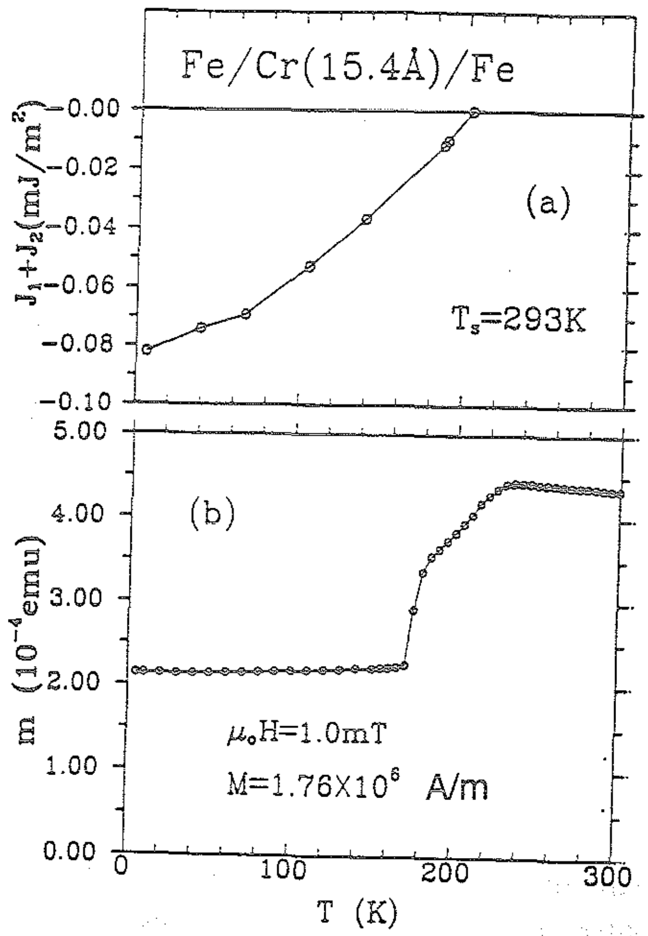

5.7.2 Influence of Interface Roughness on Biquadratic Coupling

In previous sections, one can find that the layered structures with rougher interfaces have a larger contribution of biquadratic coupling. In order to find out the influence of the interface roughness on the coupling, roughness is introduced in the interfaces by introducing an Ag layer into the Cr interlayers. Sample structures for this investigation are shown in fig.5.31.

RHEED and AES were used to monitor the structure growth. Rougher surfaces of Cr in these structures have been observed than without the additional Ag layers. With AES we detected Ag on the Cr surfaces. Thus, the added Ag layer between the Cr interlayer diffuses into the Cr and gives rise to rough interfaces.

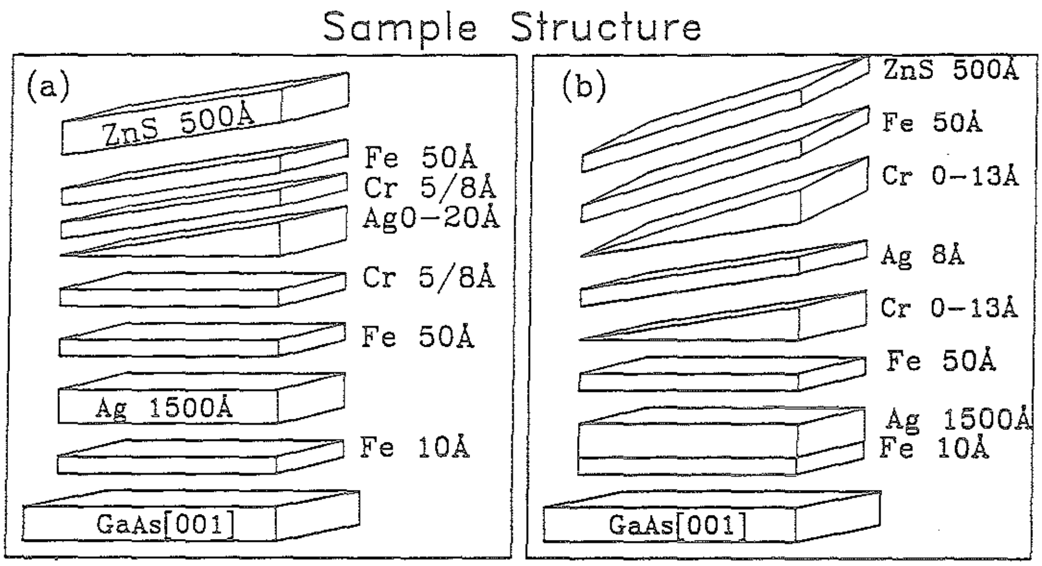

Fig.5.31 Sample geometries

Fig.5.32 demonstrates the results of coupling versus Ag thickness in a layered structure having the geometry of fig.5.31(a). In this sample a wedge-shaped silver layer between two 5Å-thick Cr layers is introduced. It was fabricated with a T_S=293K. Without the additional silver layer, this structure has a 10Å-thick interlayer of Cr and shows strong AFM coupling {panel (a) in fig.5.32}. However, by only adding at least a 2Å-thick Ag layer the coupling decreases drastically and changes to 90°-type one {panel (b) in fig.5.32}. As the Ag thickness increases further, the coupling intensity seems to saturate.

The strongly reduced coupling means that the saturation field in this system is much smaller than in the normal Fe/Cr/Fe system. The Fe/Cr layered systems are well known for their GMR effect. Small switch fields could be attained by using this structure in field sensors. Therefore, the Fe/Cr/Ag layered systems which show weakly 90°-type coupling may be promising candidates for GMR sensors, because they have relatively small saturation fields and still preserve the large GMR effect due to the Fe/Cr interfaces.

Fig.5.33 shows the thickness(d_{Ag})-dependence of the coupling in the Fe/Cr(8Å)/Ag/Cr(8Å)/Fe system. Without the Ag layer this structure shows FM coupling, but as Ag is inserted, it shows 90°-type coupling. The coupling has a strong temperature dependence like normal biquadratic coupling, and displays some fine structures at low temperatures.

Fig.5.34 shows the results of exchange coupling in the structure of fig.5.31(b) which was made at T_S=373K and has an Ag layer of fixed thickness between two wedge-formed Cr layers. Without the silver layer, the coupling in this structure should oscillate with a long period like in fig.5.2(a) or fig.5.8. With a 8Å-thick silver layer, The first two coupling peaks can be clearly seen and do not shift compared to fig.5.2(a), but the AFM coupling is strongly reduced and the second peak is dominated by biquadratic coupling. Although the first peak is still AFM, its coupling intensity is only one sixth of that without the additional Ag layer. The region which is the second FM area in fig.5.2(a) shows 90°-type coupling in fig.5.34.

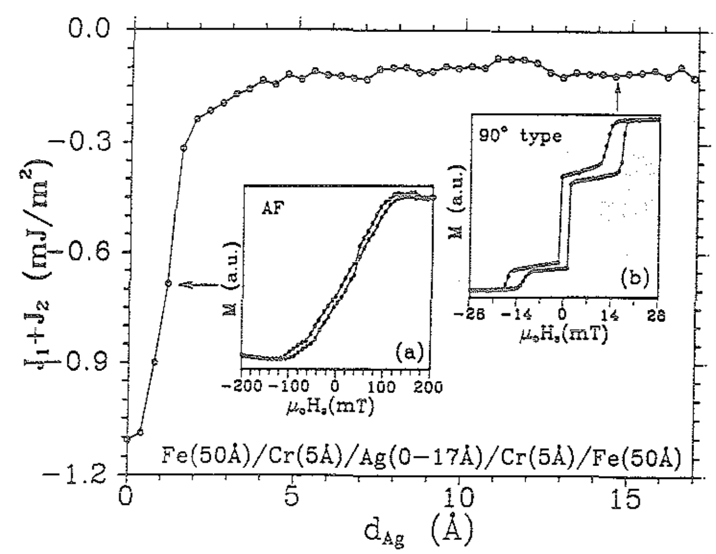

Fig.5.32 Exchange coupling as a function of the thickness of the silver layer in a Fe(50Å)/Cr(5Å)/Ag(0-17Å)/Cr(5Å)/Fe(50Å) system prepared with T_S=293K. Typical hysteresis cuvesfor the coupling are indicated, where panel (a): AFM- and (b) 90°-type coupling.

As mentioned above, the added Ag layer to the Cr interlayer in a Fe/Cr/Fe layered structure is to yield roughness at the interfaces and to influence the structure of the Cr interlayer. With respect to the coupling in these structures, the role of the added Ag layer is to reduce the bilinear coupling intensities and at the same time to strengthen the biquadratic coupling. Thus, the interface roughness should be reponsible for the biquadratic coupling. The following experimental data supports this statement.

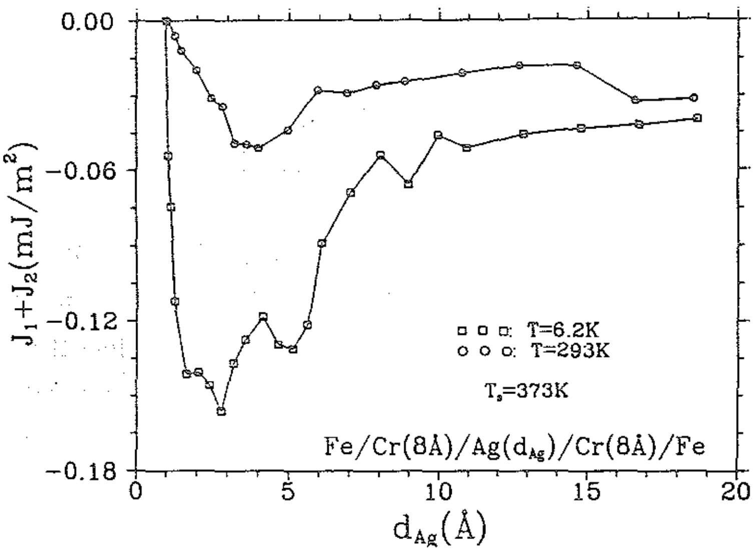

Fig.5.33 Exchange coupling as a function of thickness of the silver layer in a Fe(50Å)/Cr(8Å)/Ag (0-20Å)/Cr(8Å)/Fe(50Å) system prepared with T_S=373K. The coupling curves were measured at T=6.2K and T=293K.

Fig.5.34 Interlayer coupling as a function of the Cr thickness in a Fe(50Å)/Cr(0-13Å)/Ag(8Å)/Cr(0-13Å)/Fe(50Å) system prepared with T_S=373K. T is the measuring temperature.

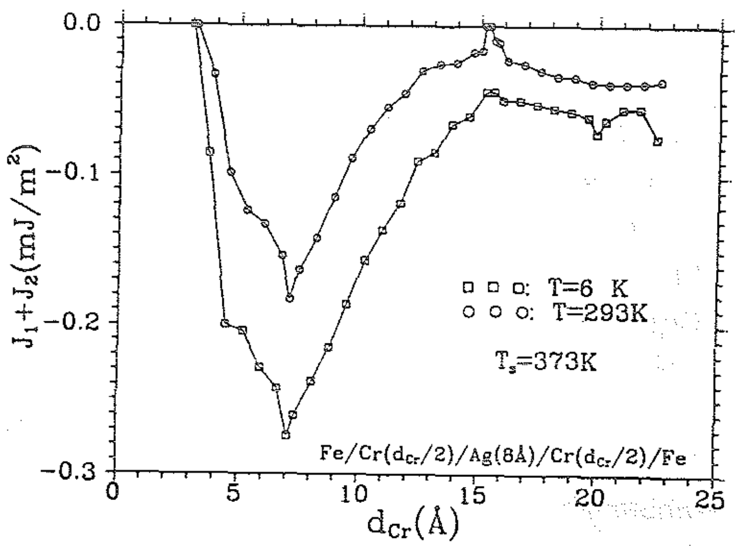

Interlayer coupling versus the thickness of the Fe layer in a Cr spacer system is displayed in fig.5.35 with its sample structure. In this sample two wedged Fe layers were prepared beside a 13Å-thick Cr interlayer with T_s=293K. This structure shows AFM coupling imposed on biquadratic one. Bilinear- and biquadratic coupling contributions in this structure can be separated by analysing the hysteresis curve. In fig.5.35 the bilinear coupling (J_1) versus the Fe thickness follows the same trend of change as the total coupling intensities, while the biquadratic one seems to be independent of the Fe thicknesses. These results suggest that the bilinear coupling should depend on the thickness of the magnetic layers as well as the interlayer thickness and the biquadratic coupling be originated from interface roughness, because the interface roughness should would stay on the same level in a wedge-shaped layered structure.

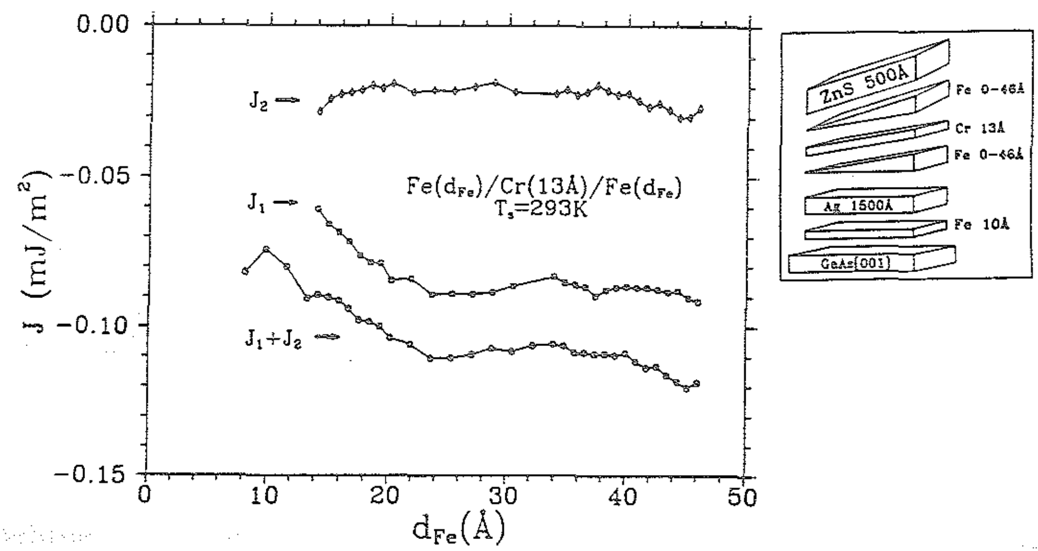

Fig.5.35 Exchange coupling as a function of Fe thickness in a Fe(0-46Å)/Cr(13Å)/Fe(0-46Å) system prepared with a T_S=293K.

As to the mechanism of the biquadratic coupling, Slonczewski[5.28] has proposed a model on the basis of interface roughness. According to his theory, the biquadratic coupling arises from spatial fluctuations in the bilinear coupling resulting from thickness fluctuations in the interlayer. Our experimental results are consistent with the central idea of the theory. The theory predicts a relation between biquadratic coupling (J_2) and fluctuations in bilinear coupling (ΔJ_1) as

$$J_2 = -(\Delta J_1)^2 L^2 / (\pi^4 A d_{Fe}) \qquad (5.4)$$

where A is the Fe intralayer exchange constant, L is a characteristic terrace length of the interfaces, and d_{Fe} is the thickness of the Fe films. Because ΔJ_1, the fluctuation of the bilinear coupling is due to the thickness fluctuation of the interlayer, for a given interlayer thickness, ΔJ_1 is constant. Likewise, for a given layered structure, the terrace length L should be also a constant. Therefore, according to equ.5.4, the strengths of the biquadratic coupling will decrease with increasing Fe thickness (d_{Fe}). Our experimental results do not indicate this trend. In opposite, the bilinear coupling depends on the thicknesses of the Fe layers. It should be noted that we do observe oscillations of the bilinear coupling as a function of the Fe thickness in a Fe/Cr/Fe structure with a fixed Cr thickness prepared at 523K. These oscillations have been predicted by recently theoretical approaches[5.42,5.43].

5.7.3 Anomalous Temperature Dependence of Biquadratic Coupling

Biquadratic coupling shows a strong temperature dependence. Its temperature dependence is not always monotonous and sometimes can show a maximum. If the thickness of the interlayer is very large, the biquadratic coupling shows a anomalous behavior. It can be seen from a sample with a steep wedge interlayer in fig.5.36.

In fig.5.36 the coupling as a fuction of the interlayer thickness was measured at 6.2 and 293K. When the Cr thickness is less than 45Å, Normally, the coupling is enhanced at lower temperatures. As d_{Cr} is above 45Å, however, the biquadratic coupling is reduced at low temperatures and will be switched to FM coupling as d_{Cr} is thicker than about 90Å.

For gaining more detailed information, the sample of Fe(50Å)/Cr(95Å)/Fe(50Å) prepared under the same condition as the wedge sample is used to measure its temperature properties. The results are shown in fig.5.37. In this structure contribution from the bilinear is very weak and can be negligible, while the biquadratic coupling appears only within a temperature range of 130 to 470K and changes to FM coupling beyond this temperature range (fig.5.37a). Fig.5.37(b) shows magnetic moments at various temperatures from absolute measurement by SQUID. Its measuring procedure was the same as that for the layered sample whose results has been displayed in fig.5.30, but an opposite trend with temperature has been observed. Measurement of AC susceptibility (fig.5.37c) in this layered structure gives the same critical point of about 210K as SQUID.

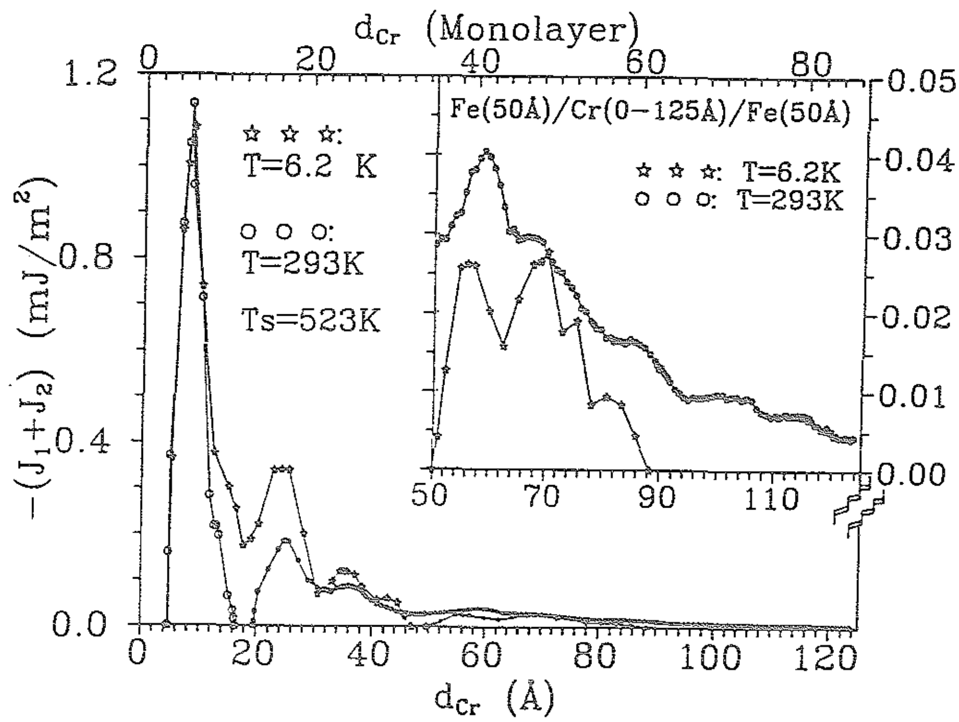

Fig.5.36 Magnetic coupling versus interlayer thickness of Cr in a Fe(50Å)/Cr(0-125Å)/Fe(50Å) system made with T_S=523K. The coupling curves were measured at T=6.2K and 293K. The inserted picture is a enlarged part of the curves corresponding the same Cr thickness range.

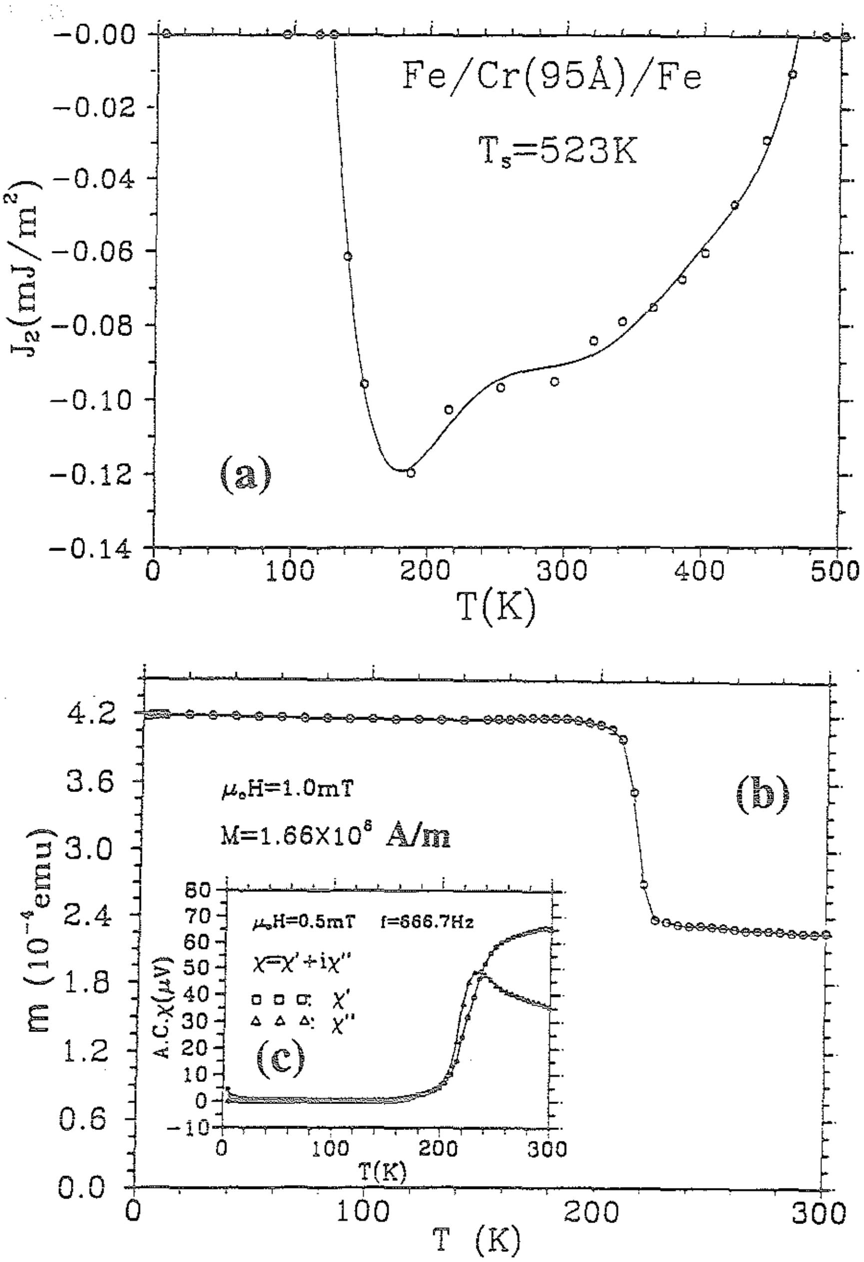

Fig.5.37 Temperature dependence of interlayer coupling (a), magnetic moment (b) and AC susceptibility (c) in the Fe(50Å)/Cr(95Å)/Fe(50Å) structure.

The existing theories about the biquadratic coupling might be hardly to explain this temperature dependence in fig.5.36 and 5.37. Since the coercive force is very large ($\mu_0 H_s \approx 5mT$) at low temperature, this behavior of biqudratic coupling with temperature may be related to mechanism of coercivity in the magnetic layers due to pinning effect. In addition, the critical temperature where 90°-type coupling switches to FM coupling is around 130K. This is also the critical temperature for transformation of transverse SDW to longitudinal SDW in Cr (see fig.5.28). This transformation in Cr may have effect on the coupling.

Thus, for the biquadratic coupling the existing theories could interpret some experimental results, but a final conclusion is still impossible.

5.8 References

[5.1] P.Grünberg, R.Schreiber, Y.Pang, M.B.Brodsky and H.Sowers, Phys. Rev. Lett. 57 (1986) 2442.

[5.2] G.Binasch, P.Grünberg, F.Saurenbach and W.Zinn, Phys. Rev. b39 (1989) 482.

[5.3]. M.N.Baibich, J.M.Broto, A.Fert, F.Nguyen van Dau, F. Petroff, P.Etienne, G.Creuzet, A.Friedderich and J.Chazelas, Phys. Rev. Lett. 61 (1988) 2472.

[5.4]. S.S.P.Parkin, N.More and K.P.Roche, Phys. Rev. Lett. 64 (1990) 2304.

[5.5]. S.Demokritov, J.A.Wolf and P.Grünberg, Europhys. Lett. 15 (1991) 881; S.Demokritov, J.A.Wolf, P.Grünberg and W.Zinn, Mater. Res. Soc. Symp. Proc. 231 (1992) 133.

[5.6]. J.Unguris, R.J.Celotta and D.T.Pierce, Phys. Rev. Lett. 6 (1991) 140.

[5.7]. S.T.Purcell, W.Folkerts, M.T.Johnson, N.W.E.McGee, K.Jager, J. aan de Stegge, W.B.Zeper, W.Hoving and P.Grünberg, Phys. Rev. Lett. 67 (1991) 903.

[5.8]. M.Rührig, R.Schäfer, A.Hubert, R.Mosler, J.A.Wolf, S.Demokritov and P.Grünberg, Phys. Sol. Stat. (a) 125 (1991) 635.

[5.9]. B.Heinrich, J.F.Cochran, M.Kowalewski, J.Kirschner, Z.Celinski, A.S.Arrot and K.Myrtle, Phys. Rev. B44 (1991) 9348.

[5.10]. J.A.,Wolf, Dissertation, University of Cologne (1993); and Jül-2743, Repts, KFA Research Center Jülich, March 1993.

[5.11]. A.Fuß, Dissertation, University of Cologne (1993); and Jül-2740, Repts, KFA Research Center Jülich, March 1993.
[5.12]. A.Fuß, J.A.Wolf, and P.A.Grünberg, to be published.
[5.13]. S.Demokritov, J.A.Wolf, P.A.Grünberg and W.Zinn, Mat. Res. Soc. Symp. Proc. Vol.231 (1992) 133.
[5.14]. A.Chaiken, T.M.Tritt, D.J.Gillespie, J.J.Krebs, P.lubitz, M.Z.Harford and G.A.Prinz, J. Appl. Phys. 69 (1991) 4798.
[5.15]. A.Barthelemy, A.Fert, M.N.Baibich, S.Hadjoudj, F.Petroff, P.Etienne, R.Cabenel, S.Lequin, F.Nguyen Van Dau and G.Creuzet, J. Appl. Phys. 67 (1990) 5908.
[5.16]. A.Fuß, S.Demokritov, P.A.Grünberg and W.Zinn, J. Magn. Magn. Mater. 103 (1992) L221.
[5.17] Y.Wang, P.M.Levy and J.L.Fry, Phys. Rev. Lett. 65 (1990) 2732.
[5.18] P.Bruno and C.Chappert, Phys. Rev. Lett. 67 (1991) 1602 and 2592.
[5.19] P.Bruno and C.Chappert, Phys. Rev. B 46 (1992) 261.
[5.20] Y.Yafet, Phys. Rev. B 36 (1987) 3948.
[5.21] C.F.Majkrzak, J.W.Cable, J.kwo, M.Hong, D.B.McWhan, Y.Yafer, J.V.Waszczak and C.Vettier, Phys. Rev. Lett. 56 (1986) 2700.
[5.22] W.Baltensperger and J.S.Helman, Appl. Phys. Lett. 57 (1990) 2954.
[5.23] F.Herman, J.Sticht and M.Van Schilfgaarde, in Mat. Res. Soc. Symp. Proc. edited by S.S.P.Parkin, et al., 1992, vol. 231, p. 195.
[5.24] N.Garcia and A.Hernando, J. Magn. Magn. Mater. 99 (1991) L20.
[5.25] D.M.Edwards, J.Mathon, R.B.Muniz and M.S.Phan, Phys. Rev. Lett.67 (1991) 493; J.Phys.Condens.Mater. 3(1991) 4941.
[5.26] J.Mathon, J.Magn.MAgn.Mater. 100 (1991) 527.
[5.27] J.Barnas, J.Magn.Magn.Mater. 111 (1992) L215.
[5.28] J.C.Slonczewski, Phys. Rev. Lett. 67 (1991) 3172.
[5.29] Daniel Stoeffler and Francois Gautier, J. Magn.Magn.Mater. 121 (1993) 259.
[5.30] P.Lang, L.Nordstrom, R.Zeller and P.H.Dederichs, 71 (1993) 1927.
[5.31]. M.D. Stiles, "Exchange Coupling in Magnetic Heterostructures", unpublished.
[5.32]. M.A.Ruderman and C.Kittel, Phys. Rev.96 (1954) 99.
[5.33]. T.Kasuya, Prog. Theor. Phys. 16 (1956) 45.
[5.34]. K.Yosida, Phys. Rev. 106 (1957) 893.

[5.35]. L.M.Roth, H.J.Zeiger, and T.A.Kaplan, Phys. Rev. 149 (1966) 519.
[5.36]. D.G. Laurent, J.Callaway, J.L.Fry and N.E.Brener, Phys. Rev. B. 23 (1981) 4977.
[5.37]. P.M.Levy, private communication.
[5.38]. Unguris, R.J.Celotta and D.T.Pierce, Phys. Rev. Lett. 6 (1991) 140. and John Unguris, Daniel T.Pierce, Robert J.Celotta, and Joseph A.Stroscio, to appear in Magnetism and Structure in Systems of Reduced Dimension, Proceedings of the NATO Advanced Research Workshop.1993.
[5.39]. M.Schneider and V.Cros, private communication.
[5.40]. Ch.Sauer and W.Zinn, "Conversion Electron Mössbauer Spectroscopy of Magnetic Multilayers", in "Magnetic Multilayers", edt, L.H.Bennett and R.E.Watson (World Scientific, Singapore, 1993).
[5.41]. Ch.Sauer and E.Y.Tsymbal et al, private communication.
[5.42]. M.Mori, Y.Tsunoda and N.Kunitomi, Sol. Stat.Comm. 18 (1976) 1103, 1105.
[5.43]. J.Barnas, J. Magn. Magn. Mater., 111 (1992) L215.
[5.44]. P.Bruno, "Oscillations of interlayer exchange coupling versus ferromagnetic layers thickness", to be published in Europhsics Letters.

6 Noble Metal Spacer Systems

With 5 Figures and 2 Tables

6.1 Introduction

In the last chapter the interlayer coupling with Cr spacers has been presented. From the RKKY like theories[6.1,6.2] it has been known that the oscillatory periods in the interlayer coupling are connected with certain distances at the Fermi-surface of the interlayer materials. Therefore it is not surprising that there are many possible periods in the oscillations of the interlayer coupling with Cr spacers due to its complex topology of the Fermi-surface. Compared to this, the noble metals, Cu, Ag and Au, have simple electronic bands which are all similar. Their Fermi-surfaces are well known and established. Therefore studies of the magnetic exchange coupling with noble metal spacers are of interest and can avoid a lot of complexities. In addition, for (001)-plane growth, Au and Ag have a very good match to the Fe lattices and therefore well grown samples, suitable for reliable results, are possible. Since the elements, Cu, Ag and Au, are mutually soluble, the alloys of Au and Cu have been also used as interlayers for the studies of the exchange coupling. One purpuse of this chapter is to show that the oscillatory coupling in the noble spacer systems can be simply understood using the RKKY like theory, and the other aim is to find out whether interlayer coupling can be used for an examination of the Fermi surfaces of alloys.

6.2 Magnetic Properties of Fe-Noble Metal Systems

The samples used for this study are all wedge-shaped. The structures and preparation are similar to that for Cr spacer but in different substrate temperatures.

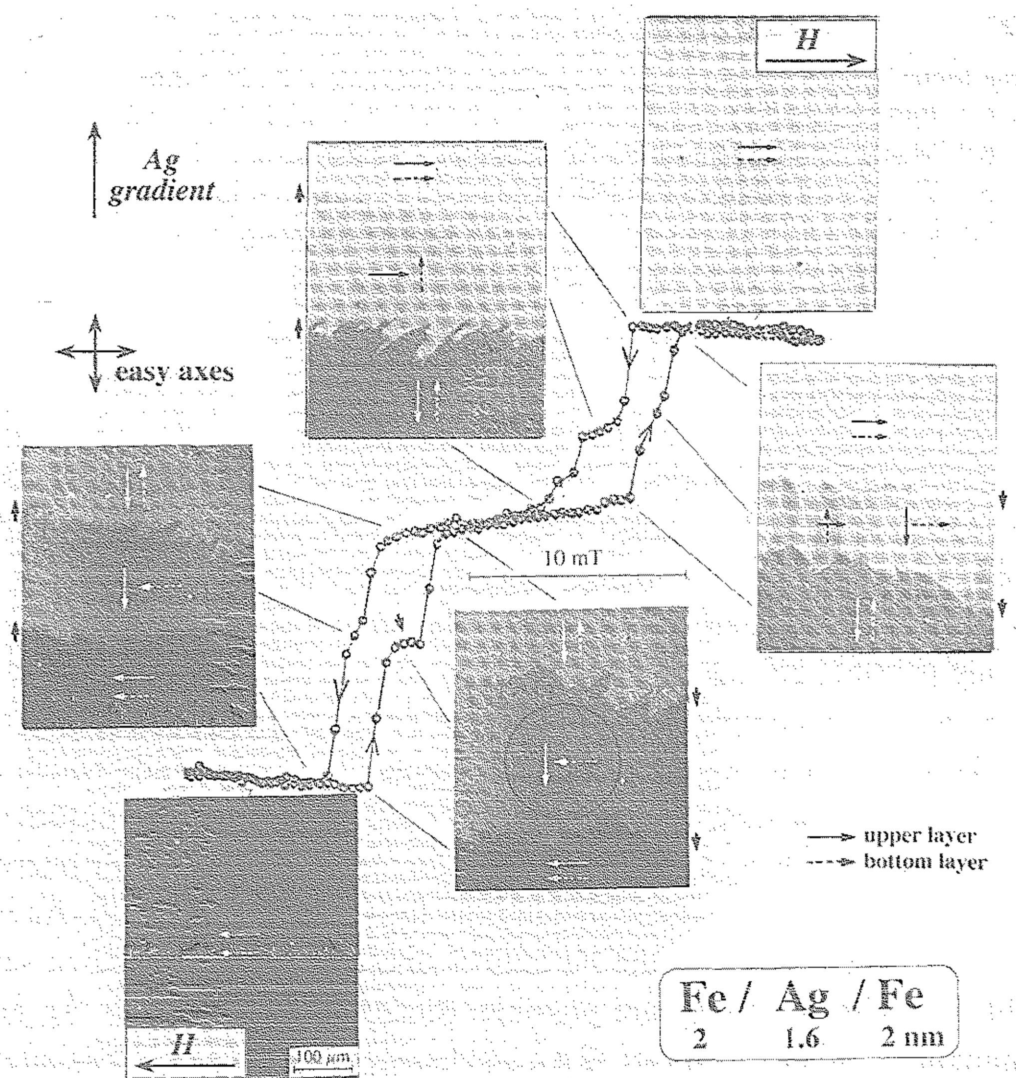

Fig.6.1 Hysteresis loop from a Fe(20Å)/Ag (0-37Å)/Fe(20Å) wedge structure at the position of d_{Ag}=16Å with 90° -type coupling superimposed on AFM coupling. The attached domain patterns reveal the micromagnetic states of the structure during the remagnetization process [6.3].

The interlayer coupling can be evaluated from hysteresis loops measured by MOKE. The typical hysteresis loops obtained from a Fe/Ag/Fe(001) layered structure for different coupling areas were shown in fig.3.3. The theoretical analyses of the hystereses and theoretical curves have been given in this figure too (see chapter 3). Fig.6.1 shows one of these loops with d_{Ag}=16Å. In order to be sure about the interpretation of this M(H)-curve the magnetic domains corresponding to the various parts of the curve have been investigated by means of a Kerr microscope. The characteristic patterns representing the whole remagnetization process have been included in fig.6.1. The magnetization directions as deduced from the grey scales of the Kerr contrast and the domain wall orientations have been indicated. In this hysteresis the biquadratic coupling is superimposed to the bilinear coupling. As an example let's have a closer look at the plateau marked by an arrow. The corresponding domain configuration reveals that it is due to a domain with perpendicularly aligned magnetization directions moving through the focus of the laser beam during the MOKE measurement. The spot size of the incident laser is shown with a circle.

The experimental results of the oscillatory coupling in Fe/Ag/Fe system are displayed in fig.6.2(a). The experimental results of the coupling for Au and Cu spacer systems taken from literature [6.4] are shown in fig.6.3(a) and fig.6.4(a).

6.3 Theoretical Analysis and Discussion

According to the theory proposed by Bruno and Chappert[6.1], the oscillation periods λ_n are connected with certain distances Q_n at the Fermi-surface of the interlayer materials via the relation

$$\lambda_n = 2\pi/Q_n \quad (n=1,2) \qquad (6.1).$$

Here the Q_n (n=1, 2) are the small and the large "caliper" of the dog's bone orbits in the [100]-direction, as indicated in figs.6.2(b)-6.4(b). On the basis of the RKKY theory the dependence of the J_1 parameter on the interlayer thickness d_i for fixed temperature may be written in the form

$$J_1=[A_1\sin(2Q_1d_i + \Phi_1) + A_2\sin(2Q_2d_i + \Phi_2)]/d_i^2 \qquad (6.2).$$

For the evaluation of the experimental results the periods λ_1 and λ_2, amplitudes A_1 and A_2, and phases Φ_1 and Φ_2 are used as adjustable parameters. In practice, apart from λ_1, λ_2, and Φ_1, Φ_2, only the ratio of A_1/A_2 is fixed and in this way J_1 is in arbitrary units. Strictly this theory makes only predictions for values of d_i corresponding to a number of filled monolayers and should be used in this sense. On this basis equs.6.1 and 6.2 have been used to fit the experimental data of the noble metal spacer systems and the results of the analysis are displayed in figs.6.2(b)-6.4(b). The fitted values for the periods, amplitude ratios and phases are summerized in tab.6.1. These figures show also electronic band structures, the well known dog's bones, with arrows which indicate the "caliper" vectors Q_n (n=1,2), and the sizes of which are consistent with the resulting λ_2/λ_1 ratio.

Tab.6.1 Experimental and theoretical oscillation periods for noble metal spacer systems, including data from literatures. The theoretical periods are taken from ref. [6.1].

Noble metal	*Theoretical period (ML)*		*Experimental parameters obtained from fitting with equ.6.1 and 6.2*					*References*
	λ_1	λ_2	λ_1(ML)	λ_2(ML)	A_1/A_2	Φ_1	Φ_2	
Au (100)	8.60	2.51	8.00	2.00	1.40	0.63	0.94	This work
			8.60	2.48	2.1	0.44	3.14	[6.5]
Ag (100)	5.58	2.38	5.20	2.30	1.20	-1.49	-1.49	This work
			5~6*					[6.6]
			5.73	2.37	1.02	4.80	-0.43	[6.7]
Cu (100)	5.88	2.56	7.5*					[6.8]
			8.0	2.59	1.25	14.2	14.5	[6.9]
			9.30	4.10	1.70	2.01	2.52	This work
$Au_{0.45}Cu_{0.55}$			7.6*	2.0*				This work

* : obtained directly (without fitting) from the experimental data.

The Fe/Cu/Fe - system has also been studied earlier[6.8,6.9] and the Fe/Ag/Fe - system has been investigated at the same time by other groups[6.6,6.7]. For comparison the data from these references are also given in tab.6.1.

Fig.6.2. Thickness dependence of the exchange coupling in a Fe/Ag/Fe (100) layered structure. (a) Experimental results evaluated from M(H)-curves; (b) calculated oscillation on the basis of equ.6.1 and 6.2 using the indicated parameters. Part with full lines can be compared with the experiment. The shape of the corresponding electronic bands (dog's bone orbit) and relevant calipers are shown.

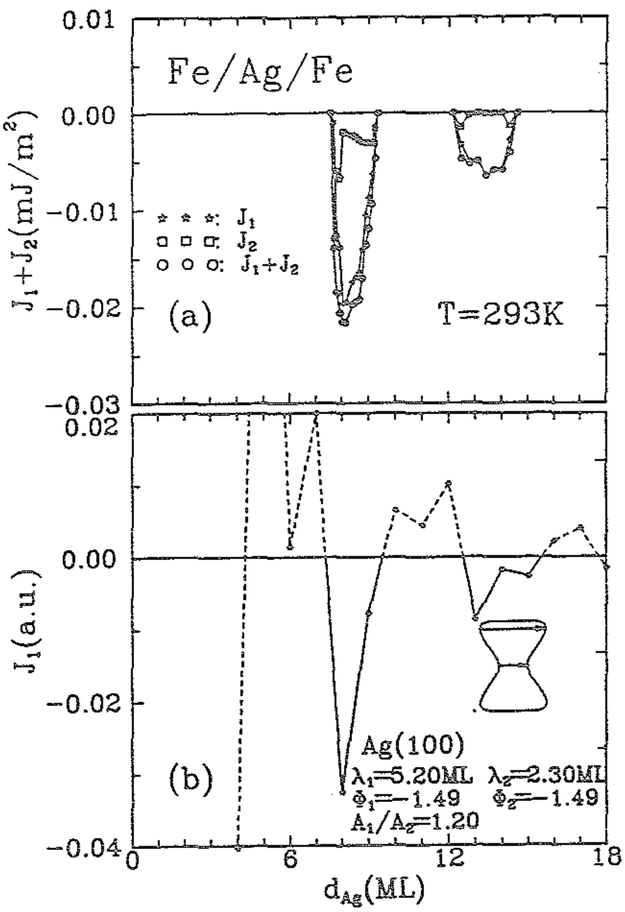

With equ.6.2 which is based on the RKKY interaction the oscillatory coupling with noble metal spacers can be simply reconstructed. It is clear that interlayer coupling can be employed for an investigation of electronic properties of the interlayer materials. However, so far only the oscillation periods can be used for a determination of the calipers at the Fermi surface in the direction perpendicular to the film plane. A more detailed theory based on the Friedel-Anderson theory of localized moments[6.10] has qualitatively shown that the coupling strengths and phases of the oscillations depend both on the Fermi surface characteristics of the interlayer material and the interaction between the interlayer and the magnetic layers. Another spin model theory of oscillatory coupling based on a simple cubic tight-binding band structure[6.11] has shown that the amplitudes of the oscillations depend on the curvature of the Fermi surface at its extremal points and the temperature dependence of the exchange coupling is determined by the velocity of carriers at these extremal points. For a quantitative evaluation of the phases and amplitudes a good theoretical background is still missing.

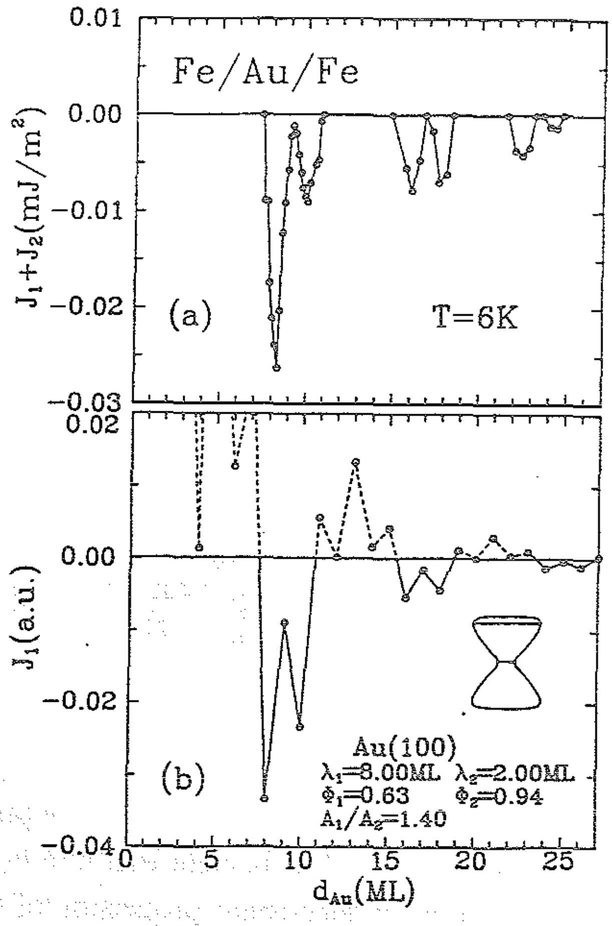

Fig.6.3. Thickness dependence of the exchange coupling in a Fe/Au/Fe (100) layered structure. (a) Experimental results taken from ref.[6.4]; (b) calculated oscillation on the basis of equ.6.1 and 6.2 using the indicated parameters. Part with full lines can be compared with the experiment. The shape of the corresponding electronic bands (dog's bone orbit) and relevant calipers are given.

From the theory[6.1] the phases for the noble metal spacers are all the same, i.e. $\Phi_1=\pi$ and $\Phi_2=\pi/2$, while the fitting phases are quite different. It can be due to imperfections of the sample structures which are also reponsible for the fact that the short period oscillations in the experimental results for the Ag and

Cu spacer systems are undetectable. Nevertheless, the trend of the measured coupling strengths is consistent with the theoretical results which is demonstrated in tab.6.2.

Fig.6.4. Thickness dependence of the exchange coupling in a Fe/Cu/Fe (100) layered structure. (a) Experimental results taken from ref. [6.3,6.4]; (b) calculated oscillation on the basis of equ.6.1 and 6.2 using the indicated parameters. Part with full lines can be compared with the experiment. The shape of the corresponding electronic bands (dog's bone orbit) and relevant calipers are given.

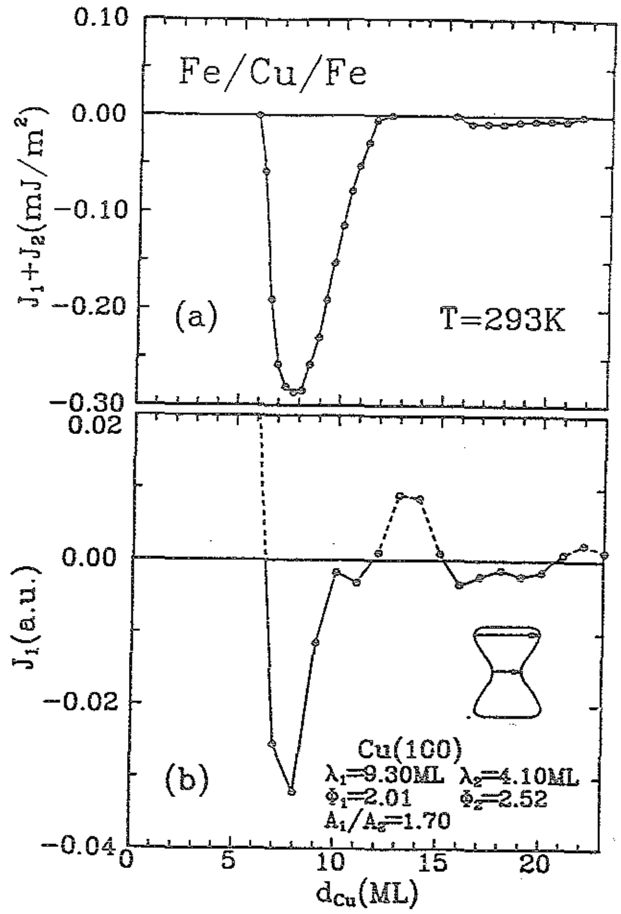

Figure 6.2(a) includes also a separation of the total coupling in the Fe/Ag/Fe-system into the bilinear and biquadratic constributions. The biquadratic coupling acounts for about 20% of the total coupling amount in the first AFM peak and almost vanishes in the second AFM range except at the boundaries between FM and AFM ranges.

Tab.6.2 Experimental and theoretical amplitudes of the oscillations for noble metal spacer systems. The experimental values were taken from fig.6.2(a)-6.4(a) and the theoretical value was from reference [6.1]. It should be noted that the coupling was measured at 6K for the Au spacer system in fig.6.3(a), but all the coupling strengths in this table are at 293K.

Noble Metal Spacers	**Au (100)**	**Ag (100)**	**Cu (100)**
Experimental Amplitude (mJ/m²)	0.017	0.022	0.285
Theoretical Amplitude (a.u.)	0.18	0.37	0.43

Now the discussion switches to the exchange coupling with an interlayer of an $Au_{0.45}Cu_{0.55}$ alloy. Au and Cu possess solid solubility for any concentration ratio, but some particular ratios are characterized by well defined crystalline order. In thermal equilibrium the structure of the alloy $Au_{0.5}Cu_{0.5}$ is a fcc lattice with alternating layers of Au and Cu, but if the solid has been rapidly quenched from the melt state, there can also be a random distribution. This situation is expected for a thin layer structure because they are condensed from the vapour state. The $Au_{0.45}Cu_{0.55}$ interlayer was prepared by e gun-evaporatation using an ingot with appropriate composition. The actual composition was determined by means of AES. This alloy is near a 1:1 Au-Cu composition and would be expected to have an ordered structure in thermal equilibrium.

Fig.6.5 shows the exchange coupling across the $Au_{0.45}Cu_{0.55}$ alloy as grown and after annealing. There is a drastic increase of the coupling after annealing. This change is due to the fact that the structure of this alloy goes from a disordered to a strongly ordered phase. These results suggest that the crystallinity of the interlayer plays a very important role in the strength of the coupling. Many controversial results on the coupling strength reported in literature might be due to this fact. Exchange coupling with interlayers of $Au_{1-x}Cu_x$ alloys with various x has been previously investigated[6.3,6.4]. This investigation indicates that the phases of the oscillations change with the composition x whereas the short periods do not change. The long periods decrease as the composition x increases. It is clear that the oscillatory coupling across the noble metal spacers can be ultilized to construct the Fermi surfaces of Au-Cu alloys with the help of the measured oscillation periods, phases and coupling strengths. Therefore it can be used as a method to obtain information on Fermi surfaces in a similar way as with the usual de Haas-van Alphen effect, but only that the latter seems to be more sensitive to structural imperfections. More details about the annealing investigation of the coupling with Ag, Cu and the Au-Cu alloy interlayers will be presented in the next chapter.

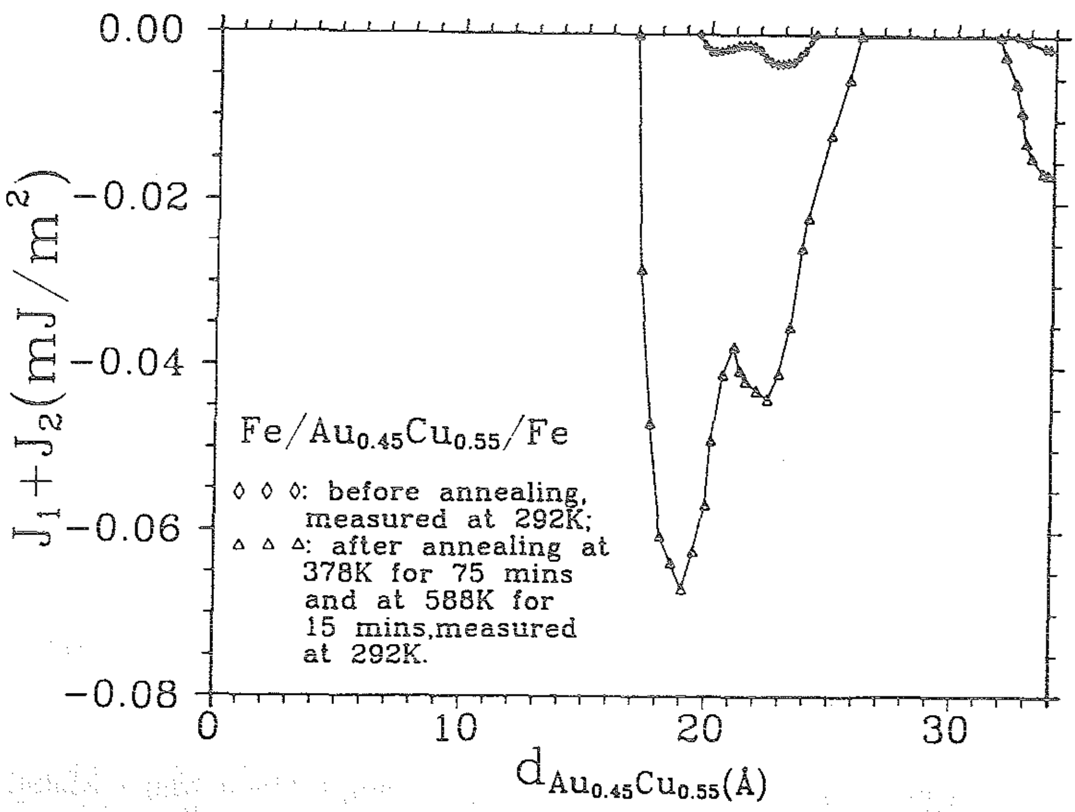

Fig.6.5 Magnetic interlayer coupling between iron layers across an $Au_{0.45}Cu_{0.55}$ alloy interlayer as-grown and after annealing with indicated conditions.

6.4 Conclusion

The magnetic exchange coupling between two iron layers separated by noble metal interlayers has been investigated. The two period oscillations in the exchange coupling can be reproduced by simply adding two sin-functions based on the Ruderman-Kittel-Kasuya-Yosida type theory. It has been confirmed in the case of the noble metals, Au, Ag and Cu, that the oscillatory periods depend on the extremal distances in the Fermi surfaces of the interlayer elements and the coupling strengths and phases are also given by the characteristics of the Fermi surface of the spacer. The interlayer coupling, therefore, can be used as a probe to determine the Fermi surface, especially in the case of alloys complementary to the de Haas-van Alphen effect.

6.5 References

[6.1] P.Bruno and C.Chappert, Phys. Rev. Lett. 67 (1991) 1602; 67(E) (1991) 2592.

[6.2] M.D. Stiles, "Exchange Coupling in Magnetic Heterostructures", to be published.

[6.3] Q.Leng, V.Cros, R.Schäfer, A.Fuß, P.Grünberg, W.Zinn, J. Magn. Magn. Mater. 126 (1993) 367-373.

[6.4] A.Fuß, S.Demokritov, P.Grünberg, W.Zinn, J. Magn. Magn. Mater. 103 (1992) L221; A.Fuß, J.A.Wolf, P.Grünberg, Physica Scripta T45 (1992) 95 and A. Fuß, Dissertation, University of Cologne (1993), and Jül-2740, rpts, KFA Research Center Jülich, March 1993.

[6.5] John.Unguris, Daniel T.Pierce, Robert J.Celotta and Joseph A.Stroscio, on "Magnetism and Structure in Systems of Reduced Dimension", (1992) Cargese,to be published in the NATO ASI series.

[6.6] Z.Celinski, B.Heinrich, J.F.Cochran, to be published in J. Appl. Phys.

[6.7] J.Unguris, R.J.Celotta, D.Pierce, submitted.

[6.8] W.R.Bennet, W.Schwarzacher, W.F.Egelhoff, Phys. Rev. Lett. 25 (1990) 3169.

[6.9] M.T.Johnson, S.T.Purcell, N.W.E.Mc Gee, R.Coehoorn, J.an de Stegge, W.Hoving, Phys. Rev. Lett. 68 (1992) 2688.

[6.10] P.Bruno, J. Magn. Magn. Mater. 116 (1992) L13-L17.

[6.11] D.M.Edwards, J.Mathon, R.B.Muniz and M.S.Phan, J. Phys. :Condens. Matter 3 (1991) 4941-4958.

7 Annealing Investigation of the Interlayer Coupling in Fe/X/Fe -(001) Systems

With 15 Figures

7.1 X=Cr and Cr/Ag/Cr

The exchange coupling in Fe/Cr/Fe sandwiches as presented in chapter 5 is thermally reversible up to 700K. This can be observed by Brillouin light scattering from spinwaves as shown in fig.7.1. There are no observable changes in the coupling by annealing for a rather long time.

For the Cr spacer system, the interlayer coupling in as-grown structures is thermally stable. On the other hand the preparation conditions, such as substrate temperature T_s, deposition rate V_r and annealing etc. have a large effect on the coupling. The effects resulting from T_s and V_r have been shown in section 5.2 in this thesis, and the other one resulting from annealing during sample preparation is indicated in fig.7.2. This figure shows the thickness dependence of the normalised saturation field in two sandwiches, i.e. sample #1: Fe(100Å)/Cr(0-23Å)/Fe(100Å) and sample #2: Fe(50Å)/Cr(0-22Å)/Fe(50Å). Both samples were prepared under the same conditions,

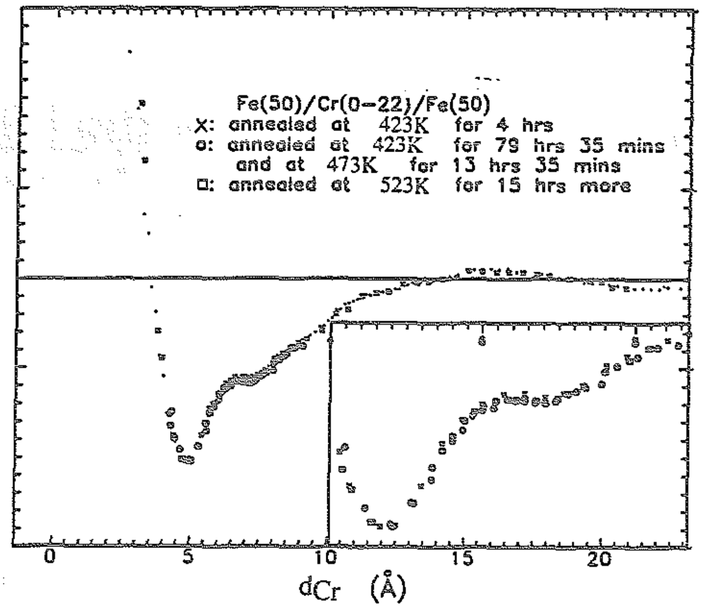

Fig.7.1 Interlayer magnetic coupling as a function of the interlayer thickness d_{Cr} in sample #2: Fe(50Å)/Cr(0-22Å)/Fe(50Å), evaluated from BLS spectra after annealing. The inserted picture shows the fine structure of the coupling in the region of d_{Cr}=4 - 9Å.

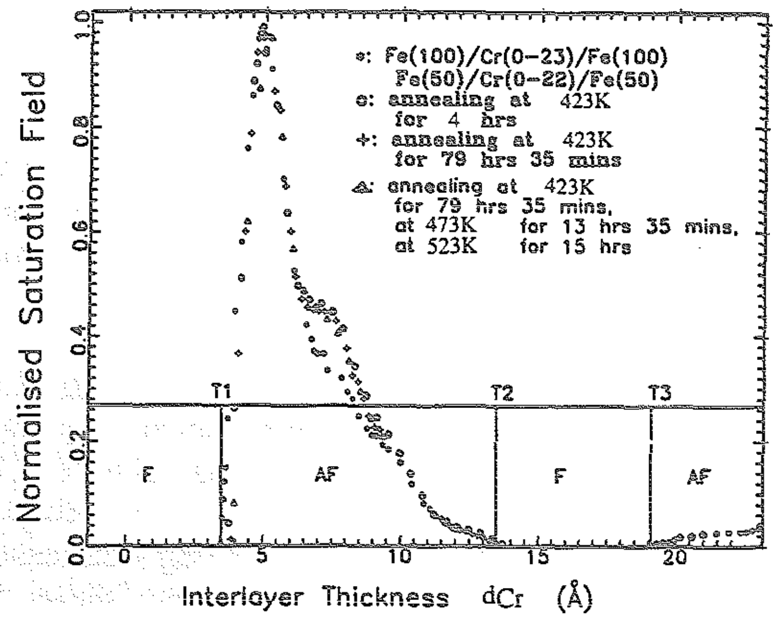

Fig.7.2 The normalised saturation field versus the interlayer thickness d_{Cr} in sample #1: Fe(100Å)/Cr(0-23Å)/Fe(100Å) (*) and sample #2: Fe(50Å)/Cr(0-22Å)/Fe(50Å), measured by MOKE as grown and after annealing under the indicated conditions. The circle tokens (o) indicate the coupling in sample #2 as grown.

T_s=293K and V_r=0.1~0.2 Å/sec, except that the sample #2 was annealed at 423K for 4 hours just after deposition of the Cr wedge and before evaporation of the second Fe layer. And both structures develop the long period oscillations in the coupling. In the figure, star (*) tokens show the results for sample #1, measured at RT without heat treatment; circles (o) show the results of the as grown sample #2 with four hour annealing at 423K during its preparation; crosses (+) and triangles (Δ) show the coupling in sample #2 with heat treatment after the sample fabrication. It can be clearly seen that there is a difference between the samples only on the shoulder of the first antiferromagnetic coupling range, in the region where a further AF coupling peak is expected by improving the layered structure. However, there are no differences to be observed within the experimental error by annealing after the sample preparation. This experiment confirms once more the fact that the coupling in the doubled magnetic layers is sensitive to the preparation conditions, but is thermally stable after preparation unless the sturucture is destroyed.

It is interesting to observe the magnetic behavior in the magnetic layered systems directly on the GaAs substrate without the buffer layer. For this purpose, the giant magnetoresistance (GMR) has been investigated on a multilayer structure of Fe(50Å)/Cr(6Å)/Fe(27Å)/Cr(6Å)/Fe(50Å)//GaAs-(001) by the four point method. This structure was directly deposited on the GaAs crystal. The results are demonstrated in fig.7.3, in which $R_{\uparrow\uparrow}$ is the resistance, as the magnetizations in the adjacent iron layers are parallel to each other, $R_{\uparrow\downarrow}$ the resistance as the magnetizations in the Fe films are in antiparallel alignment, μ_0H_s the saturation magnetic field where the magnetizations are forced into the direction of the external field. This structure shows strong AF coupling and a GMR effect with $\Delta R/R_{\uparrow\uparrow} \cong 5.8\%$ ($\Delta R = R_{\uparrow\downarrow} - R_{\uparrow\uparrow}$). The sample was annealed for 30 minutes for each shown annealing temperature. As the annealing temperature is below about 700K, the magnetoresistance and the saturation field do not have significant changes after annealing. As the structure is annealed over 700K, the field μ_0H_s and ΔR begin to decrease, but the resistance $R_{\uparrow\uparrow}$ increases. It means that the structure and Fe/Cr interfaces become worse after annealing. These results agrees well with that of the coupling investigations in the layered structures.

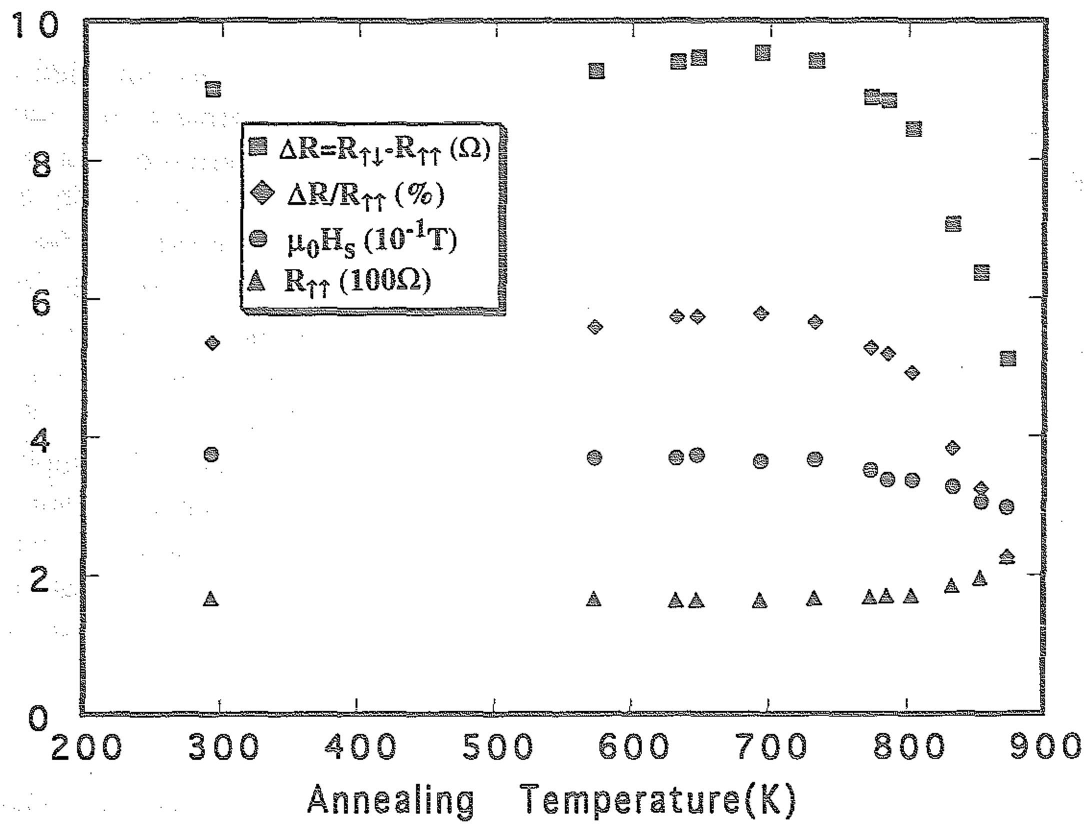

Fig.7.3 Magnetoresistance, $R_{\uparrow\uparrow}$, ΔR and the ratio $\Delta R/R_{\uparrow\uparrow}$, and the saturated field $\mu_0 H_s$ versus annealing temperature in Fe(50Å)/Cr(6Å)/Fe(27Å)/Cr(6Å)/Fe(50Å) //GaAs (001). Annealing time for each temperature is 30 minutes. The external magnetic field parallels to the electricity current direction and is along in-plane [110] direction.

Finally, the annealing result of interlayer coupling in the Fe/Cr/Fe structure with additional Ag layers inside the Cr interlayer is shown in fig.7.4. The added silver layer has the wedge geometry. Without the Ag the structure shows ferromagnetic coupling ($J_2 \geq 0$) and with more than 1Å-thick Ag it is 90° -type coupling ($J_2 < 0$). As seen above, the coupling in the samples with only pure Cr interlayers is quite stable after heat treatment, but the coupling in the case of Fe/Cr/Ag/Cr/Fe is greatly reduced after annealing at 573K for 30 minutes. This is a result of Ag diffusion into the Cr and the influence of the diffusion at the interfaces as discussed in section 5.5. The coupling after annealing shows a FM coupling region surrounded with 90° -type coupling at the position of d_{Ag}=5Å. This phenomenon may be due to some defect on the sample and formation of pin-holes after annealing. Therefore the FM area with the 90° coupling surrounding is the result of a ferromagnetic bridge though the defect.

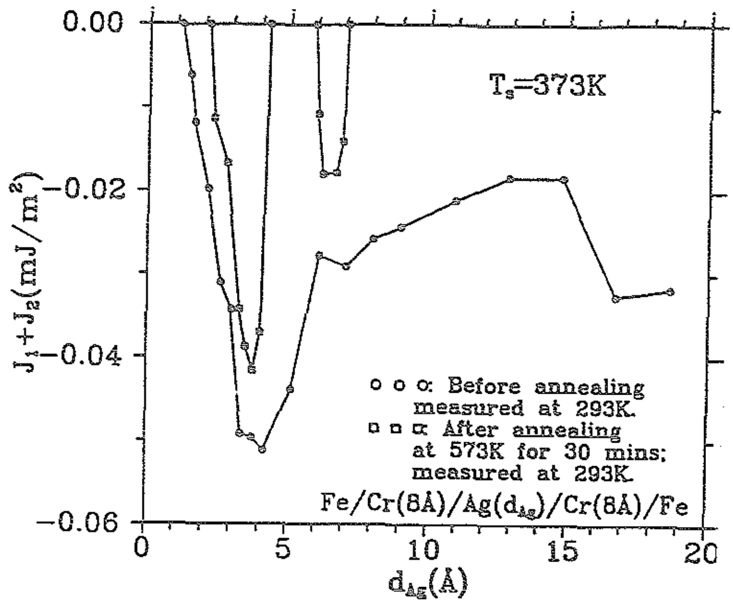

Fig.7.4 Interlayer exchange coupling as a function of d_{Ag} in Fe(50Å)/Cr(8Å)/Ag(0-20Å)/Cr(8Å)/Fe(50Å) system, measured before and after annealing with the quoted conditions. T_S is the substrate temperature.

7.2 X=Au-Cu alloys and Au/Cu superlattices

7.2.1 Introduction

This section presents the annealing investigations on the systems with Au-Cu alloy and Au/Cu superlattice interlayers. For the Cr interlayer systems, improvement of the structural order by heat treatment is in competition with the changes of interface quality, and both effects are difficult to distinguish. For the Au-Cu alloy systems it is well known for which compositions well ordered structures can be established below around 400°C.

Fig.7.5 shows the phase diagram for this system[7.1]. Au and Cu possess solid solubility for any composition. Some particular compositions are characterized by well defined crystalline order.

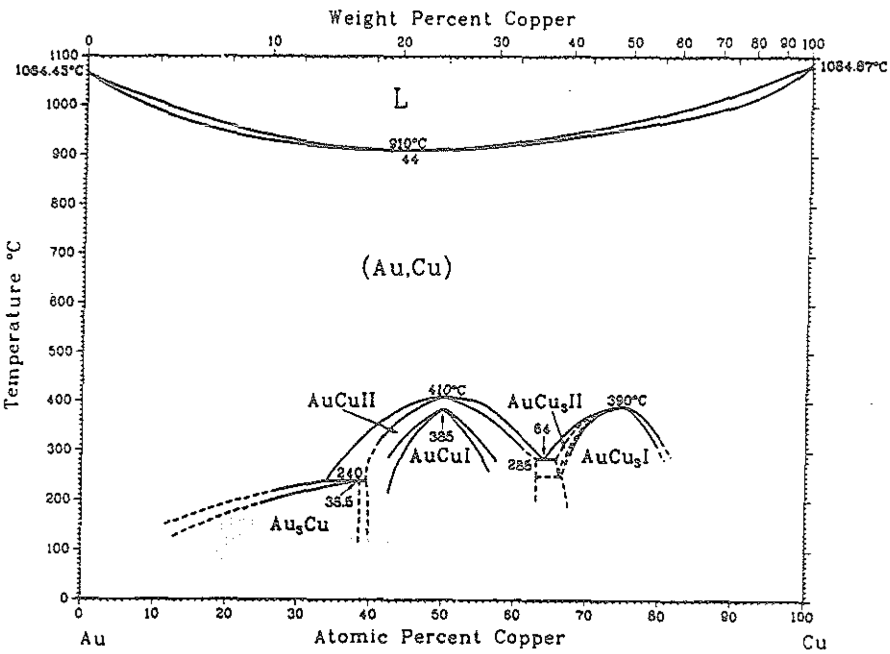

Fig.7.5 The phase diagram of Au-Cu system [after 7.1].

AuCu alloy: In thermal equilibrium the structure of alloy AuCu is a fcc lattice with alternating layers of Au and Cu. There are two ordered phases for this alloy. Below 385°C the tetragonal AuCu(I) phase forms and for small deviations from the 1:1 composition ratio the alloys form at lower temperatures. There is an order-order transformation in AuCu at a higher temperature, in which an orthorhombic AuCu(II) phase is established from the tetragonal AuCu(I) ordered phase. As the temperature is above 410°C, the orthorhombic AuCu(II) phase transforms to the disordered fcc phase.

$AuCu_3$ alloy: The $AuCu_3$ alloy is well known for its long-period superlattice structure. It can be obtained below 390°C and transforms to a disordered Au-Cu alloy at a higher temperature.

7.2.2 Annealing Effect of the Coupling in the X=$Au_{0.45}Cu_{0.55}$ Alloy System

Magnetic coupling between iron layers across an $Au_{0.45}Cu_{0.55}$ alloy interlayer has been studied with a wedged geometry interlayer. The sample was evaporated with V_r=0.1~0.2Å/sec, T_s=293K for the first iron layer and the alloy interlayer, and T_s=373K for the second iron layer[7.2]. Annealing was performed in vacuum. The coupling was observed by in situ MOKE during the

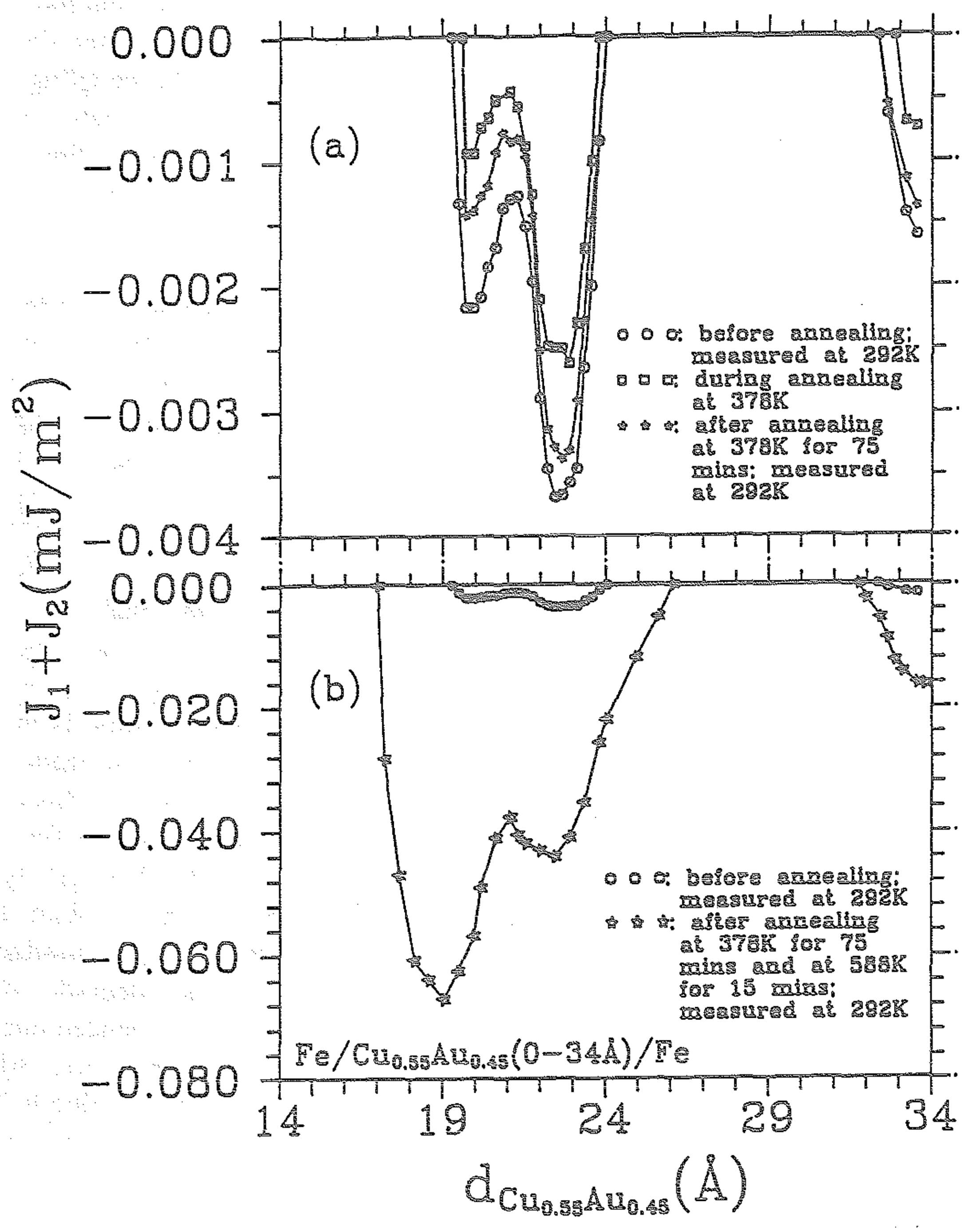

Fig.7.6 The exchange coupling as a function of the thickness of the $Cu_{0.55}Au_{0.45}$ alloy interlayer in the Fe(10Å)/$Cu_{0.55}Au_{0.45}$(0-34Å)/Fe(10Å) structure as grown, and during and after annealing under the quoted conditions.

annealing. Fig.7.6 shows the coupling versus thickness of the alloy interlayer. It shows two oscillation periods. The long period is about 7.6 ML and the short period is around 2ML. From fig.7.6(a), it is clearly seen that the coupling is reduced during annealing at 378K, while after annealing at this temperature for 75 minutes the interlayer coupling is still weaker than that before annealing. In fig.7.6(b) a drastic increase of the coupling has been observed after annealing at 588K for 15 minutes or more.

The $Au_{0.45}Cu_{0.55}$ alloy is near a 1:1 concentration ratio. In principle, it can form ordered structure. However, the sandwich structure of Fe/$Au_{0.45}Cu_{0.55}$/Fe was evaporated at room temperature (RT). Thus, the as-grown state might not have the ordered structure. Normally, in this doubled magnetic layers annealing results in two effects. One is the interdiffusion at the interfaces between the iron layers and the alloy interlayer and the another is the change of the layered structure. Both effects depend strongly on annealing temperature and time. The results shown in fig.7.6(a) indicates that the annealing temperature of 378K is not high enough to improve the structures of the films, but the quality of the interfaces in the sandwich become worse than that before the annealing due to diffusion. This may be the reason why the coupling intensities decrease after annealing at this temperature. As indicated in fig.7.6(b), the situation is quite different as it is annealed at a higher temperature. After annealing at 588K for 15 more minutes, the coupling is about 30 times as large as that before this heat treatment. According to these diagram of the Au-Cu system shown in fig.7.5, this temperature should be high enough to form an ordered fcc AuCu(I) -type alloy, i.e. the phase with tetragonal order. For the interlayer with the $Au_{0.45}Cu_{0.55}$ composition the situation is similar. Although the interfaces between Fe and the $Au_{0.45}Cu_{0.55}$ alloy layer would further degrade after annealing at elevated temperatures, the coupling is still greatly enhanced due to much improvement of the interlayer structure at this temperature. After annealing above 680K the coupling decreases and then disappears due to the transformation from the ordered structure to fcc disordered phase according to Au-Cu phase diagram.

7.2.3 Annealing Effect of the Coupling in the X=$AuCu_3$ Alloy System

A similar effect as described in the previous section has been observed in the Fe/$AuCu_3$/Fe system. The results of interlayer coupling as a function of the

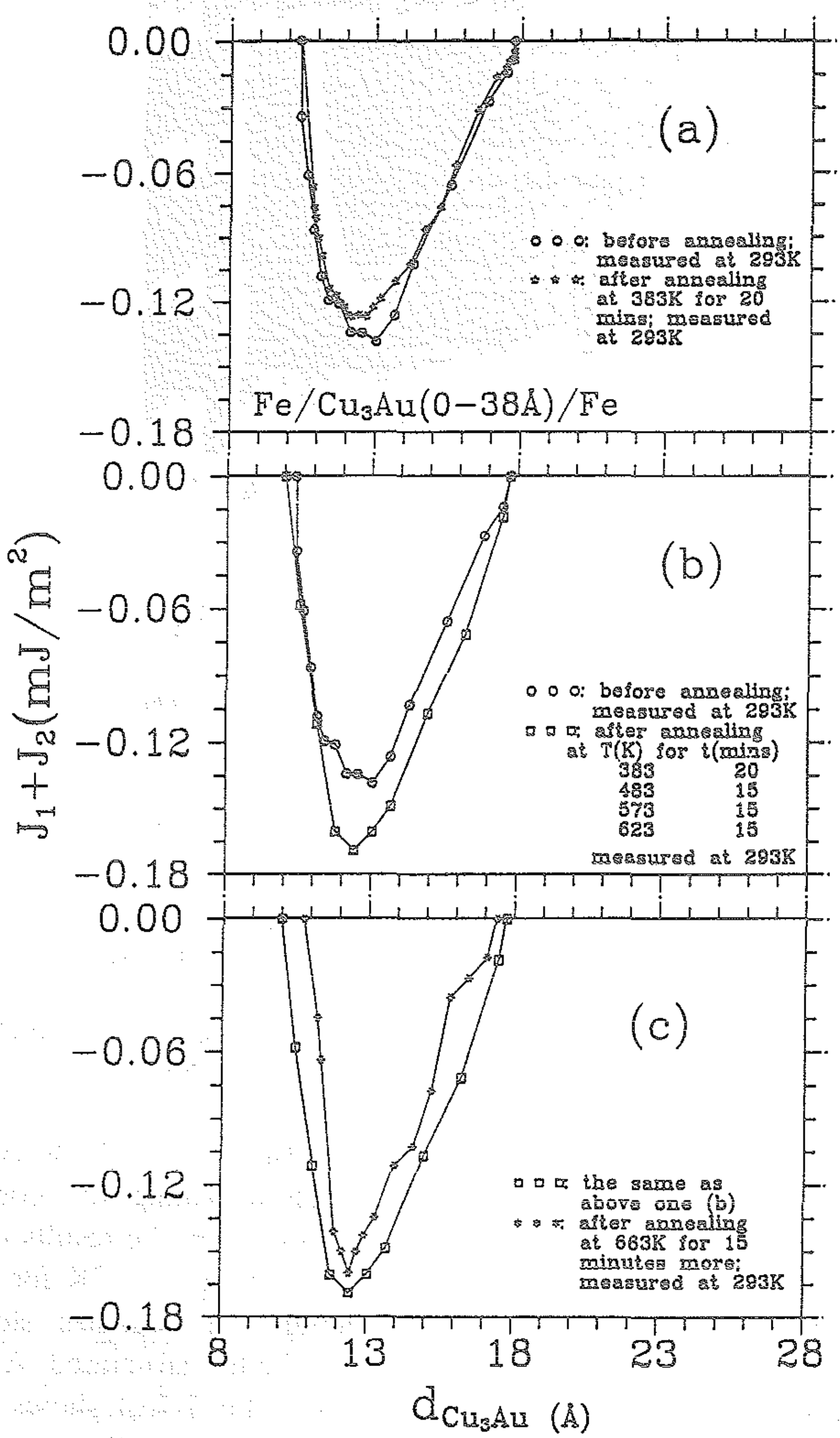

Fig.7.7 The exchange coupling as a function of the thickness of Cu_3Au alloy interlayer in Fe(20Å)/Cu_3Au(0-38Å)/Fe(20Å) structure as grown and after annealing under the quoted conditions.

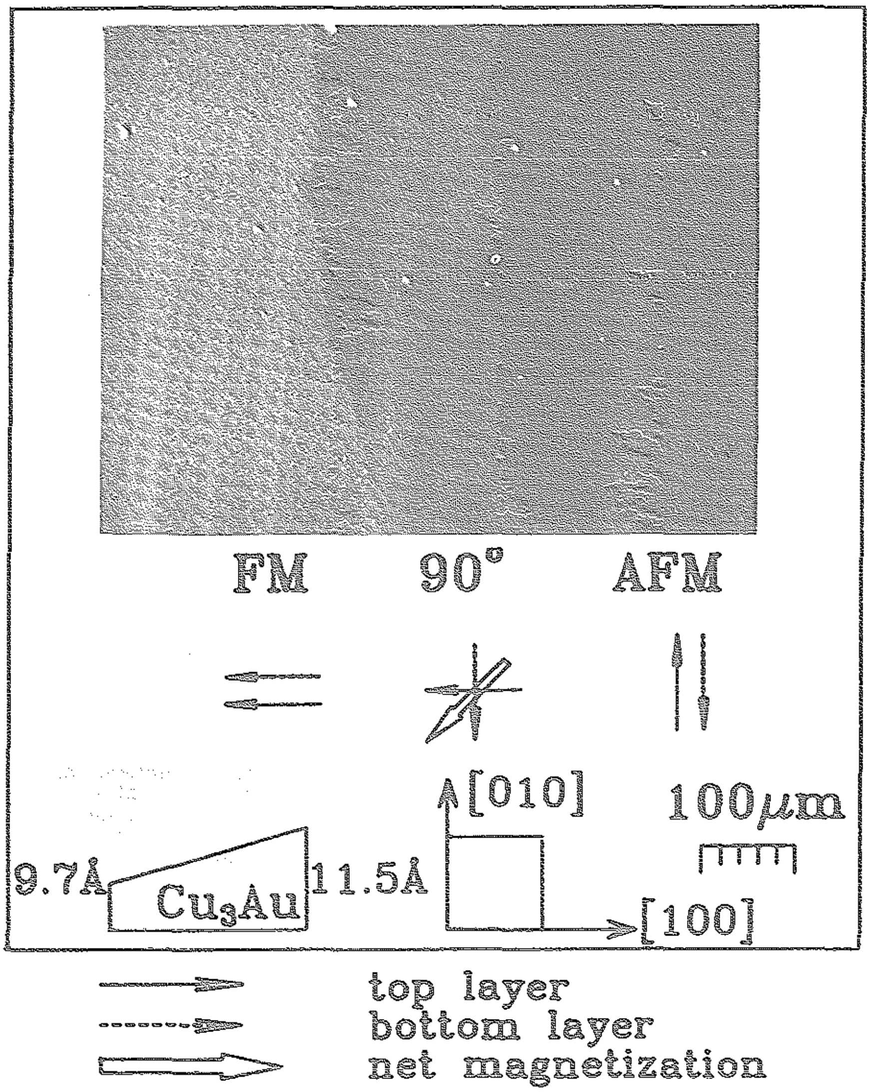

Fig.7.8 The domain configuration taken by Kerr microscope in Fe/Cu_3Au/Fe layered structure in the region of $d_{Cu_{0.55}Au_{0.45}}$=9.7 - 11.5Å.

interlayer thickness in this system are shown in fig.7.7. In order to conveniently compare the coupling before and after each annealing the corresponding coupling curves are set in one panel of the figure. From the results in fig.7.7(a) it is found that the exchange coupling after annealing at 383K for 20 minutes becomes weaker than that before annealing, but becomes stonger after annealing at a higher temperature where a better structured $AuCu_3$ alloy interlayer may form as indicated in fig.7.7(b). Fig.7.7(c) shows the results obtained after annealing at higher temperature. The coupling decreases after this heat treatment comparing with that shown in fig.7.7(b). The coupling becomes weaker after annealing at 663K where is near the critical boundary of the order-disorder phase transformation in the diagram of the Au-Cu system.

Therefore, at this temperature the structures of the layers as well as the Fe/$AuCu_3$ interfaces degrade and make the coupling to disappear above about 673K.

Fig.7.8 gives the domain configuration taken with a Kerr microscope from this structure in the region of d_{AuCu3}=9.7-11.5Å. There is a narrow 90°-type coupling zone between the FM and AFM coupling ranges. The interpretation of the orientations of the magnetizations is indicated by means of arrows.

7.2.4 Annealing Effect of the Coupling in the X=Au/Cu Superlattice System

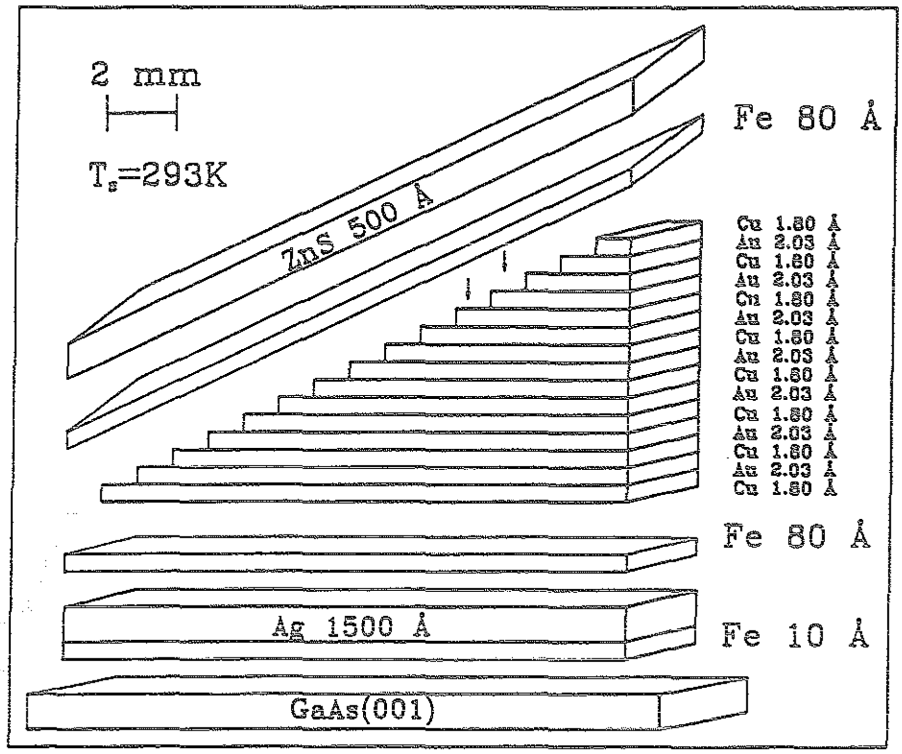

Fig.7.9 The sample geometry with a special interlayer for annealing research.

This subsection presents the exchange coupling between iron films separated by a superlattice interlayer of Au/Cu as grown and after annealing.

The sample was fabricated following the same procedure as that for the sandwiches of Cr interlayers, with substrate temperature T_s=RT and deposition rate V_r=0.1Å/sec. The geometry of the interlayer is shown in fig.7.9. It consists of alternating monoatomic layers of Cu and Au. Each additional atomic layer was deposited on the previous layer by moving the substrate at same time behind a diaphragm by 1 mm during evaporation. Both iron films are 80Å thick. The studied sandwich was fabricated on an Ag buffer layer. The effective length of GaAs(001) substrate is 16 mm. A 10Å Fe film is used as seed layer directly on the GaAs.

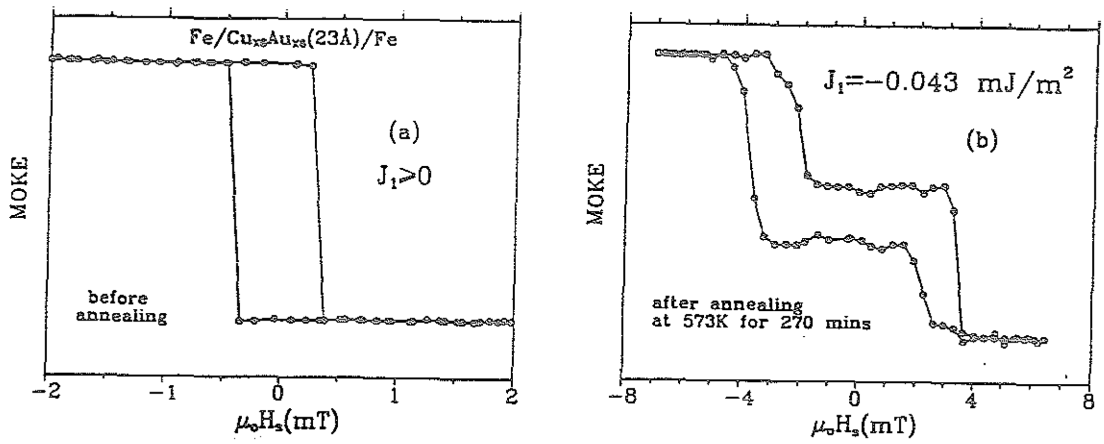

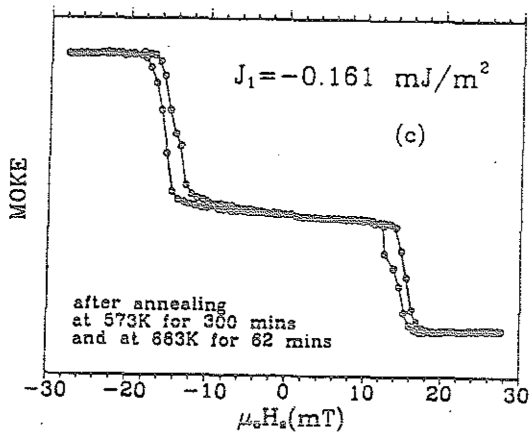

Fig.7.10 The hysteresis loops in a Fe/(Cu/Au)$_{\times 6}$/Fe layered structure, measured by MOKE before and after annealing.

The annealing investigations were carried out in a vacuum with a background pressure of 4×10^{-4} Pa. The magnetic exchange coupling was monitored by MOKE during annealing. Before the heat treatment this sample show ferromagnetic coupling in the whole region at RT and 6K. After annealing at appropriate temperatures antiferromagnetic coupling has been observed in the positions which are indicated by arrows in fig.7.9. These two positions coorespond to interlayers of $(Cu/Au)_{\times 6}$ and $(Cu/Au)_{\times 5}/Cu$, respectively. Fig.7.10 displays the hysteresis loops before and after annealing at the position with the $(Cu/Au)_{\times 6}$ interlayer. The as-grown structure at this position shows FM coupling, i.e. $J_1 \geq 0$, as seen from the typical ferromagnetic M(H) curve in fig.7.10(a). Fig.7.10(b) shows the typical hysteresis of AFM coupling with a plateau of $M \cong 0$ due to antialignment of the magnetizations in the adjacent iron layers after annealing at 573K for 270 minutes. After the sample is annealed at 573K for 300 minutes and at 663K for 62 minutes, the AFM coupling (fig.7.10c) is approximately three times stronger than that in fig.7.10(b).

This is a good example of the layered structure which shows negative coupling after heat treatment in the doubled magnetic layers with a Au/Cu interlayer, which is positive coupling without the heat treatment. Considering the phase diagram of the Au-Cu system, it is clear that an interlayer of alternative Cu and Au elements will be well alloyed by heating to 663K and forms there a well ordered structure.

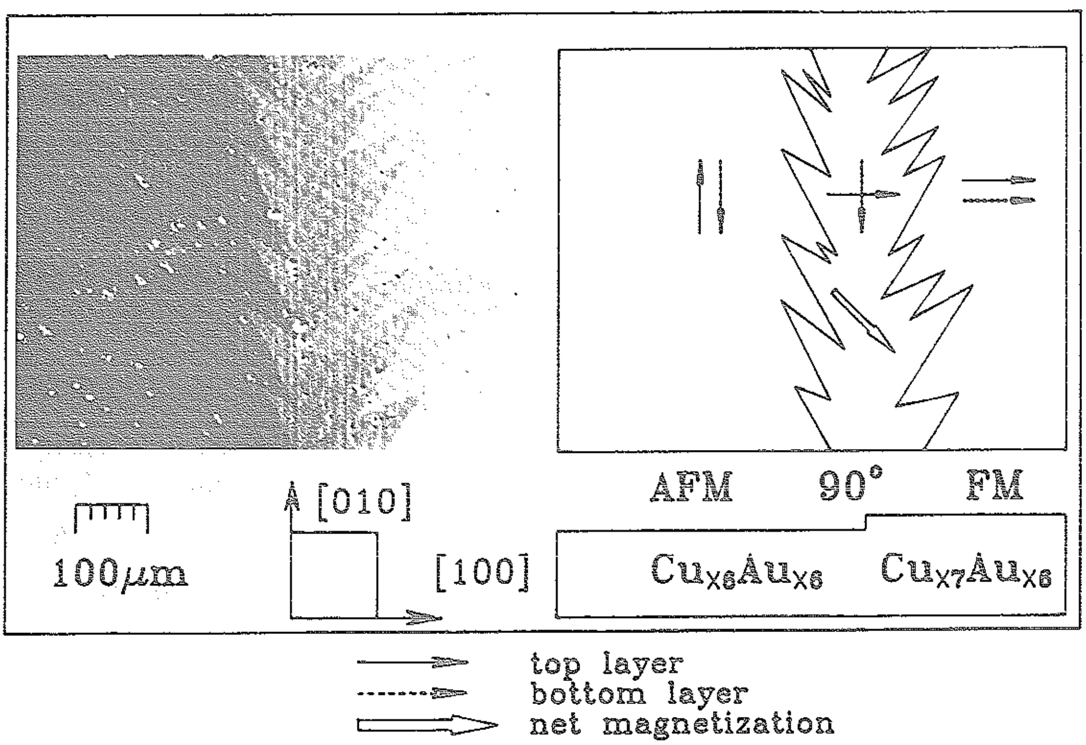

Fig.7.11 The domain pattern (left bild) taken by Kerr microscope in the region of $Fe/(Cu/Au)_{\times 6}/Fe$ and $Fe/(Cu/Au)_{\times 6}/Cu/Fe$. The right picture is the interpretation of the orientations of the magnetizations in iron layers.

The domain pattern obtained by Kerr microscopy in the range of the $(Cu/Au)_{\times6}$ and $(Cu/Au)_{\times6}/Cu$ interlayers in the sandwich structure is given in fig.7.11. Zig-zag domain walls have been observed between the FM- and 90°-type coupling areas and between 90°- and AFM - type coupling areas. The domain walls are orientated in a stray field free way. The interpretation of the orientations of the magnetizations are given with arrows

The negative coupling between Fe films across $(Cu/Au)_{\times5}/Cu$ interlayers after annealing has been investigated from 6K to RT. The temperature dependence of the coupling J_1 is displayed in fig.7.12. It shows linear behviour like normal bilinear exchange coupling.

Fig.7.12 Temperature dependence of the interlayer magnetic coupling in $Fe/(Cu/Au)_{\times5}/Cu/Fe$ structure after annealing.

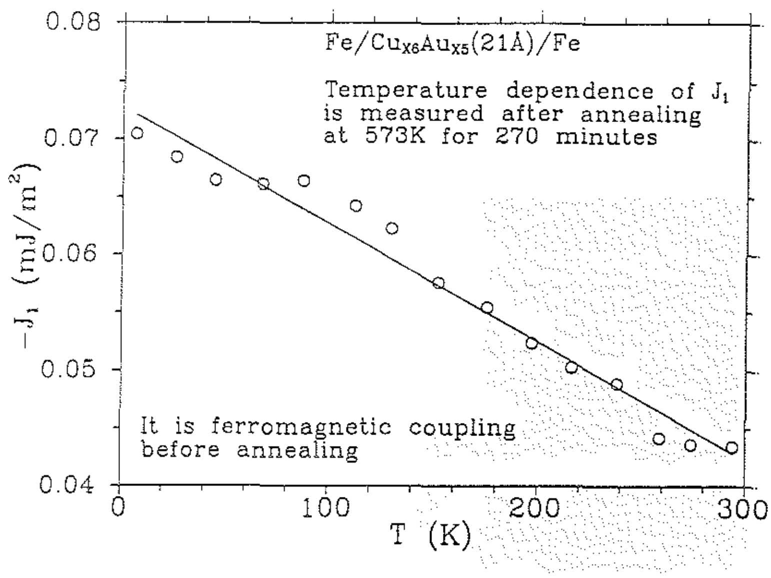

When $(Cu/Au)_{\times6}$ forms an alloy by annealing, it is of near a 1:1 atomic concentration ratio. The thickness of the $(Cu/Au)_{\times6}$ is around 23Å. The coupling with this interlayer can compare with that shown in fig.7.6 with an $Au_{0.45}Cu_{0.55}$ alloy interlayer. There is just one AFM peak around $d_{Au0.45Cu0.55} \cong$ 23Å.

7.2.5 Conclusion

In this section annealing investigations of the interlayer exchange coupling between iron layers spaced by Au-Cu alloy interlayers has been presented. Both interface- and volume-structure effects have been observed. The negative interlayer coupling could be greatly enhanced by annealing due to the improvement of the crystal quality of the interlayer. Therefore, this research suggests that the crystallinity of the interlayer should play a very important role in the coupling intensity.

Probably for the observed effects the good match of the lattices of the iron layers and the interlayer materials are important. Also because of the possibility of interdiffusion at the interfaces in the studied sandwiches clear results due to heat treatment are only expected if the well ordered structures of the interlayer materials are easy to be achieved at temperatures as low as possible, where the influence of diffusion at the interfaces is not large enough to destroy the coupling. The Au-Cu alloy is just a good choice for this kind of investigation.

The coupling strength can be reduced by the influence of the interdiffusion between the magnetic layers and the interlayers. As the structure is well improved, the coupling strength will largely increase, and at the same time the diffusion at the interfaces is still working and reduces the coupling intensity. However, according to the observation, the former effect is much larger than the latter one at a temperature where an ordered alloy phase will form in Au-Cu alloy spacers of proper composition.

Not only the AFM coupling can be enhanced by annealing, but also for the first time it is observed that the AFM coupling is obtained by heat treatment starting from the FM coupled state.

The annealing investigation were also carried out in pure Au, Cu or Ag spacer systems by heat treatment at various temperatures, but the AFM coupling has not been observed, if the as-grown structures showed only FM coupling. This is the fact that the interface effect is not smaller than the structure effect as annealing at an elevated temperature.

7.3 X=Cu, Ag and Al

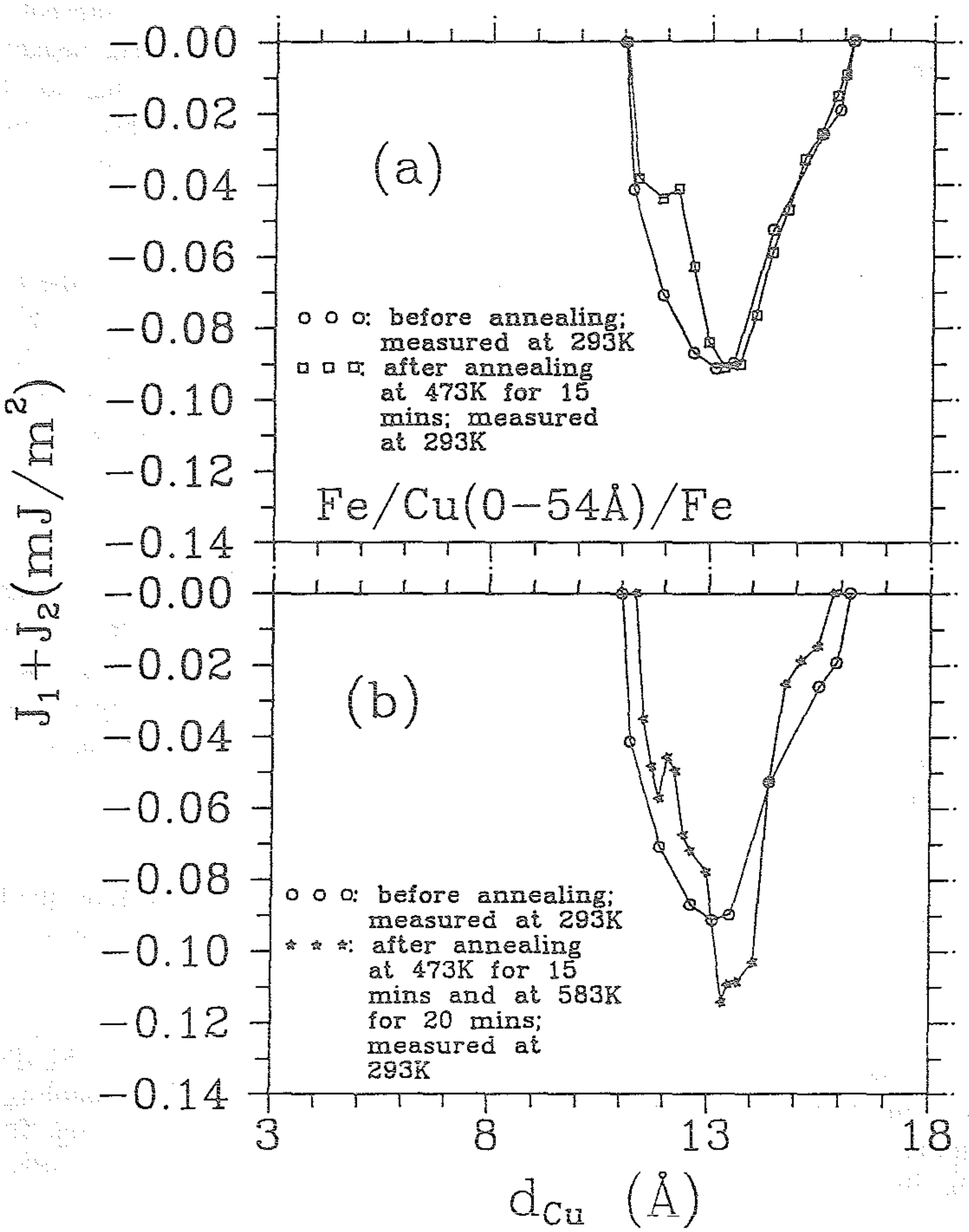

Fig.7.13 The interlayer coupling versus the interlayer thickness d_{Cu} in Fe/Cu layered structure, measured as grown and after annealing under the indicated conditions.

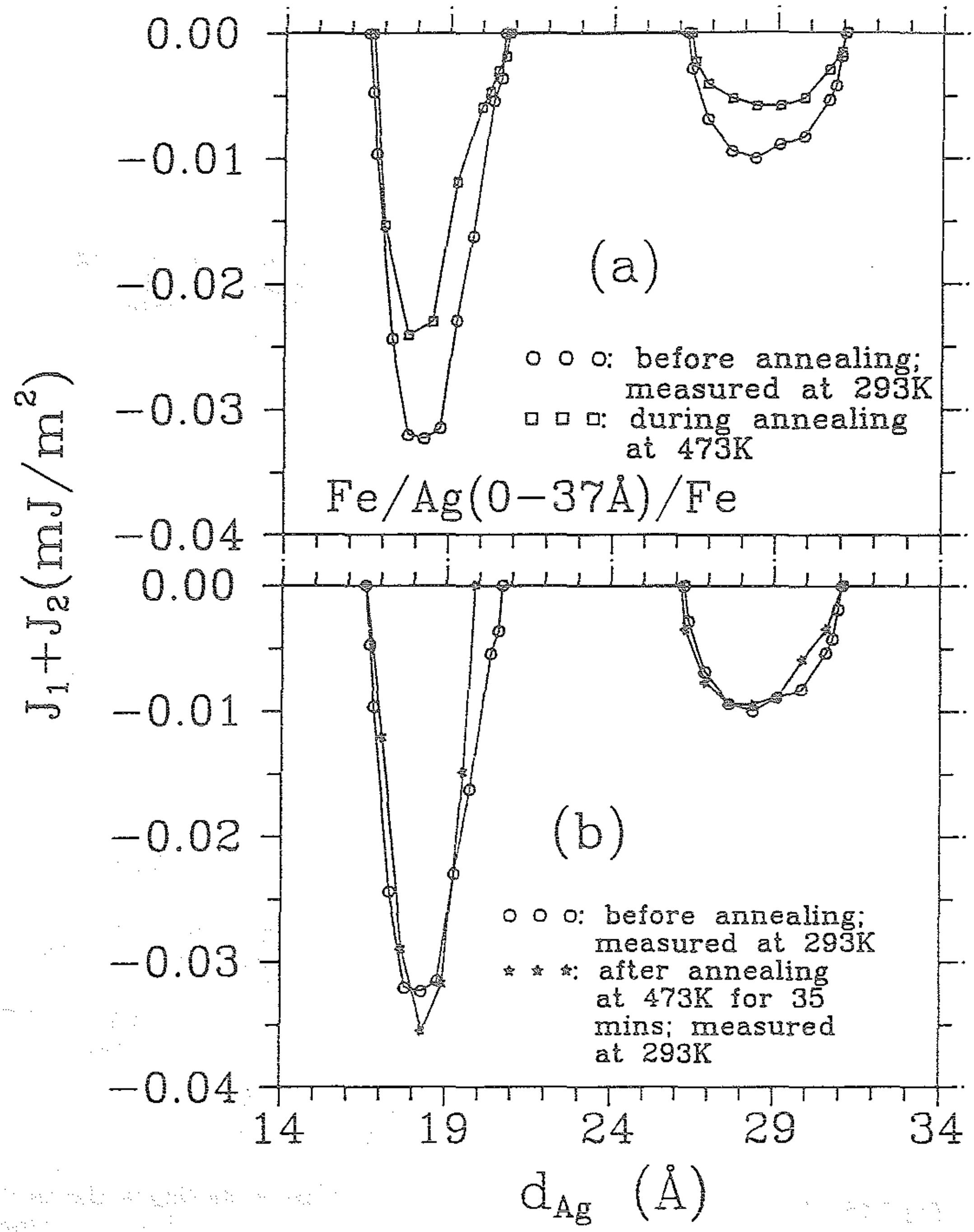

Fig.7.14 The interlayer coupling versus the interlayer thickness d_{Ag} in Fe/Ag layered structure, measured as grown, and during and after annealing under the indicated conditions.

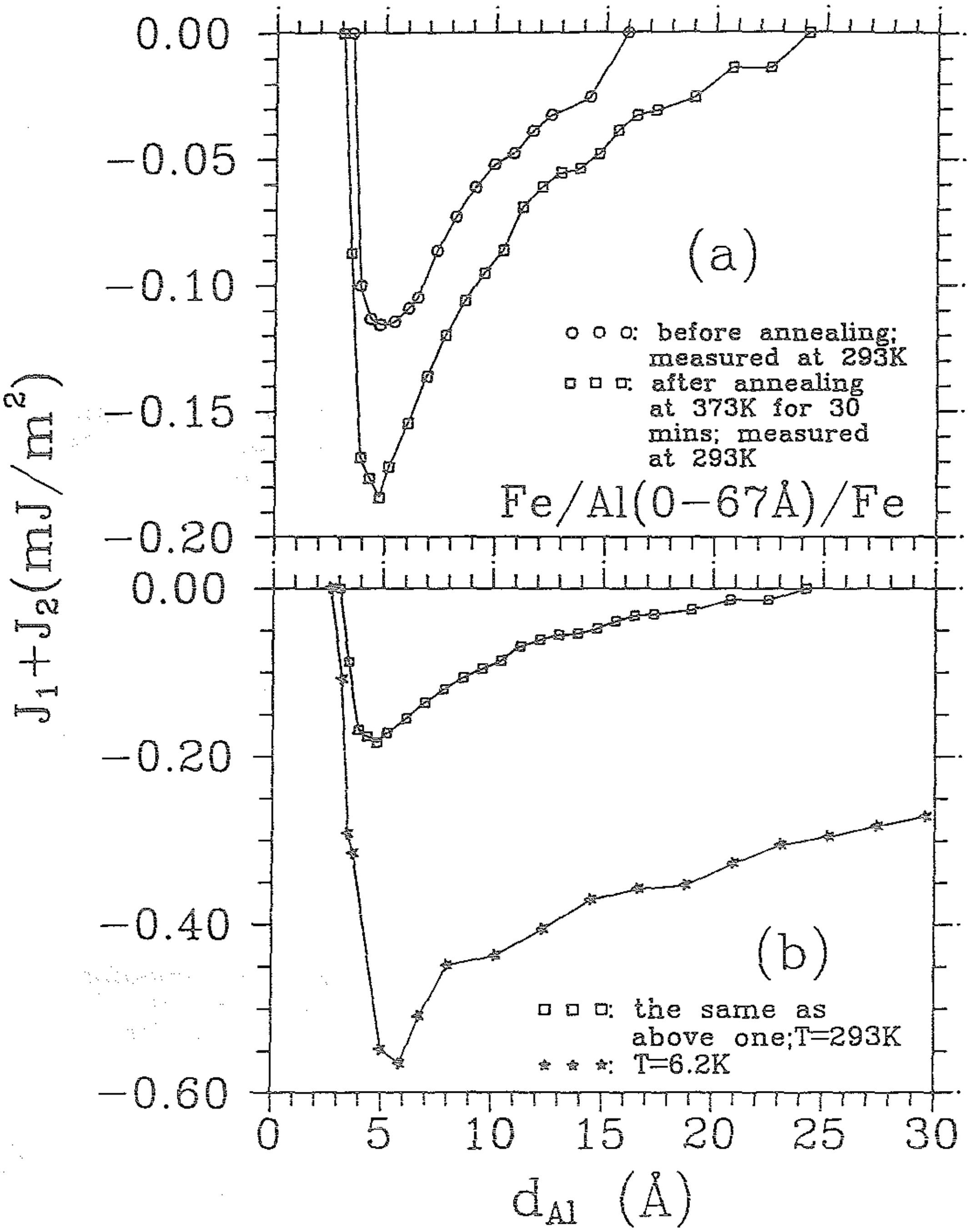

Fig.7.15 The interlayer coupling versus the interlayer thickness d_{Al} in a Fe/Al layered structure, measured as grown and after annealing under the indicated conditions.

Fig.7.13 displays the Cu-thickness dependence of the interlayer coupling in Fe/Cu/Fe (001) structures. In this sample 90°-type coupling is dominant. The coupling strength did not increase until the annealing temperature reached 583K, but after heat treatment the 90° coupling region became narrower. This is probably due to diffusion at the interfaces of Fe/Cu. Comparing the coupling after annealing with that before annealing in both fig.7.13 (a) and (b), the changes of the coupling due to annealing are irregular from point to point. This may be the influence of inhomogeneity of the sandwich structure due to the lattice mismatch between bcc Fe and fcc Cu.

Fig.7.14 shows the coupling versus interlayer thicknesses of d_{Ag} as grown, and during and after annealing. The coupling as measured at the annealing temperature is reduced during annealing at 473K (fig.7.14a). However, the coupling measured at room temperature is the same as before(fig.7.14b). For annealing temperatures above 563K negative coupling disappears. The AES investigation indicates that under these conditions Ag diffused into iron layers seriously.

Fig.7.15 displays the coupling as a function of the Al interlayer thickness before and after annealing, measured at RT and at 6.2K. The 90°-type coupling is dominant in this sample. There is quite a large change after annealing only at 373K for 30 minutes as indicated in fig.7.15(a). Thus, for the Al spacer, the exchange coupling is very sensitive to the preparation temperature[7.2]. The well known strong temperature dependence of the coupling in the Fe/Al/Fe system has been also found in fig.7.15(b).

7.4 References

[7.1] H.Okamoto, D.J.Chakrabarti, D.E.Laughlin and T.B.Massalski, Bulletin of Alloy Phase Diagrams, Vol.8 No.5 (1987) 454-474.

[7.2] H.Fuß, Dissertation, University of Cologne (1993), and Jül-2740, Rpt., KFA Research Center Jülich, March 1993.

8 Conclusions

In this work the magnetic coupling between iron layers across nonmagnetic metal interlayers has been investigated by means of magneto-optic methods. The epitaxial growth and crystalline quality of the layered structures were controlled by RHEED, SPA-LEED and AES techniques.

Ultrathin Fe Films:

The magnetic properties, such as in plane anisotropy, effective magnetization and coercivity etc, as well as their thickness dependences and external field direction dependences have been investigated by means of BLS and MOKE for ultrathin iron films between 1.5 and 16 ML prepared at two different substrate temperatures.

Two magnetic phases are identified, the paramagnetic phase for 1.5ML and the ferromagnetic one for 2ML and thicker iron films. It is found that the g factor is 7% smaller in a 1.5ML film than that in the bulk. A nearly linear thickness dependence of the coercive force in these films has been observed. The thickness dependence of the bulk in-plane anisotropy shows similar behavior as that of the magnetization, but with a delay in thickness. No perpendicular surface magnetic anisotropy has been observed at RT in the samples, which may be related to the nearly perfect in-plane lattice matching between the sandwiched Fe layer and the Ag cover and substrate layers.

The observed 4-fold anisotropy in ultrathin Fe films, the observed narrow linewidth in BLS from 2 and 3 ML Fe films, and the small coercive forces (£0.4mT) demonstrate that the studied iron films are of high quality. The possible interdiffusion between interfaces of the iron film and the buffer or coating layer has been found in films prepared at an elevated temperature.

Interlayer Coupling in Cr Spacer Systems:

Investigation of epitaxial growth shows that the interlayer coupling is very sensitive to the preparation conditions. If the substrate temperature is too low, the sandwich structure will not have the quality to show the fine structure in the oscillations. If the T_S is too high, interdiffussion may take place at the Fe/Cr interfaces and attenuates the coupling strength. If evaporation is at a too high rate, the adatoms can not form a well ordered structure. Therefore, too fast growth can smooth the fine oscillations. Thus, to study the oscillatory coupling, the optimum may be reached with T_S=523K and V_r=0.1~0.2Å/sec.

The interlayer magnetic exchange coupling for both long and short period oscillations in Fe/Cr/Fe systems has been observed in situ by MOKE during annealing up to around 800K. It has been found that the oscillatory coupling for both cases is thermally stable up to 700K and can be observed until the sample structure is destroyed at temperatures beyond approximately 750K. A deviation in the range of extremely thin interlayers is contributed to the diffusion at the Fe/Cr interfaces . The biquadratic coupling is reduced faster than the bilinear one with increasing temperature.

Temperature dependences of both long and short period oscillatory coupling have been investigated from 6 to 700K. It has been found that the periods in the oscillations do not change in this temperature range. The bilinear coupling behaves in the way of linear temperature dependence. The biquadratic coupling behaves in very different ways. It is not always monotonically decreasing as temperature increases and can show maxima. If the thickness of the interlayer is very large, the biquadratic coupling shows a anomalous behavior. A common feature of the biquadratic coupling, on the other hand, is a strong temperature dependence.

For the Fe/Cr/Fe system in total three different periods in the oscillations are found to be related to certain distances in the Fermi-surface of Cr, as predicted by theories. The attenuations of the oscillation amplitudes in the exchange coupling follow d_{Cr}^{-n} -dependent power laws with n=1.03, 1.22, 1.80 and 2.08 for different samples. They are correlated with different nesting effects, where n=1 corresponds to the complete nesting and n=2 to the absence of nesting.

According to the investigation by means of CEMS, 3 at% Fe diffusing into the Cr interlayer is possible for the layered structures made with T_S_523K. The interdiffusion at Fe/Cr interfaces should be reponsible for the no phase-slip oscillations, because the diffusion of Fe into Cr would cause the transition of incommensurate- to commensurate spin density wave in the antiferromagnetic phase of Cr.

Introducing an Ag layer into the Cr interlayer in a Fe/Cr/Fe layered structure will increase the roughness at the interfaces and influence the structure of the Cr interlayer. With respect to the coupling in these structures, the role of the added Ag layer is to reduce the bilinear coupling intensity and at the same time to strengthen the biquadratic coupling. The interface roughness should be reponsible for the biquadratic coupling.

Interlayer Coupling in Noble Metal Systems:

The magnetic exchange coupling between two iron layers separated by noble metal interlayers has been investigated. The two period oscillations in the exchange coupling can be reproduced by simply adding two sin-functions based on the Ruderman-Kittel-Kasuya-Yosida type theory. It has been confirmed in the case of the noble metals, Au, Ag and Cu, that the oscillatory periods depend on the extremal distances in the Fermi surfaces of the interlayer elements and the coupling strengths and phases are also given by the characteristics of the Fermi surface of the spacer. The interlayer coupling, therefore, can be used as a probe to determine the Fermi surface, especially in the case of alloys complementary to the de Haas-van Alphen effect.

Influence of Annealing on Interlayer coupling:

Annealing investigations of the interlayer exchange coupling between iron layers spaced by Cr, Cr/Ag/Cr, AuCu, Au/Cu, Ag, Cu and Al interlayers has been performed.

Both interface- and volume-structure effects have been observed in Au-Cu alloy spacer systems. The negative interlayer coupling could be greatly enhanced by annealing due to the improvement of the crystal quality of the interlayer. Therefore, this research suggests that the crystallinity of the interlayer should play a very important role in the coupling intensity.

Probably for the observed effects the good match of the lattices of the iron layers and the interlayer materials are important. Also because of the possibility of interdiffusion at the interfaces clear results due to heat treatment are only expected if the well ordered structures of the interlayer materials are easy to be achieved at temperatures as low as possible, where the influence of diffusion at the interfaces is not large enough to destroy the coupling. The Au-Cu alloy is just a good choice for this kind of investigation.

The coupling strength can be reduced by the influence of the interdiffusion between the magnetic layers and the interlayers. As the structure is well improved, the coupling strength will largely increase, and at the same time the diffusion at the interfaces is still working and reduces the coupling intensity. However, according to the observation, the former effect is much larger than the latter one at a temperature where an ordered alloy phase will form in Au-Cu alloy spacers of proper composition.

Not only the AFM coupling can be enhanced by annealing, but also for the first time it is observed that the AFM coupling is obtained by heat treatment starting from the FM coupled state.

For pure Au, Cu or Ag spacer systems, however, the AFM coupling has not been observed by heat treatment at various temperatures, if the as-grown structures showed only FM coupling. This is the case where the interface effect is not smaller than the structure effect for annealing at an elevated temperature.

Finally, we may conclude that the oscillatory magnetic coupling between iron layers across nonmagnetic interlayers depends on both crystalline ordered structures of the interlayers and interfaces, but a smooth interface is not a necessary condition for an oscillatory coupling with short periods, while a well ordered crystalline interlayer should be reponsible for a fine oscillatory magnetic coupling. The biquadratic coupling may originate from interface roughness. This work supports the RKKY like interaction theory.

Zusammenfassung

In dieser Arbeit wurden die magnetischen Eigenschaften ultradünner Fe-Schichten zwischen 1.5 und 16 Monolagen und die Austauschkopplung von Fe-Schichten über verschiedene Zwischenschichten, mittels Brillouin Lichtstreuung und magnetooptischem Kerr-Effekt untersucht. Das epitaktische Wachstum und die Einkristallqualität der Proben wurden mittels RHEED-, SPALEED- und AES kontrolliert. Die Untersuchungen der Austauschkopplung dünner Fe-Filme über Cr-Zwischenschichten ergaben, daß zum erstenmal für Proben auf GaAs Substraten Oszillationen mit zwei Perioden in Abhängigkeit von der Cr- Dicke beobachtet wurden. Zuvor war die Oszillation mit der kürzeren Periode nur an Proben auf Fe- whiskern nachweisbar. Für die Fe/Cr- Schichtungen auf GaAs wurde auch die Temperaturabhängigkeit und Stabilität der Kopplung bis 700K untersucht. Die Periode der Oszillationen und die Abnahme der Kopplungsstärke mit der Cr- Dicke konnten mit Hilfe des „nesting"- Effektes in der Fermi- Fläche des Cr verstanden werden. Der Anteil biquadratischer Kopplung und das Ausbleiben eines erwarteten „phase slip" bei den Oszillationen, wie sie bei den Proben auf Fe- whiskern nachweisbar waren, ist auf Störungen im Kristallgitter und an der Fe/Cr- Grenzfläche zurückzufüren. Der Einfluß der Grenzflächenrauhigkeit auf die oszillierende Austauschkopplung wurde durch eine in die Cr- Schicht zusätzlich eingebettete Ag- Schicht untersucht. Diese bewirkte eine Verstärkung der biquadratischen Kopplung und Abschwächung der bilinearen Kopplung, was auf eine erhöhte Grenzflächenrauhigkeit zurückgefürt werden kann. Bei Zwischenschichten aus Edelmetallen oszillierte die Kopplung mit zwei Perioden, in guter Übereinstimmung mit einer RKKY- artigen Wechselwirkungstheorie. Im Fall der Edelmetalle ist damit geklärt, daß die Perioden durch extremale Entfernungen in der Fermi- Oberfläche des Zwischenschichtmaterials gegeben sind. Auch an diesen Schichtungen wurden Temperexperimente durchgeführt. Bei Proben mit Zwischenschichten aus Cu/Au- Legierungen mit einer 1:1 Zusammensetzung ergab sich eine große Verstärkung der Kopplung durch Tempern. Dies wurde auf die Ausbilding von geordneten Phasen wie man sie hier erwartet und damit reduzierten Elektronenstreuung zurückgeführt. Bei disen Proben konnte sogar ein Umschlagen der Kopplung von ferro- nach antiferromagnetisch durch Tempern nachgewiesen werden.

Acknowledegments

At first I would like to express my heartfelt thanks to Prof.Dr. W.Zinn for granting me the opportunity to pursue my Ph.D degree in the Faculty of Mathematics and Nature Sciences, University of Cologne, and to conduct this work in the Division of Magnetism and Low Temperature Physics, Department of Solid State Research, Research Center Jülich, Germany. His extensive knowledge in physics and many simulating discussions with him would be much beneficial to this work.

I am deeply grateful to Prof.Dr. P.A. Grünberg. He has introduced me to the exciting world of interlayer magnetic coupling and giant magnetoresistance effect. The results of this work rely on his guidance, active assistance and many fruitful discussions with him. Working with him in the past three years has been an enriching experience. I also thank him for a careful and critical reading of this manuscript.

I am especially grateful to Mr. R.Schreiber for his valuable assistance in the sample preparation and characterization, and many other technical supports.

Many thanks to my co-students and co-workers, Dr. A.Fuß, Dr. J.A.Wolf, Dr. M.Vohl, Dr. S.Demokritov, Dr. R. Schäfer, Mr. R. Mosler, Mr. V.Cros, M.Schäfer for their assistance in experiments, many helpful disscusions and otherwise.

I am very grateful to Prof. P.X.Zhang, Dr. Ch.Sauer, Dr. E.Tsymbal, Dr. U.Köbler, for good cooperation and many valuable discussions.

I am also grateful to Prof. J.Slonczewski, Prof. P.M.Levy, Dr. Barnas, Dr. P.Bruno, Dr. Z.J.Lin, Dr. F.R.Wang and Mr. M.Schneider for many hints and simulating discussions during composing this work.

I would like to thank Mr. C.Osthöver for the SQUID measurement, Mrs. S.Handschuh for the CEMS measurement, Dr. Q.Chen for the measurement of AC susceptibility and Mr. J.C.Chen for the SEM image.

Special thanks to Mrs. H.Sittardt for her kind help in administrative affairs.

I should also like to thank my wife, Xiaoli Li, for typing the corrected manuscript and good family atmosphere during the stay in Jülich, Germany.

Without extensive help from a number of colleagues and friends, some of whom are not named here, this work would not have been possible. I express my sincere gratitude to them.

FORSCHUNGSZENTRUM JÜLICH GmbH

Jül-2934
Juli 1994
ISSN 0944-2952